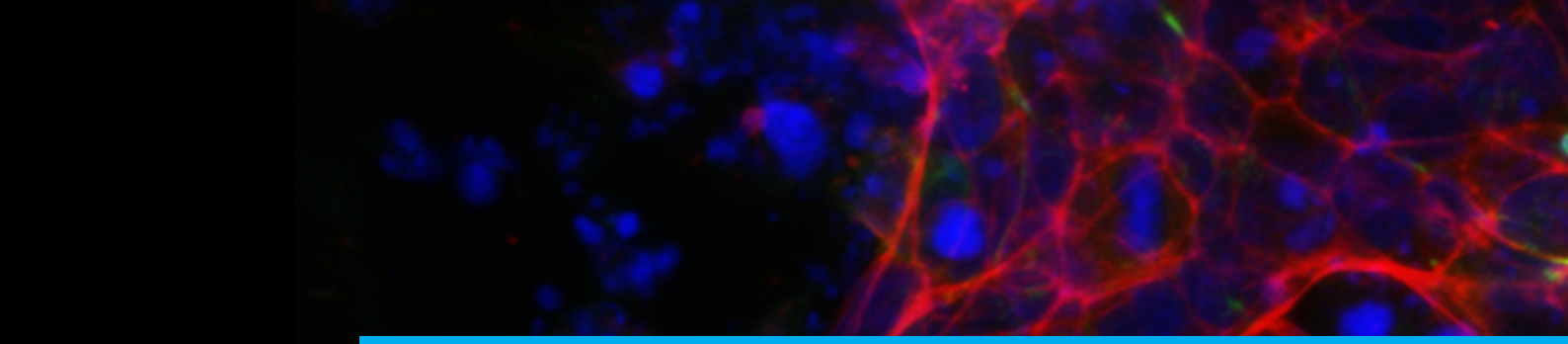

Department of Precision and Microsystems Engineering

Two-photon polymerized scaffolds for neuronal differentiation of mouse embryonic stem cells

D.W. Veldkamp

Report no : 2022.018
Coaches : Ir. A. Sharaf, Dr. C.P. Frias
Professors : Dr. A. Accardo, Dr. D.H. Meijer
Specialisation : Micro and Nano Engineering
Type of report : MSc Thesis
Date : 31 May 2022

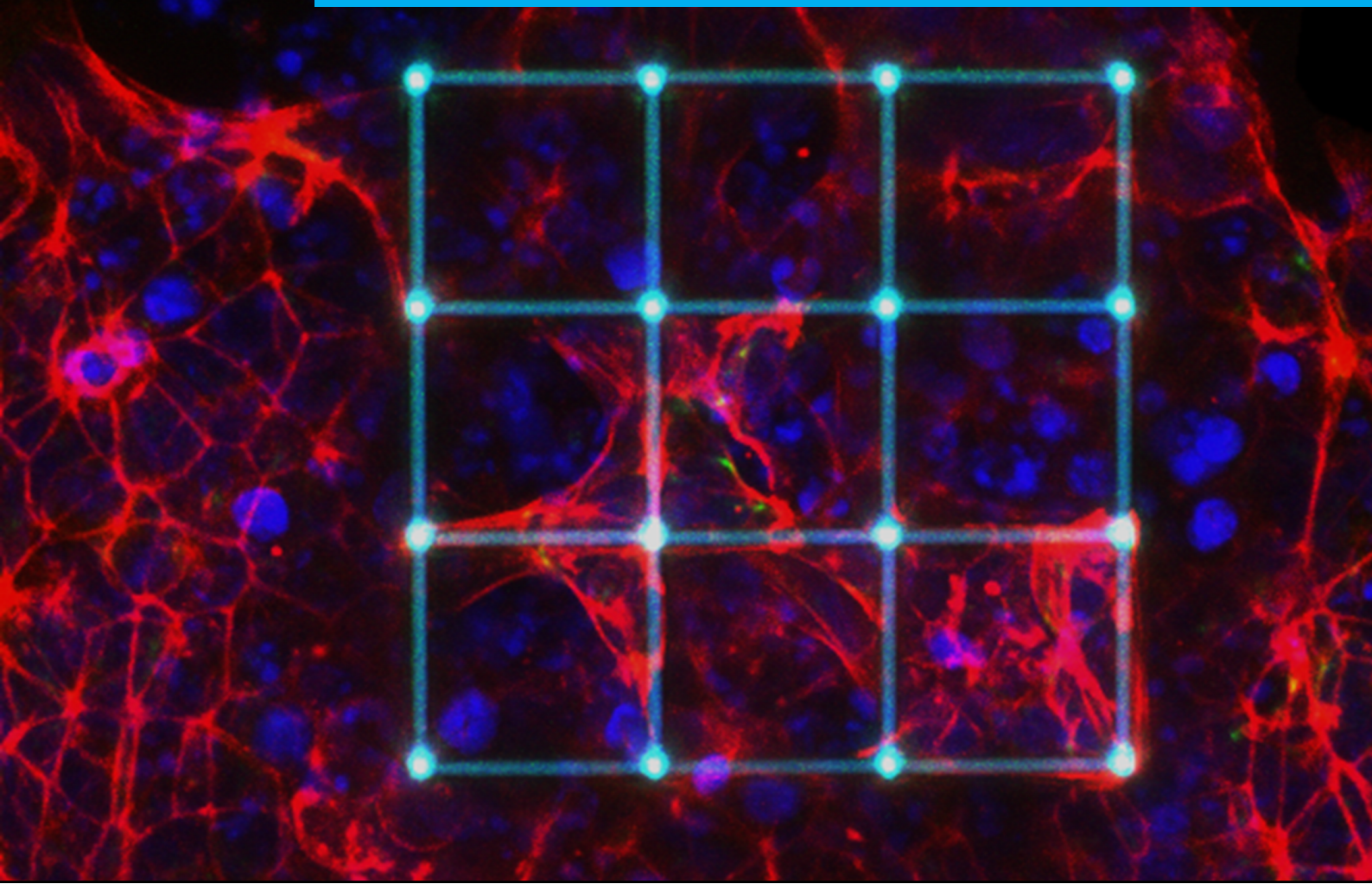

TU Delft Delft University of Technology

Challenge the future

Two-photon polymerized scaffolds for neuronal differentiation of mouse embryonic stem cells

by D.W. Veldkamp
Student number: 4226879

Supervisors:
Dr. A. Accardo
Dr. D.H. Meijer

Daily supervisors:
Ir. A. Sharaf
Dr. C.P. Frias

In collaboration with The Department of Bionanoscience
(Faculty of Applied Sciences)

Faculty: Mechanical Engineering
Department: Precision and Microsystems Engineering
TU Delft

June 1, 2022

Acknowledgements

Before you lies the thesis that concludes my years as a student in Delft and is the result of many long hours in several labs during which I learnt to appreciate the radio again. The project was a collaboration between the department of Precision and Microsystems Engineering and the department of Bionanoscience. Furthermore, I made several trips to the Erasmus Optical Imaging Centre in Rotterdam to use their confocal microscope. It might not have been the most convenient to carry out such an interdisciplinary project during a global pandemic, but I certainly learnt a lot from it. I would like to take the opportunity to thank the people who supported me during this project.

First, I would like to thank Angelo for spiking my interest in this subject, which may or may not be due to the nice image from the Small paper. I appreciated your valuable feedback, encouragement and patience during this period. I also wish to thank my daily supervisor at 3mE, Ahmed, for his continuous support, nice talks and wise words. I am grateful to Dimphna and Cátia for welcoming me to their department with open arms and providing me with valuable insights from a biologists' perspective. Special thanks to Cátia for making sure I had some good-looking cells to image and teaching me how to fix cells and make panels.

Many thanks go out to Beatriz who helped me ease into the topic at the beginning of this project and whose work provided a perfect starting point for my research. I also had the pleasure of working with Gert-Jan at the Erasmus optical centre, who provided me with confocal imaging training and was not afraid to think out of the box and try innovative imaging methods. Additionally, I want to thank the lab technicians and other people who provided me with the necessary instrument training and were always ready to assist in need of help.

Lastly, I like to thank my family, friends and boyfriend for believing in me and trusting that I would someday finish writing this thesis. I especially want to thank my dad for pushing me when I needed it and helping me with the statistical analysis.

Abstract

The central nervous system has a very limited capacity to regenerate damaged tissue. Therefore, regeneration strategies focus on transplantation of neural stem cells or differentiated neural cells. In order to make such a treatment effective, it is important to understand the mechanisms that enable cell differentiation. It is well known that besides biochemical cues, also mechanical and geometric properties of the cell environment, such as topography, curvature and stiffness, can influence the process, which has been studied mostly in 2D. In order to conduct relevant cell studies *in vitro*, it is therefore important to mimic the 3D structure of the *in-vivo* cell environment. Many different approaches have been adopted to create scaffolds for neuronal cells, such as freeze-drying, electrospinning and stereolitography. The main drawbacks of these methods are the limited resolution and the constraints in terms of achievable geometries. Two-photon polymerization overcomes these problems by using a laser to polymerize a photosensitive material in extremely confined volumes, achieving a submicrometric resolution. In this study, we fabricated 3D microscaffolds made of an acrylate polymer called IP-Dip by employing two-photon polymerization in order to study the effect of curved versus straight lattice geometries on the differentiation of mouse embryonic stem cells into neural progenitor cells. First, feasibility studies were carried out with HeLa cancer cells and the effect of curvature on these cells was investigated on 2.5D structures. We established a workflow for conducting these experiments from the fabrication up until the analysis. By employing confocal imaging, image stacks were obtained and then analysed to obtain the volumetric cell occupancy of the scaffolds and identify the location of the cells within the scaffolds. We concluded that mESCs could successfully grow and differentiate within the 3D scaffolds without a specific preference for a curved over a straight lattice structure.

List of acronyms

2PP	Two photon polymerization
AFM	Atomic force microscopy
AR	Aspect ratio
FA	Focal adhesion
GA	Glutaraldehyde
CFN	Chick forebrain neuron
CNS	Central nervous system
DiLL	Dip-in laser litography
DIW	Deionized water
DLP	Digital light processing
DLW	Direct laser writing
ECM	Extracellular matrix
ESC	Embryonic stem cell
GelMA	Gelatin methyacrylate
HEK	Human embryonic kidney
HMDS	Hexamethyldisilazane
hPSC	Human pluripotent stem cell
IPA	Isopropyl alcohol
mESC	Mouse embryonic stem cell
MSC	Mesenchymal stem cell
NA	Numerical aperture
NPC	Neural progenitor cell
NSC	Neural stem cell
PBS	Phosphate-buffered saline
PC12	Pheochromocytoma 12
PCL	Polycaprolactone
PDMS	Polydimethylsiloxane
PEGDA	Polyethylene glycol diacrylate
PFA	Paraformaldehyde
PGMEA	Propylene glycol methyl ether acetate
PLA	Polylactic acid
PLGA	Poly lactic-co-glycolic acid
PMA	Polymethyl acrylate
PNS	Peripheral nervous system
RI	Refractive index
ROI	Region of interest
SEM	Scanning electron microscopy
SLA	Stereolithography apparatus
TCPS	Tissue culture polystyrene
VSMC	Vascular smooth muscle cell
WD	Working distance

Contents

1 Introduction **1**
1.1 Biological background . . . 1
1.1.1 The central nervous system . . . 1
1.1.2 Interaction between cell and extracellular matrix . . . 2
1.1.3 Stem cells and the neural lineage . . . 3
1.2 Mechanobiology . . . 4
1.2.1 Influence of ECM stiffness on cells . . . 5
1.2.1.1 Cell differentiation and proliferation . . . 5
1.2.1.2 Cell morphology . . . 6
1.2.1.3 Cell migration . . . 7
1.2.2 Topography . . . 7
1.2.3 Influence of geometry and dimension . . . 7
1.2.3.1 Cell proliferation and differentiation . . . 7
1.2.3.2 Cell morphology . . . 8
1.2.4 Influence of substrate curvature (curvotaxis) . . . 8
1.3 Fabrication of 3D microstructures for neural cells . . . 9
1.3.1 Conventional methods . . . 10
1.3.2 Electrospinning . . . 10
1.3.3 Bioprinting . . . 10
1.3.4 Light assisted additive manufacturing methods . . . 10
1.3.5 Hybrid methods . . . 11
1.4 Two photon polymerization . . . 12
1.4.1 2PP for stem cell applications . . . 13
1.4.2 2PP for neural lineage applications . . . 13
1.5 Research objectives . . . 14

2 Materials and Methods **17**
2.1 Fabrication of 3D microstructures via 2PP . . . 17
2.1.1 Pedestals . . . 18
2.1.2 2.5D structures . . . 18
2.1.3 3D scaffolds . . . 19
2.2 Cell culture . . . 21
2.3 Immunofluorescence imaging . . . 22
2.3.1 Immunofluorescence staining . . . 22
2.3.2 Confocal imaging configurations . . . 23
2.4 Scanning electron microscopy . . . 24
2.4.1 Sample preparation for SEM . . . 24
2.4.2 SEM dehydration experiment . . . 25
2.5 Analytical approaches . . . 25
2.5.1 Characterization of scaffold deformation . . . 26
2.5.2 Comparison of confocal imaging configurations . . . 27
2.5.3 Characterization of cells on the 2.5D structures . . . 28

2.5.4 3D reconstruction of images . . . 28
2.5.5 Characterization of cells in the 3D scaffolds (HeLa, ESCs) . . . 28
2.5.5.1 Z-projection phalloidin and DAPI occupancy . . . 28
2.5.5.2 Volumetric phalloidin occupancy . . . 29
2.5.6 Characterization of ESC colonies . . . 30

3 Results and Discussion 32
3.1 Development of the 2PP scaffold workflow for cell culture . . . 32
3.1.1 Fabrication . . . 32
3.1.2 Press to seal . . . 34
3.1.3 Confocal imaging configurations . . . 35
3.1.4 SEM dehydration . . . 41
3.2 Effect of 2PP scaffolds on viability and morphology of HeLa cells . . . 45
3.2.1 Cytocompatibility and seeding density . . . 45
3.2.2 Curvature 2.5D . . . 46
3.2.2.1 Effect of pedestal thickness . . . 46
3.2.2.2 Effect of sinusoidal structures . . . 49
3.2.2.3 Effect of pyramidal structures . . . 52
3.2.2.4 Effect of triangular structures . . . 52
3.2.3 Culture of HeLa cells on 3D scaffolds . . . 55
3.2.3.1 Cell morphology . . . 57
3.2.3.2 Nucleus size . . . 58
3.2.3.3 Nucleus localization within 3D scaffolds . . . 58
3.2.3.4 Phalloidin and DAPI z-projection occupancy . . . 62
3.2.3.5 Volumetric phalloidin occupancy . . . 62
3.2.3.6 Correlation with surrounding cell density . . . 64
3.3 Preliminary results on the neural differentiation of embryonic stem cells growing on 2PP scaffolds . . . 67
3.3.1 ESC density and viability . . . 67
3.3.2 ESC morphology and location . . . 67
3.3.3 Occupancy of scaffolds in z-projection . . . 70
3.3.4 Formation of ESC colonies . . . 70
3.3.5 ESC differentiation . . . 71

4 Conclusion and Recommendations 74
4.1 Conclusion . . . 74
4.2 Recommendations . . . 75

5 Self-reflection 77

A Design table 78

B Print settings table 87

C Extra 3D scaffold designs 89

D Comparison threshold algorithms 90

E Dose tests 94

F Mean intensity comparison confocal imaging configurations 97
F.1 MP versus confocal in oil immersion configuration . . . 97
F.2 Confocal in vectashield immersion configuration . . . 98
F.3 Confocal with press-to-seal versus plastic sheet in water dipping configuration . . . 98
F.4 Confocal imaging with Vectashield and seal per scaffold type . . . 98

G Correlation SEM distortion top versus side of scaffolds **100**

H SEM dehydration experiment density **101**

I HEK-293T experiments **103**

J Effect of seeding location on cell distribution within press-to-seal **106**

K Simulation of projected major axis angle distribution in nuclei on sinusoidal scaffold **107**

L Distribution phalloidin within 3D scaffolds **108**

M Volumetric vs z-projection occupancy **109**

Chapter 1

Introduction

The central nervous system differs from the peripheral nervous system in that it has a very limited ability to regenerate cells after an injury or disease. This results in very different tactics needed to heal damaged tissue. In the case of small peripheral injuries, the ends of damaged nerves can be sutured together to repair the defect, as peripheral nerves have the ability to spontaneously regenerate [1]. In the case of larger damage to the PNS, transplantation using an nerve autograft (tissue from elsewhere in the body) or allograft (donor tissue) is the common practice [2]. The approach to peripheral nerve injuries is thus to facilitate nerve regeneration, provide guidance for axonal growth and to prevent fibrous tissue formation that hinders the regenerating nerve [1]. This approach is reflected in the research field as well, where the focus is on the guidance of neurons by producing for example tubes, ridges or aligned fibers from polymers.

Currently the most promising strategies to cure an injured brain are the transplantation of neural stem cells or differentiated neural cells. But in order for such a transplant to be successful, it is important to understand how cells will behave in the body. It is well known that cells react to chemical, mechanical and electrical stimuli from their surroundings, influencing cell migration, proliferation, differentiation, morphology and death. In order to understand these mechanisms, cell cultures need to be performed *in vitro*. The relevance of mimicking the 3D microenvironment of cells *in vivo* has become apparent as studies have shown a discrepancy between cell behaviour in 2D versus in the body.

Different fabrication methods have been employed to develop structures to support 3D growth of cells, such as freeze-drying, gas foaming, electrospinning and stereolithography. Drawbacks of these methods are limited resolution and decrease in design freedom. Two-photon polymerization overcomes these problems by using a laser to polymerize a photosensitive material in extremely confined regions, achieving a resolution of 100 nm.

1.1 Biological background

In order to investigate the use of neural stem cells in regenerative medicine, it is important to have an understanding of the nervous system, brain cell types and the process of stem cell differentiation. This chapter will give an introduction into these topics and shortly discuss stem cell culturing.

1.1.1 The central nervous system

The nervous system of vertebrates consists of the central (CNS) and the peripheral (PNS) nervous system. The CNS includes the brain and the spinal cord and forms the main control centre of the body. The PNS contains the nerves leading from the CNS to the rest of the body, providing communication paths. In this report we will focus on the CNS, which is largely composed of neurons and glial cells.

Neurons are excitable cells that collect, process and transmit electrical signals through specialized connections called synapses or axon terminals (see figure 1.1a). The cell function is reflected in their

morphology. The main body of a neuron is called the soma and contains the cell nucleus, from this soma one long axon emerges that conveys an output signal and multiple dendrites that collect electrical signals from the synapses of another neuron. There are over 200 different varieties of neurons [3] with different geometries, depending on their function in the neural system. In mammals, the typical size of a soma is in the order of 10 µm and the axon and dendrites have a diameter of less than 1 µm [3].

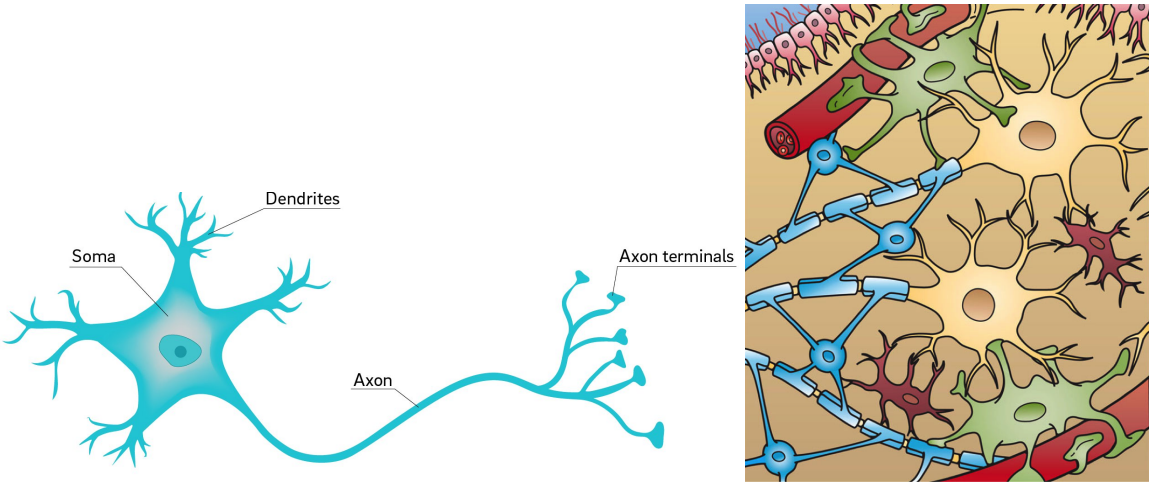

Figure 1.1: Brain cell types. (a) Schematic of a neuron. [4] (b) Schematic of brain tissue showing the interactions between neurons and glial cells. Oligodendrocytes (blue) form the myelin sheeth around the axons of the neurons (yellow). Astrocytes (green) contribute to the blood-brain barrier while microglia (dark red) play an immunological role. [5]

Glial cells can be divided into three main types: astrocytes, oligodendrocytes and microglia. Each of these glial cells performs different important tasks in the brain. Astrocytes, named after their star-like shape, have various functions: they supply nutrients to the neurons, help regulate the composition of the interstitial fluid in the nervous system and modulate synaptic activity [3]. Lastly, they contribute to the blood-brain barrier which is a semipermeable membrane that separates the blood circulation from the extracellular fluid in the brain, preventing certain particles like bacteria from reaching neurons.

Glial cells, unlike mature neurons, may retain the potential to divide and this is one of the reasons that brain cell cancers often originate from glial cells [3]. They are also associated with mechanical changes observed in injured brain.

Oligodendrocytes provide insulation to the axons, by forming the so called myelin sheath (analogous to Schwann cells in the PNS). Microglia play an immunological role by clearing cellular debris and dead neurons from nervous tissue through the process of phagocytosis (cell eating). Figure 1.1b shows the interplay between the different cells in the central nervous system.

1.1.2 Interaction between cell and extracellular matrix

All animal cells are enclosed by a cell membrane that separates the internal contents of a cell from the outside environment, called the extracellular matrix (ECM). Inside the cell, the nucleus is immersed in cytoplasm which consists of the aqueous medium cytosol, various organelles and several types of protein filaments. These filaments are organized in a dynamic network, forming the cytoskeleton of the cell (see figure 1.2).

The cytoskeleton not only gives the cell its shape and mechanical support, but also plays an important role in the dynamical properties of the cell such as migration, force generation and transduction of external signals. The cytoskeleton interacts strongly with the ECM through the formation of focal adhesions (FA) which attach the cell membrane to the ECM (see figure 1.2) and make transmembrane communication possible. FAs play a central role in cell migration, morphology,

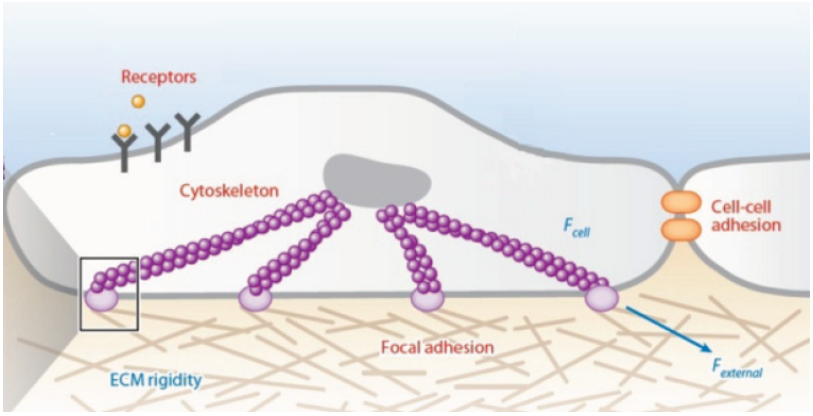

Figure 1.2: Schematic of cell and cytoskeleton (purple) interacting with the ECM through focal adhesions. Image adapted from [6].

proliferation, differentiation and death.

The composition of the ECM varies throughout the body and in different stages of development. In embryonic brains, the main proteins found in the ECM are laminin, fibronectin, collagen and heparan sulfate proteoglycan [3]. In adult brains, however, the main components are lecticans, a family of proteoglycans. These materials are often used in stem cell research for the neural lineage as substrate material or adhesive coating. Other adhesive coatings that can be encountered are non-specific adhesive molecules such as poly-L-lysine (PLL) or gelatin.

1.1.3 Stem cells and the neural lineage

Stem cells are characterized by the ability to self-renew, producing additional stem cells, as well as differentiate into multiple different cells by performing cell divisions. The number of cell types towards which a stem cell can differentiate determines its potency. For example, a stem cell that is totipotent can produce all differentiated cells in an organism, even extraembryonic cells (e.g. placenta cells), whereas a multipotent stem cell can only differentiate into multiple specialised cell types present in a specific tissue or organ.
Embryonic stem cells (ESC) are pluripotent cells, as they can give rise to all of the different cell types of the body but cannot produce extraembryonic cells. ESC differentiation is the start of all organs and tissues that make up an organism, such as the heart, the nervous system and the immune system (see figure 1.3).

Stem cells differentiate into several cell types through multiple steps, where each step creates more specialized cells. For neural differentiation, the first step is from the ESC to the neural stem cell (NSC). NSCs are multipotent cells which are able to self-renew and proliferate without limit, to produce neural progenitor cells (NPC). NPCs differ from NSCs in that they have a limited ability to proliferate, however, they can still differentiate into multiple cell types [8]. Differentiation of NPCs gives rise to neurons, astrocytes and oligodendrocytes (see figure 1.4). Microglia come from a different cell lineage. In this report, we will only be concerned with the neural lineage.

In further chapters a distinction is made between the early differentiation state, from ESCs to NPCs, and the late differentiation state from NPCs to neurons and glial cells.

The exact mechanisms of stem cell differentiation are still largely unknown. However, it is clear that biochemical, electrical and mechanical cues all play a role.

Protocols have been developed and established for the differentiation of stem cells into different cell lineages *in vitro*. These protocols are based on a mix of biochemical compounds that promote differentiation and are usually carried out in a 2D tissue culture polystyrene (TCPS) plate.

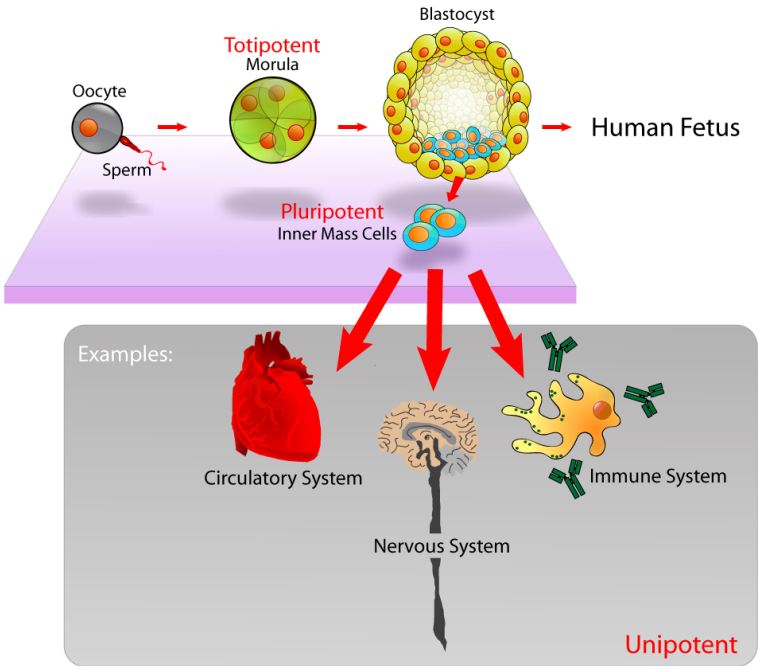

Figure 1.3: Schematic of stem cell differentiation process. Embryonic stem cells (here depicted as blue with orange nucleus) are present in the inner cell mass of an early embryo (blastocyst) and can differentiate into multiple different cell types that form organs and tissues. [7]

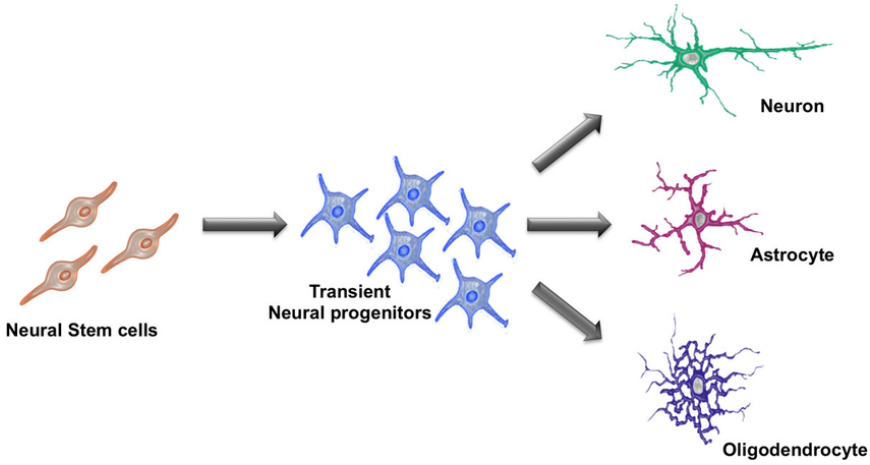

Figure 1.4: Differentiation from NSCs to neurons, astrocytes and oligodendrocytes. [9]

1.2 Mechanobiology

Cells are known to interact with their surroundings, reacting to biochemical, electrical and mechanical stimuli such as forces, elasticity and topography. The field of mechanobiology studies how mechanical properties can influence cell processes like migration, differentiation, proliferation and cell death. Important terms in mechanobiology are mechanosensing and mechanotransduction. Mechanosensing is the process by which living cells sense mechanical forces and or deformations applied externally. Mechanotransduction is the conversion of this mechanical signal into a biochemical signal. While the exact molecular mechanisms of these phenomena are still unknown [10], it is clear that the interaction between the cytoskeleton and the ECM plays an important role.

In this chapter, several aspects of mechanobiology will be highlighted, while mainly focussing on

neural cells and the differentiation of stem cells into the neural lineage. The influence of ECM stiffness, topography and geometry on cell migration, morphology and proliferation and differentiation will be explored.

1.2.1 Influence of ECM stiffness on cells

It has been widely recognized that among other cues, ECM stiffness can play a significant role in the function of cells such as growth, spreading and differentiation. However, the mechanotactic behaviour of cells is cell type dependent and context dependent. Some cells are highly mechanosensitive, whereas others seem to have no preference for stiffness within a certain range. This section will highlight how ECM stiffness can influence stem cell differentiation and neural cells.

In the following sections, whenever the word stiffness is used, this will refer to the elastic modulus or Young's modulus of a material. In order to make the mentioned stiffness values more relevant, one can compare them with the ones of various tissues (see figure 1.5). The Young's modulus of tissues varies largely between organs and tissues, and is inherently related to tissue function [11]. Tissues exposed to high mechanical loading, such as bone or skeletal muscle, exhibit moduli which are much larger than static tissues such as the brain. For example, the stiffness of brain tissue is around 500 Pa compared to 10^4 Pa for muscles and $10^9 - 10^{10}$ Pa for bone tissue [12].

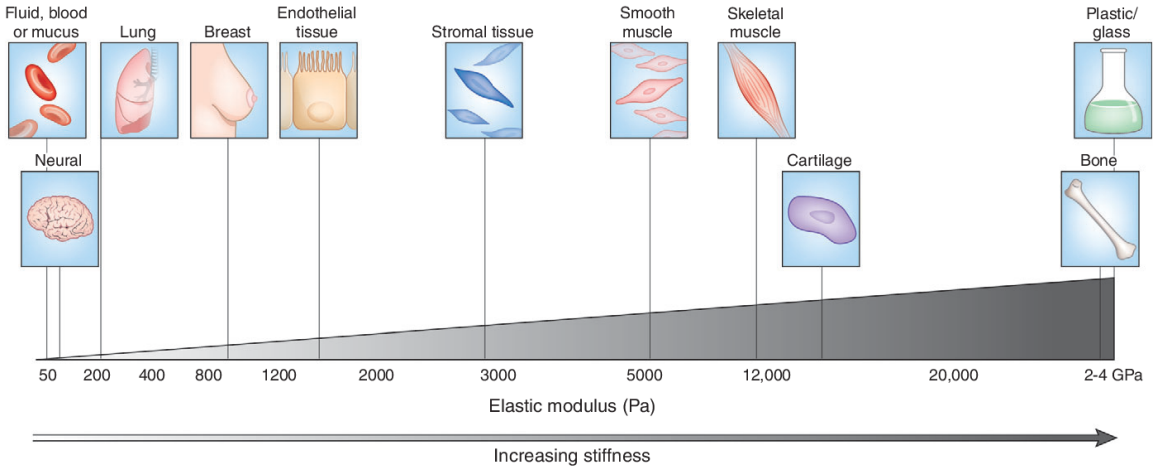

Figure 1.5: Variations in tissue stiffness. The biomechanical properties of a tissue in terms of stiffness (elastic modulus), measured in pascals (Pa). Retrieved from [11].

.

1.2.1.1 Cell differentiation and proliferation

It is established that stem cell differentiation is influenced by the stiffness of the ECM, or in the *in vitro* case, the microenvironment. It was shown that soft matrices that mimic brain tissue (0.1–1 kPa) are neurogenic (i.e. induce the formation of neural cells), stiffer matrices that mimic muscle tissue (8-17 kPa) are myogenic (i.e. induce the formation of muscle cells), and comparatively rigid matrices that mimic collagenous bone (25-40 kPa) prove osteogenic (i.e. induce the formation of bone cells) [13]. Ali et al. cultured mESCs on substrates of varying stiffness: 2 kPa, 18 kPa and 35 kPa. They found that cell expansion was independent of stiffness, implying that the proliferation of cells during the differentiation process was independent of the Young's modulus [14]. Furthermore, cell attachment decreased with increasing substrate stiffness which is possibly due to soft substrates preferentially absorbing the integrin protein vitronectin that strongly promotes mESC attachment [14].

Experiments concerning the influence of the substrate modulus on late neural differentiation have been performed in both 2D and 3D with varying materials and cells. Saha et al. studied the influence of substrate stiffness on the behaviour of neural stem cells and found that NSCs optimally differentiated into neurons on substrates of intermediate stiffness (500 Pa) [12]. Furthermore, they showed that softer gels (100–500 Pa) greatly favored neurons, whereas harder gels (1,000–10,000 Pa) promoted glial cultures. However, on very soft substrate (10 Pa) cell spreading, self-renewal and differentiation were inhibited.

Banerjee et al. performed a same kind of experiment in 3D, where they encapsulated neural stem cells in alginate hydrogels of differing stiffnesses (range 180-19700 Pa) [15]. They concluded that the rate of proliferation of NSCs decreased with an increase in hydrogel modulus, obtaining the highest number of cells at 183 Pa. They also found the highest relative expression for the neural marker in the softest hydrogel, showing a $\sim$20 fold increase in β-tubulin III expression compared to the stiffest hydrogel.

In general, most studies seem to agree that a higher stiffness substrate is beneficial for growing astrocytes whereas a soft substrate promotes the growth of neurons [12] [15] [16] [17] [18] [19] [20].

However, there have also been some contradictory results, where they found that a higher Young's modulus (1000 Pa vs 1 Pa) offered a better condition for neural differentiation while yielding less astrocytes [21]. Other studies found that differentiation into astrocytes was promoted on a softer substrate as well [22] [23]. Lastly, Leipzig et al. showed that a soft substrate was preferential for growing both neurons and astrocytes [24].

Possible explanations for the contradictory results could be the range of stiffness measured, the use of different cell media or the method of measuring substrate stiffness. In the case of hydrogels, stiffness measurements can differ greatly depending on the employed measuring method since they are very soft materials. Furthermore, the measuring conditions (e.g. wet or dried hydrogel) change the stiffness value as well, but these conditions are often not explicitly mentioned. Lastly, there is an inter-dependency between stiffness and permeability of hydrogels [25] that, if not taken into account, can also influence test results.

1.2.1.2 Cell morphology

Several studies have been conducted to find a relation between substrate stiffness and neurite extensions. Most studies agree that the number of neurites, neurite branching and rate and length of outgrowth are all increased on softer materials compared to stiffer materials ([16] [20] [22] [26] [27] [28]).

However, Leach et al. found a different response using PC12 cells and a stiffness range of 7 Pa–19 kPa [29]. The team found that below a certain substrate stiffness threshold, neurite outgrowth and branching sharply decreased. On a soft hydrogel substrate of 7 Pa only a few short neurites were formed, whereas on the hydrogels with a shear modulus of 190 Pa and above, significantly more neurites were initiated, which were longer and more branched. They give some possible explanations for this discrepancy, hypothesizing that neural response to substrate compliance is a strong function of neuron type and range of compliance investigated. They also stressed the importance of quantifying ligand (adhesion molecule) density, analyzing large sample sets and applying appropriate statistical tests.

1.2.1.3 Cell migration

The migration of cells due to stiffness gradients is called durotaxis. This term dates back to Lo et al., who were the first to report that fibroblasts tend to move from softer to stiffer regions of a coated substrate [30]. Vincent et al. observed the same phenomenon with MSCs: the cells migrated towards the stiffest region on the gradient. They also found that migration velocity correlated directly with gradient strength [31].

1.2.2 Topography

Different surface features such as pillars, grooves, and ridges are able to promote and direct the axonal elongation in vitro [32]. Marino et al. designed substrates with parallel submicrometric ridges for the promotion of axonal outgrowth and guidance [32]. They compared three different spacings between the ridges, namely 2.5, 5 and 10 µm. They demonstrated that both PC12 cells and human neuroblast derived cells form strongly aligned neurites with respect to more spaced ridges and the flat control substrates (see Figure 1.6b). Furthermore, they detected an increased differentiation of human neuroblast derived cells into neurons when grown on submicrometric patterned substrates with a 2.5 µm spacing. Lastly, it was observed that axons can exert strong enough forces to bend ridges (see Figure 1.6a). The force was estimated to be in the order of 3 nN.

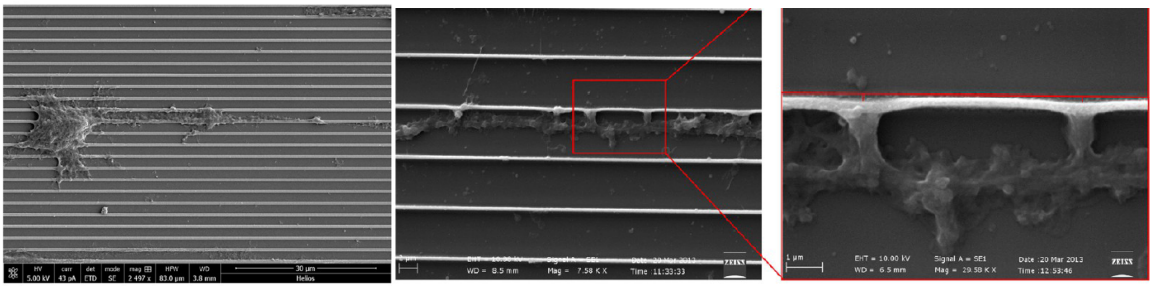

(a) (b)

Figure 1.6: Neural differentiation and alignment on substrate with submicrometric ridges. Images retrieved from [32]. (a) Neurite alignment of PC12 cells parallel to ridges. (b) PC12 cells deforming a ridge.

Several other studies that employed electrospinning to create fibrous 3D structures observed alignment of neuritic extensions along the fibers [33] [34] [35], which is in accordance with the results obtained by Marino et al. [32]. Abbasi et al. found that aligned nanofibrous scaffolds highly supported the proliferation and spreading of mESCs when compared to random nanofibrous scaffolds and TCPS [36].

1.2.3 Influence of geometry and dimension

It is known that cells in 2D react differently than cells cultured in 3D. Moreover, structure geometries, such as the fiber diameter in electrospun scaffolds, have been shown to change the morphology of the cells and influence cell processes such as migration, proliferation and differentiation. The exact mechanisms that are responsible for these changes are still not clear.

1.2.3.1 Cell proliferation and differentiation

In 2014, Wei et al. [37] studied the effects of 2D versus 3D structures on the stemness maintenance of mESCs. mESCs cultured on 3D scaffolds made of collagen, PLGA and chitosan were compared to 2D cultured cells. By employing cell counting, clone formation essays, pluripotency markers and gene expression profiling, they found that 3D scaffolds promote stemness maintenance and supported pluripotency in long term cell culture (one month) without feeder cells (cells that secrete growth factors to promote cell proliferation). Since feeder cells are believed to be the major source of xeonogeneic contaminants [37], this is a promising result. Furthermore, they found that the change in dimension had more impact on the genome expression than the type of material.

A study by Christophersen et al. reported that the fiber diameter of an electrospun scaffold significantly influences rat NSC (rNSC) differentiation and proliferation [38]. The laminin coated polyethersulfone (PES) fibers had average diameters of 283, 749 and 1452 µm and were compared to a TCPS control. Under differentiation conditions, rNSCs showed a 40% increase in oligodendrocyte differentiation on the 283 nm fibers and a 20% increase in neural differentiation on the 749 nm fibers compared to the 2D control. Overall, cell cultures grown on fiber scaffolds showed higher levels of

differentiation marker compared to TCPS. Cell proliferation, however, was lower on the fibers.

1.2.3.2 Cell morphology

In the aformentioned study of Wei et al. [37], they also studied the morphology of mESCs cultured under 2D and 3D conditions. While the cells in 2D became more spread and irregular, the cells cultured in 3D presented a more spherical and compact morphology.
This more rounded morphology was also observed by Christophersen et al. [38]. A decrease in fiber diameter of an electrospun scaffold resulted in lower proliferation rate, increased cell spreading and less clustering of cells. This result suggests that cell spreading and migration might be factors that enhance cell proliferation.

1.2.4 Influence of substrate curvature (curvotaxis)

In more recent studies it was found that cells can also respond to cell-scale curvature variations, a phenomenon which is called curvotaxis. Cells can discriminate between planar, convex and concave surfaces to different extents by reshaping or adapting. In some cases, cells were even found to avoid certain regions of curvature, for example in the study by Pieuchot et al. [39] where they cultured MSCs, fibroblasts, macrophages and epithelial for 24 hours on a sinusoidal surface (see figure 1.7A1). The strongest response was observed with MSCs (both murine and human) which positioned their nuclei in the most concave areas (figure 1.7A2) whereas macrophages were evenly distributed. The response of the MSCs increased with ligand density, time and surface aspect ratio. In a study by Werner et al. [40] it was found that hMSCs have different migration modes on convex versus concave surfaces, resulting in a significantly higher migration speed on concave versus flat and convex surfaces. The cells also assumed a different morphology. On concave surfaces, they were stretched upwards with a part of the cell body detached from the surface whereas cells on convex surfaces were fully attached (see figure 1.7B). Additionally, they found that convex spherical surfaces induced osteogenic differentiation of hMSCs, even in the absence of osteogenic growth factors. Furthermore, cylindrically curved structures such as fibers, tubes and rounded ridges are often found to induce cell-body elongation and alignment along the longitudinal axis of the structure. For fibroblasts they found that the orientation was inversely related to the fiber diameter [41] (see figure 1.7C1 and C2). However, not always does a cell align longitudinally, in some experiments cell organized circumferentially around fibers or oriented transversely to cylinder axis of fibers. Curved surfaces are also thought to facilitate the formation of tight junctions between epithelial cells [42].

While the exact mechanisms for curvotaxis are still to be uncovered, some underlying factors have been identified. Curvotaxis includes events such as bending of the cell/plasma membrane and induction of cell polarity [42]. Proteins that are associated specifically with mechanotransduction on convex surfaces are the so called BAR domain proteins which can recognize and induce bending of the cell membrane. Similarly, inverse BAR domain proteins (I-BAR) have been identified to play a role on concave surfaces. FA organization and dynamics was also changed by curvature which in combination with a change in polarity can have an effect on for example symmetric versus asymmetric division and other cell mechanisms.

Moreover, the nucleus plays a role in curvature sensing. For example, in MSCs on a curved surface, a lower ligand density resulted in a lower response to curvature and compact cells with spherical nuclei whereas a high ligand density created well spread and strongly compressed nuclei [39] indicating that nucleus shape influences curvotaxis. They also tried silencing Lamin A, the main contributor to nuclear stiffness, which significantly affected the cells' ability to respond to curvature. Furthermore, curvature was shown to alter gene expression of hMSCs. Werner et al. [40] observed that a convex surface induced nuclear compression and associated higher Lamin-A levels. Fibers of the perinuclear actin cap (a dome like cap of actin fibers located above the nucleus) even indented in the nuclear membrane which was not seen on the flat surface or the concave surface.

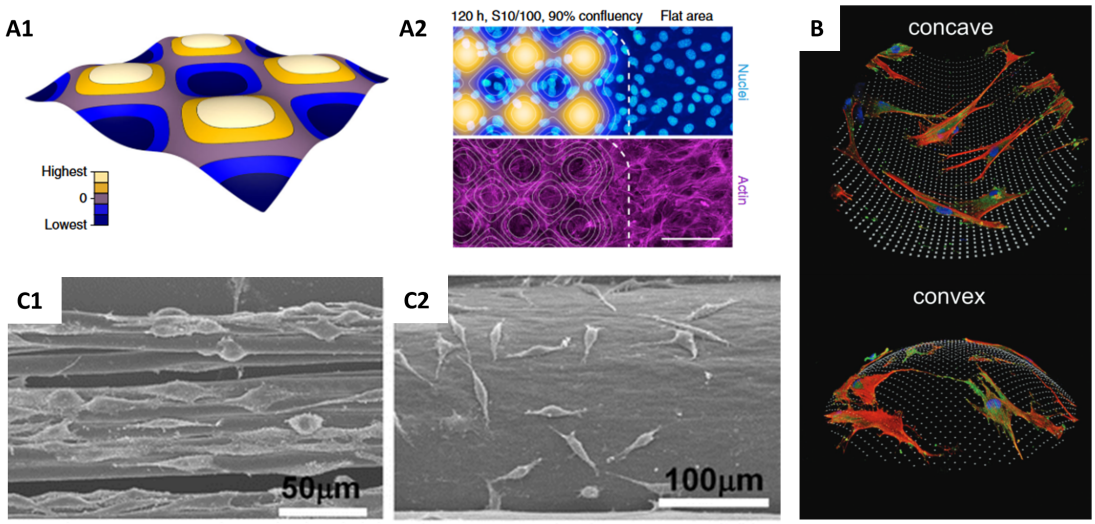

Figure 1.7: Examples of cell response to substrate curvature. A1) Schematic of hills-and-valleys landscape used in curvotaxis studies by Pieuchot et al. [39]. A2) MSCs position themselves on concave valleys (blue regions indicated in A1) on a S10/100 surface (A=5, λ=100). Cells stained for DNA and actin. Scalebar: 100 µm. B) 3D reconstruction of cells (F-actin in red, FAs in green, and nuclei in blue) on a concave and convex surface. Image adapted from [40]. C) Mouse L929 fibroblasts on PLGA fibers with a diameter of 10 µm (C1) and 242 µm (C2). Alignment of the cells with respect to the long axis of the fibers was inversely related to the fiber diameter. Images adapted from [41].

1.3 Fabrication of 3D microstructures for neural cells

There are a lot of different methods for creating 3D microstructures. What is mostly important for neural applications is that the material of the scaffold is relatively soft. Therefore, the most often used materials are polymers and hydrogels. Furthermore, porosity is very important in 3D cell cultures. We will discuss the most common fabrication methods for neural applications: conventional methods, electrospinning, bioprinting, light assisted additive manufacturing methods and hybrid approaches. This chapter will not go into detail of the working principles of all these methods. An exhaustive overview of these methods and clear schematics of their working principle are given in the paper of Papadimitriou et al. [1]. The process of two-photon polymerization will be explained and various examples of produced 3D scaffolds used for stem cells and or the neural lineage, will be given.

1.3.1 Conventional methods

Conventional methods are the older and more traditional methods for 3D fabrication, like gas foaming, solvent casting, freeze-drying and hydrogel formation. Scaffolds produced by these methods are characterized by their sponge like porous structure. The average pore size can often be influenced but location of the pores and thus interconnectivity is random and there will always be a variation in pore size present. In some of these methods, the outside of the material is not porous, thus not allowing cells to enter.

1.3.2 Electrospinning

Electrospinning has been used a fair amount of times with stem cells that were directed to the neural lineage. Electrospinning forms a scaffold by producing polymer fibers that can either be aligned or randomly placed. It has been used in studies on fiber orientation, fiber diameter, fiber stiffness and their influence on cell differentiation. Several studies that employed electrospinning were already mentioned in section 1.2.2. Figure 1.8 shows differentiated hESCs forming neuritic extensions on an electrospun scaffold. Neurites could be observed to exert forces on the fibers by a tugging motion.

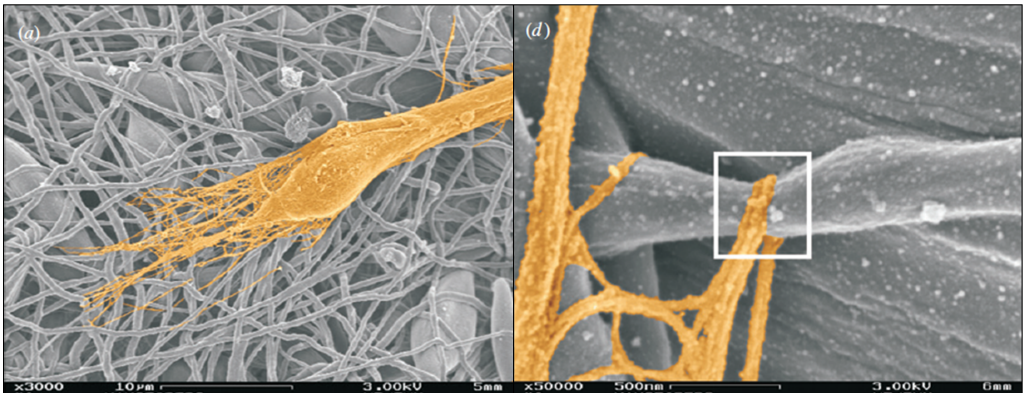

Figure 1.8: Electrospun polyurethane scaffolds for proliferation and neuronal differentiation of human embryonic stem cells. Scale bar is 10 µm. Image adapted from [35].

Sperling et al. studied the influence of fiber orientation on neural differentiation of mESCs and found that NPCs derived from the mESCs could survive and migrate onto the scaffolds [43]. Neuritic extensions preferentially extended along the axis of the fiber when fibers were aligned. Furthermore, nestin and β-III tubulin marker expression, respectively for NPCs and neurons, was enhanced on the aligned fibers in comparison with other groups.

1.3.3 Bioprinting

Bioprinting techniques are based on an ink or solution that contains a hydrogel, bioactive molecules and cells. This solution can be printed by methods like inkjet printing or extrusion bioprinting. Bozza et al. encapsulated mESCs [44] in alginate based beads. Cells were mixed with the alginate solution and dispensed from a syringe drop by drop into a gel-forming solution, that allows the alginate to polymerize. The cells were cultured for 18 days. It was demonstrated that differentiation increased within the beads compared to the 2D control and the generated neurons were able to form networks.

1.3.4 Light assisted additive manufacturing methods

Light assisted additive manufacturing methods make use of the photosensitivity of liquid polymers and employ a light source to polymerize a material. The most used method is stereolitography (SLA) which employs a UV light to polymerize a structure, layer by layer by using a laser beam. Digital light processing (DLP) follows the same layer-by-layer mechanism but each 2D layer of the 3D structure is exposed to UV light in one shot, making it a much faster process. Lastly, there is the process of 2PP, which can achieve much higher resolution due to its working principle which shall be explained in section 1.4. 2PP scaffolds created for stem cells and neural cells can be found in section 1.4.1 and 1.4.2.

A DLP scaffold for neural differentiation is shown in figure 1.9. Hexagonal and woodpile structures were printed from PEGDA and GelMA and were shown to support human neuronal cell growth and the formation of neuritic extensions [45]. Examples of structures printed by SLA for neural differentiation can be found in figure 1.10.

1.3.5 Hybrid methods

Tu et al. combined SLA and the freeze drying method to provide a strong backbone of PEGDA for porous gelatin [46]. First, a 3D lattice structure was created by SLA with pores in the order of 600 µm and a beam diameter in the order of 200 µm. Subsequently, the structure was immersed in a gelatin solution and freeze-dried (see Figure 1.10a). Finally, the structure was coated with laminin to promote cell adhesion. NPCs were obtained from the cortex of a mouse embryo and expanded

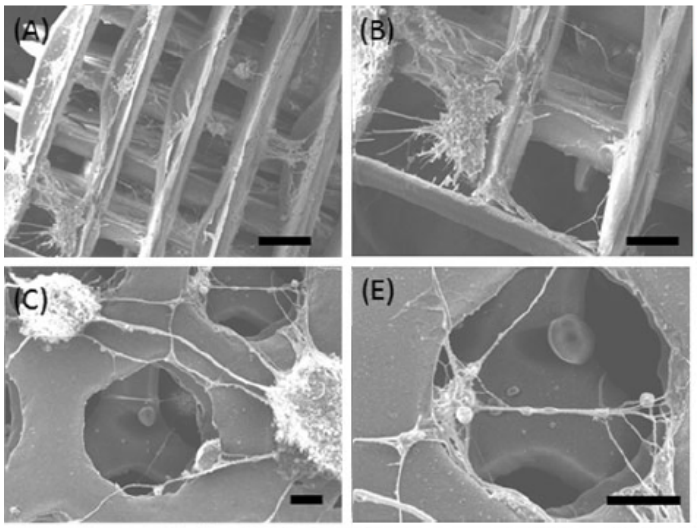

Figure 1.9: SEM image of PEGDA woodpile (A and B) and hexagonal scaffolds (C and E) created by DLP and seeded with human stem cell derived neural cells. Neuritic bridges were formed across the pores. Scale bar is 100 µm. Image adapted from [45].

in vitro before seeding on the scaffold. After a 7-day culture, fluorescent staining indicated the formation of neurons. Interestingly, the viability of the cells on the scaffold compared to a control on a traditional tissue culture plate, was significantly less.

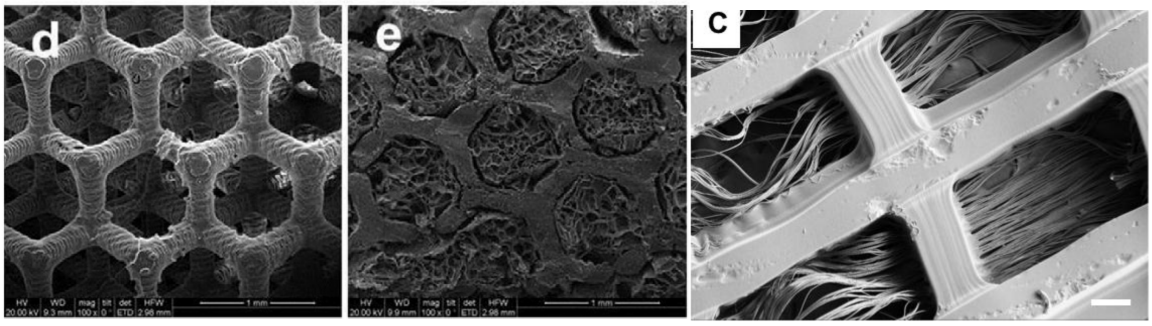

(a) (b)

Figure 1.10: Scaffold made by combining fabrication methods. Figure (a) is retrieved from [46] with on the left the PEGDA scaffold made by SLA and on the right the scaffold filled with freeze-dried gelatin, scale bar in both pictures is 1 mm. (b) SLA scaffold from PEGDA filled with electrospun PLA fibers [47], scale bar is 200 µm.

Lee et al. combined SLA with electrospinning to create a 3D structure of PCL and PCL/gelatin fibers embedded in a hydrogel scaffold [47]. First, the fibers were electrospun and then immersed in a solution of PEGDA and a photoinitiator. A porous scaffold structure was designed and printed by employing SLA which resulted in the scaffold in Figure 1.10b.

Scaffolds with PCL/gelatin fibers were compared with scaffolds with PCL fibers and a control without fibers. All structures were coated with laminin to promote cell adhesion. The scaffolds were tested with mouse embryonic derived NSCs as well as rat cortical neurons. The results showed improved NSC adhesion and proliferation on scaffolds with aligned fibers compared to the control scaffold. Moreover, they showed that the scaffold with PLA/gelatin fibers greatly increased the average neurite length and directed the neurite extension of the cortical neurons along the fiber.

1.4 Two photon polymerization

Two photon polymerized microstructures have been used to study a wide range of phenomena in the field of mechanobiology, for example cell migration, networking and determining the forces that cells can exert on structures. Every application requires a different structure.

The principle of two-photon polymerization is based on the phenomenon whereby a molecule is excited to a higher energy state by simultaneously absorbing two photons. Each of the photons carries half of the total energy needed to stimulate photopolymerization of the material via the use of a photo-initiator. In order for polymerization to occur, these photons must arrive within 1 femtosecond after each other, an event that is unlikely to occur anywhere except in the focal point of the laser [48]. Since photosensitive materials are usually transparent in the infrared and highly absorptive in the UV range, one can initiate two-photon polymerization with IR laser pulses within a small volume (voxel) of the material (see figure 1.11). This is not possible in the case of one-photon polymerization or stereolithography, where photon absorption takes place along the focalization cone. This is the reason why stereo lithography is a layer by layer process, but 2PP is a direct laser writing method (DLW).

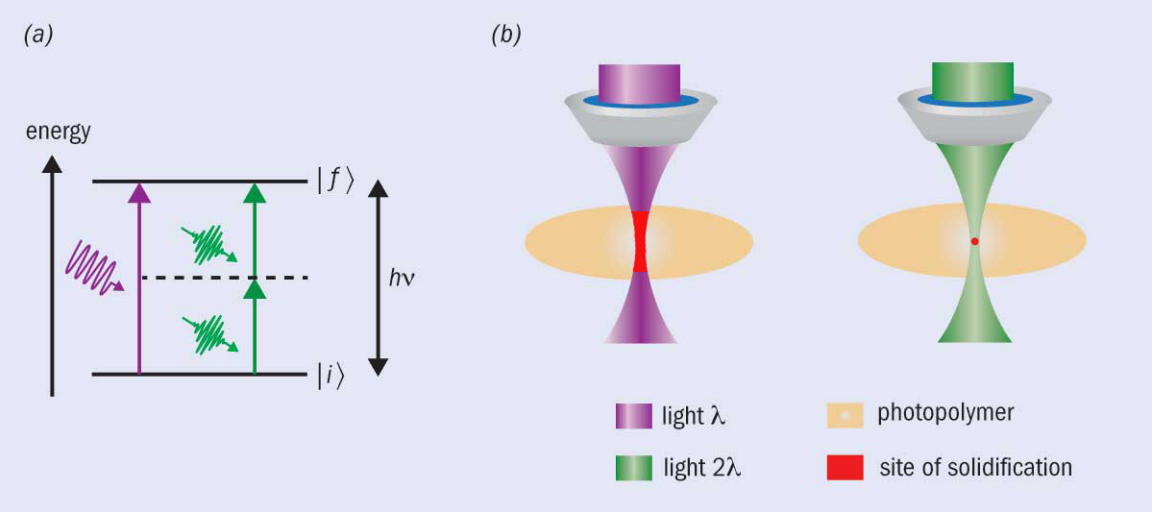

Figure 1.11: One-photon versus two-photon polymerization. Two photons of near infrared light are required to excite a molecule to a higher energy state instead of one photon of UV-light. Because of differences in light absorption, one-photon absorption takes place along a focalization cone whereas two-photon absorption only takes place in a small volume (voxel). Image adapted from [49].

While 2PP can achieve a high resolution of 100 nm and provides structural freedom, it also has some drawbacks. The most important one being the high production time, which forms a limitation in applications where many replicates are needed for statistical significance, such as in cell culture applications.

1.4.1 2PP for stem cell applications

Ricci and colleagues optimized the fabrication of a woodpile-based structure to investigate how pore size, pore density and overall structure dimensions affect stem cell homing in subsequent studies [50]. The scaffold geometry (see figure 1.12) was selected from eight previously tested ones, as the one most favoring spontaneous MSC homing and proliferation [51]. They found that MSCs invaded the scaffolds and that pluripotency of MSCs was maintained in the inner part, while in the surrounding 2D environment differentiation started to occur. Later they modified the scaffold surface with hydrogels to vary structure-mechanical properties: in all cases, 3D enhanced MSC differentiation with respect to 2D. Lastly, they showed that differentiation stopped in MSCs that had colonized the structures, hypothesizing that the structure induced changes in cytoskeletal tension.

Della Giustina et al. [52] fabricated a 2PP woodpile structure with methacrylated pullulan (a polysacharide derived from starch) in combination with PEGDA. The latter was added to modulate the mechanical properties and increase the degree of crosslinking. It was found that increasing the percentage of PEGDA increased the stiffness while decreasing the water absorption of the hydrogel. Water absorption was also influenced by the exposure time: longer exposure resulted in less absorption.

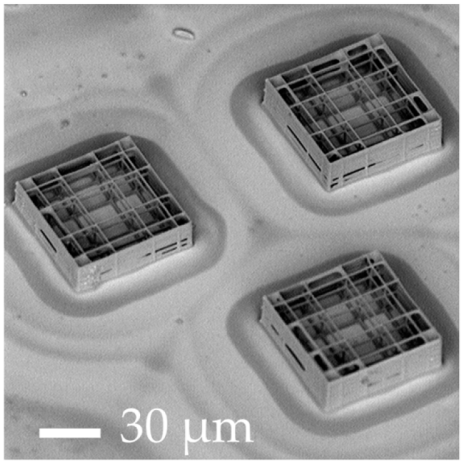

Figure 1.12: 2PP scaffold for stem cell homing of MSCs. MSCs inside the scaffold maintained pluripotency, whereas spontaneous differentiation started to occur in the surrounding 2D environment [50].

The structure achieved had a minimum feature size of 5 µm, and had a stiffness of 1.8 kPa. They demonstrated that the scaffolds were inert for cell adhesion, but biologically compatible and easily functionalizable with cell adhesive proteins. Under these conditions, successful cell cultures were established in 2D and 3D of both HEK cells and MSCs.

1.4.2 2PP for neural lineage applications

This paragraph will give some examples of different 2PP structures that were created for neural cell applications. Firstly, Turunen et al. [53] made tubular microtowers for human neuronal cells. The structure facilitated long-term (4 weeks) 3D culturing of human neuronal cells and supported neurite orientation and 3D network formation. They studied the distribution of cells within the towers, neuritic extension alignment and cell proliferation.

The structure was made by polymerizing the commercial polymer-ceramic hybrid Ormocomp and was afterwards coated with laminin. By performing force spectroscopy measurements with AFM at the upper rim of the microtower cylinder, the Young's modulus of the microtower was estimated to be 140 MPa. For comparison, the modulus of UV-cured Ormocomp thin films was measured to be 2.4 GPa, which is considerably larger. This difference is explained by the lower crosslinking degree of polymer chains achieved via 2PP versus UV-curing. Nevertheless, the structure was able to withstand the handling and cell culture procedures without major shape distortions.

An interesting observation was the capability of neural cells to form suspended bridges (see figure 1.13a) between adjacent towers and tower walls, with the longest bridge spanning a length of around 260 µm.

Among popular structures, we find the woodpile scaffold (see figure 1.13b). It was demonstrated by Accardo et al. that wood pile structures of IP-DIP and PEGDA could successfully be colonized by neuro2A cells, a fast-growing mouse neuroblastoma (cancerous) cell line [56] [54]. The cells were able to attach and develop neuritic extensions.

Lastly, Melissinaki et al. produced a sea shell structure (figure 1.13c), highlighting the endless design possibilities when creating a scaffold with 2PP [55]. PC12 cells successfully migrated and proliferated on the structures and aligned themselves with the structure geometry. Moreover, the cells extended neurites between multiple structures, forming an established network.

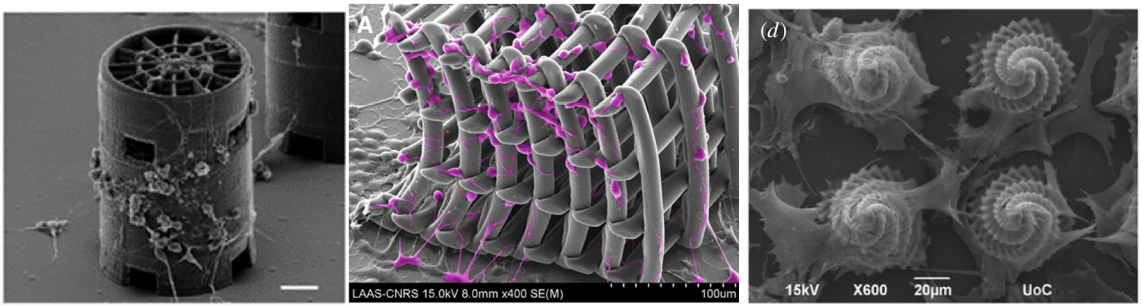

(a) (b) (c)

Figure 1.13: Examples of 2PP scaffolds for neural cell lines. (a) Tubular microtower with spiderweb structure on top, seeded with human neuronal cells. [53], scale bar represents 20 µm. (b) SEM image of 2PP scaffold fabricated from PEGDA, colonized by neuro2A cells [54]. (c) SEM image of two-photon polymerized sea shell structures, seeded with PC12 neural cells. Neurite projections were extended over more than one 3D object, forming interconnected networks [55].

1.5 Research objectives

Growing cells inside micro-engineered environments is still a relatively new field of research and there are still a lot of unknowns about the interactions of cells with these environments. Most research on neural differentiation has been focused so far only on 2D environments in the presence of chemical cues. However, in order to mimick the *in vivo* environment closer and be able to create more efficient microstructures, for example to increase the rate of differentiation, it is important to focus on 3D structures and the role of mechanobiology therein. While some mechanobiological effects regarding for example stiffness and topography have been discovered in 2D, the 3D research is relatively scarce as well as research into the effect of geometry, curvature and pore size of scaffolds. 2PP offers new opportunities here, since it can be used to fabricate 3D microstructures with finely controlled features that can be exactly replicated.

Initially, this master project was set to focus on the mechanobiological effect of material stiffness of a 3D two photon polymerized scaffold on the proliferation and neural differentiation of mESCs. Three different materials were planned to be tested in this regard, namely: IP-Dip, IP-VISIO and PEGDA. However, due to the encountered difficulties in terms of fabrication, cell culture, imaging protocols with IP-Dip structures and delays due to the pandemic, it was decided to focus on optimizing these aspects of the process instead of broadening the amount of materials. Therefore, the main objective of this research was shifted and a new research question was formulated:

What is the effect of lattice geometry of a 3D two photon polymerized scaffold on the neuronal differentiation of mESCs?

This main question was accompanied by four research sub-questions:

- What is a suitable seeding density for mESCs on a 3D 2PP scaffold?
- What is the effect of pore size of a 3D 2PP scaffold on the neuronal differentiation of mESCs?
- What is the effect of a curved lattice geometry versus a straight lattice geometry of a 3D 2PP scaffold on the neuronal differentiation of mESCs?
- What is the effect of the 3D geometry versus a 2D environment on the neuronal differentiation of mESCs?

Before starting neural differentiation, some preliminary experiments were required (see figure 1.14). First, the biocompatibility and setup of the experiment had to be tested with a different cell type that was less expensive and easier to handle in cell culture, in this case HeLa cells (human

cervical cancer cells) were available, and a simple structure: an array of pedestals. Next, we planned to test the HeLa cells in combination with the 3D scaffolds. After a successful culture, mESCs would be cultured in the 3D scaffolds, followed by a differentiation experiment utilizing biochemical cues to differentiate the mESCs into NPCs and lastly, into neurons. Unfortunately, this last step could not be carried out due to time constraints.

An additional investigation into the effect of curvature on HeLa cells on 2.5D structures was performed to gain a better understanding of the effect of curvature in a 3D lattice.

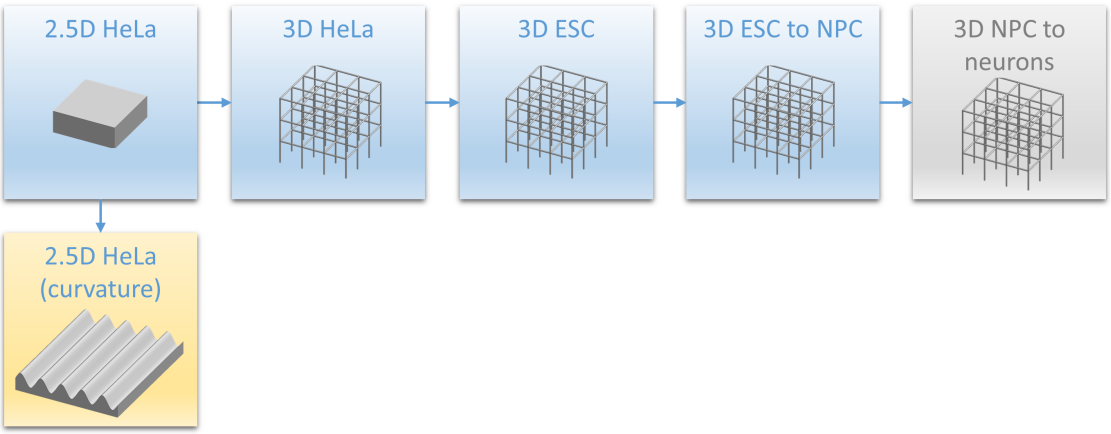

Figure 1.14: Project plan. The top row represents the originally planned project steps. The steps in the blue tiles were performed, however due to time constraints differentiation into neurons could not be carried out (grey tile). Later in the project a new research aspect was added: curvature in 2.5D (the yellow tile).

A large focus of this project was on the technical aspects of these 3D cell experiments ranging from fabrication to data analysis (see figure 1.15), such as the design and optimization of the 3D 2PP scaffolds, setting up the cell culture and imaging configurations and finding new ways to analyse the 3D cell culture images. This latter aspect was important as chemical assays (e.g. qPCR analysis or live/dead assays) were not an option in our case since a large part of the cells would reside on the flat surface of the substrate. Furthermore, since 3D cell culture within 2PP printed scaffolds is a relatively new field, there are no established common methods of data analysis yet and because the structure is 3D, imaging and analysis are not as straightforward as for 2D cell culture.

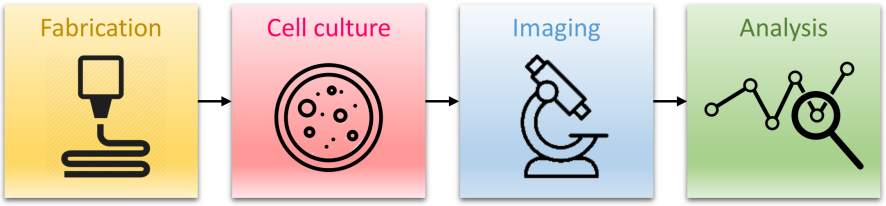

Figure 1.15: Experimental process.

The main characterization techniques used in this project were scanning electron microscopy and confocal imaging. The SEM images were used to inspect scaffold fabrication, cell morphology in the scaffolds and deformation of the scaffolds due to dehydration in the cell fixation process. The obtained confocal image stacks were analysed using Fiji (ImageJ) and Excel in order to find the volumetric occupance of cells within the scaffold, the location of nuclei and the height and area of ESC colonies. For the analysis of the 2.5D structures the area, aspect ratio and alignment of the cell nuclei were measured and compared.

Chapter 2

Materials and Methods

2.1 Fabrication of 3D microstructures via 2PP

All structures used in the following experiments were designed with the computer-aided design (CAD) program SOLIDWORKS and printed via two photon polymerization using the Nanoscribe Photonic Professional GT (PPGT, Nanoscribe GmbH & Co. KG). The principle of two photon polymerization was explained in section 1.4. The structures were made from a negative tone acrylate-based photoresin called IP-Dip (Nanoscribe GmbH & Co. KG) and printed on a fused silica substrate (dimensions 25 x 25 x 0.7 mm) with a 63x Zeiss objective (NA 1.4) in dip-in laser lithography (DiLL) configuration and galvo scan mode (see figure 2.1). After printing, the sample was developed for 25 minutes in PGMEA, followed by 5 minutes in IPA and then gently blow dried with an air gun. According to Nanoscribe, IP-Dip has a Young's modulus of 2.91 GPa after development and the material is known to be autofluorescent.

For the preliminary tests concerning sterilization and cell density on pedestals, no pre-treatment was used on the substrates before printing (other than wiping with acetone and IPA with a fine cloth under a fume hood). For all other experiments, the substrate was additionally plasma cleaned

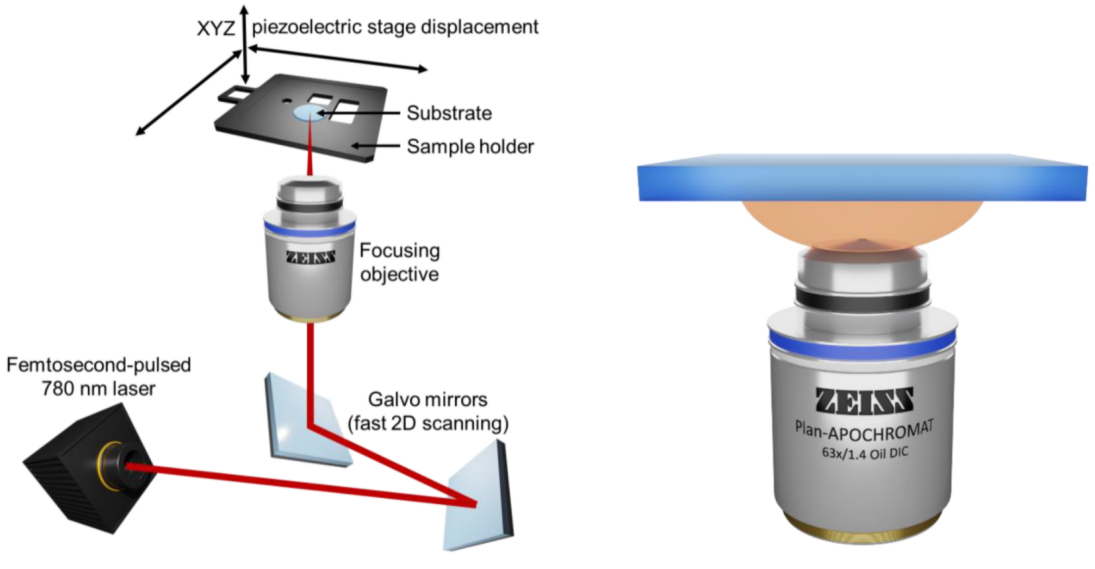

Figure 2.1: a) Schematic of two photon polymerization. b) Schematic of dip-in laser lithography (DiLL) configuration: the objective is directly immersed in the resin that is to be polymerized. Images adapted from [57].

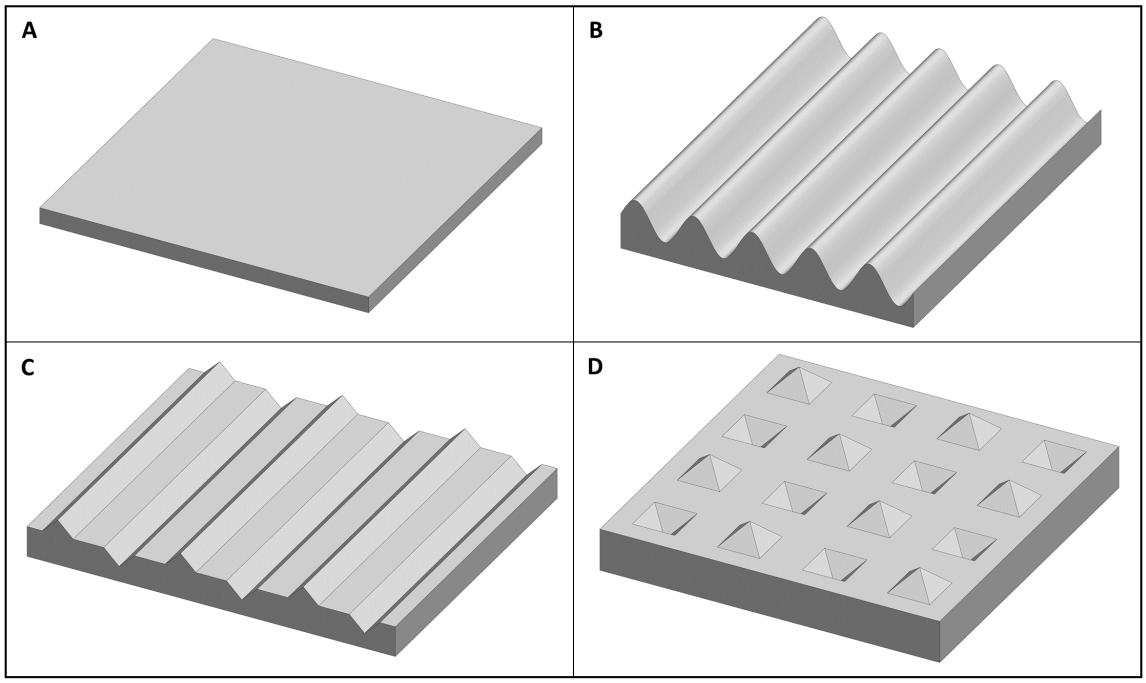

Figure 2.2: 2.5D scaffold designs for investigation of effect of curvature on HeLa cells and the difference between angular and smooth shapes. A) Flat pedestal of 500 x 500 x 25 µm. B) Sinusoidal scaffold with wavelength 100 µm and amplitude 25 µm. C) Triangular scaffold with triangular trenches and ridges of a height and depth of 25 µm. D) Pyramidal scaffold with alternating pyramids of 25 µm high and deep.

for 5 minutes with O_2 (Diener Femto Plasma Cleaner) to remove impurities and moisture from the substrate surface. Then the substrate was spincoated with the adhesion promoter OrmoPrime08 (purchased from Micro resist technology GmbH) and baked for 5 minutes at 150°C on a hot plate before applying IP-Dip. The settings for the spincoater were chosen as close as possible to the manufacturer's recommended specifications to obtain a film thickness of 130 ± 15 nm: spin speed 4000 rpm, time 60 s and acceleration 1080 rpm/s [58].

Important settings for 2PP printing are the slicing distance, hatching distance and scan speed. Before printing, the 3D model is divided into layers along the vertical direction (slices) and each layer is subdivided into a set of straight lines (hatching lines). The distance between two layers in the vertical direction is called the slicing distance and the distance between two lines within this layer is called the hatching distance. Printing occurs line for line, layer by layer. Furthermore, the laser power is set as a percentage of the total laser power of the Nanoscribe which is 50 mW. The structure designs are discussed in the following subsections and the details of each design can also be found in Appendix A and Appendix B.

2.1.1 Pedestals

For verifying the biocompatibility of IP-Dip we opted for a simple design: an array of solid pedestals of 140x140x50 µm (the maximum writing area in galvomode) (see figure A.1 and 2.4a). The pedestals were spaced 100 µm apart from each other in both directions (see figure 2.5). The writing parameters were: slicing distance of 0.4 µm, hatching distance 0.3 µm, scan speed 60 mm/s and laser power 90%. Each pedestal had a printing time of around 12 minutes.

2.1.2 2.5D structures

In order to investigate the effect of curvature on HeLa cells and the difference between angular (with straight edges) and smooth (with curved edges) shapes, a series of structures were designed

with features in the order of size of a HeLa cell. Here, we will discuss the structures that could be analysed. Unfortunately, some of them detached during the experiment (these structures were: rectangular lines, cylindrical lines and spherical hills and valleys, see Appendix A). All structures were designed with a minimum size of 500 x 500 µm to ensure statistical significance.

As a control we printed two large pedestals, both with an area of 500 x 500 µm but with a height of respectively 25 and 50 µm (see figure 2.2A). This was done in order to see whether or not the additional height had any effect on the cells' experienced stiffness.

An often used structure to research curvotaxis is a sine wave as it continuously has curvature. The designed sinusoidal scaffold had a wavelength of 100 µm and an amplitude of 25 µm. The overall size was 500 x 500 µm (see figure 2.2B).

To compare the smooth curves of the sine with an angular shape, we designed a triangular scaffold with alternating triangular trenches of 25 µm depth and triangular 'hills' of 25 µm high, with horizontal areas of 50 µm width in between (see figure 2.2C). The overall size was 500 x 600 µm.

Lastly, we designed a pyramidal shape as a counterpart of the scaffold with spherical hills and valleys, the latter could unfortunately not be analysed. The pyramidal scaffold consisted of alternating pyramid shaped pits (25 µm deep) and regular pyramids (25 µm high), spaced out 50 µm in both directions (see figure 2.2 D). The area in between the pyramids was horizontal and the overall size was 400 x 400 µm.

All 2.5D structures were printed with a slicing distance of 0.4 µm, hatching distance 0.3 µm, a scan speed of 60 mm/s, laser power 90% and galvo acceleration of 10 V/m^2 (see Appendix B). Since the structures were larger than the writing field of the Nanoscribe, we used stitching mode. In stitching mode, the design is divided into smaller blocks, which are then printed sequentially.

2.1.3 3D scaffolds

For the 3D scaffolds we wanted to compare two different geometries and two different pore sizes. An overview of the 3D scaffolds is given in table 2.1. The first design is a regular square lattice or cage and the second design is a circular shaped lattice, both with circular beams. The latter was inspired by the design of Trautmann et al. [59] and chosen for its organic shape and the presence of curvatures which in 2.5D have shown to have an effect on the behaviour of cells [39] [40] [42]. Both scaffold types were printed with a pore size of 15 and 30 µm, which both lie in the range of the cell size of the to be cultured cells. Namely, we measured that the nucleus diameter of HeLa cells cultured in 2D on a Petri dish had an average diameter of 20 µm and the diameter of mouse embryonic stem cells was reported to be 7-17 µm [60].

Table 2.1: Overview of 3D scaffolds and their design parameters: pore size, height (H), length (L), width (W) and beam diameter (b_d).

Name	Design	Pore size (µm)	H (µm)	L & W (µm)	d_b (µm)
BS	Square	30	97	98	2
SS	Square	15	65	65	1
SSB	Square	15	97	97	1
BC	Circular	29	91	91	1
BCF	Circular	28	92	92	2
SC	Circular	14	46	46	1
SCB	Circular	14	91	91	1

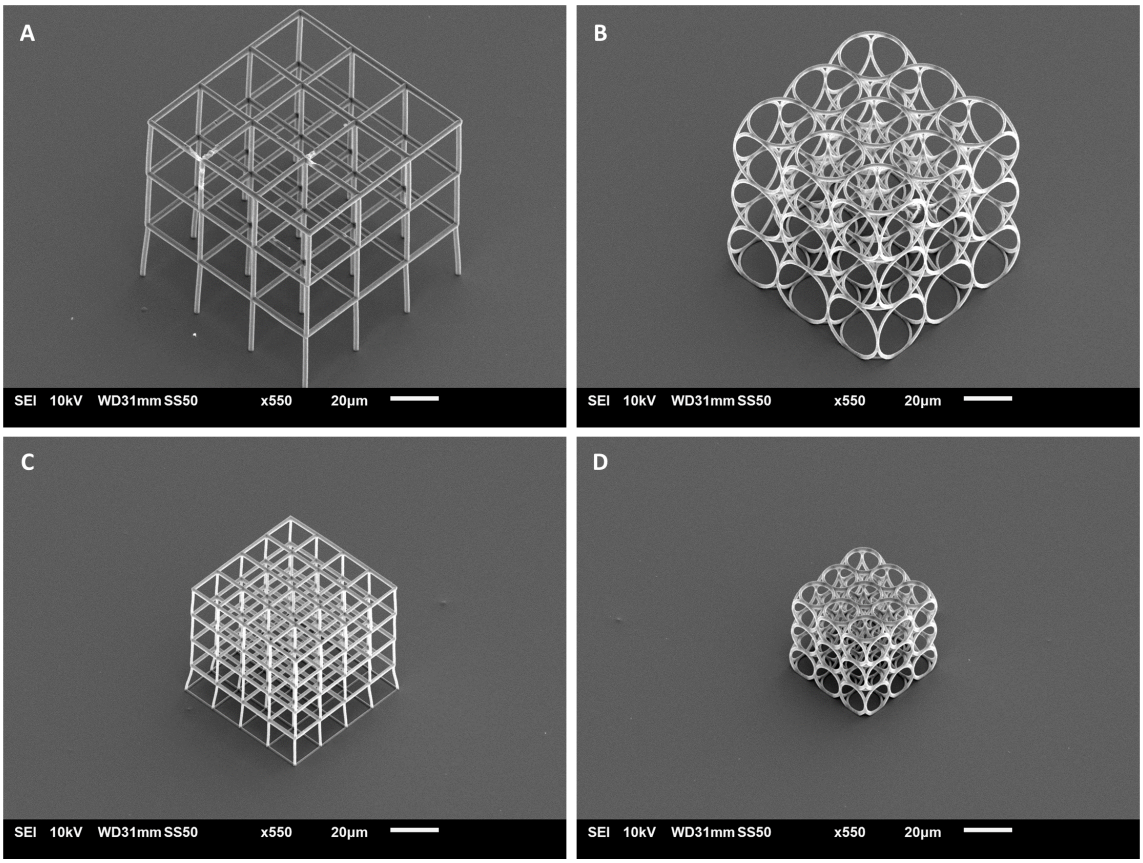

Figure 2.3: SEM images of 3D scaffold designs for cell culture. A) Big square scaffold (BS), pore size: 30 µm and beam diameter 2 µm. B) Big circular scaffold (BC), pore size: 29 µm and beam diameter 1 µm. C) Small square scaffold (SS), pore size: 15 µm and beam diameter 1 µm. D) Small circular scaffold (SC), pore size: 14 µm and beam diameter 1 µm. Scalebar = 20 µm.

The square scaffold with a pore size of 30 µm (BS) had a beam diameter of 2 µm and overall dimensions of 98 x 98 x 97 µm (see figure 2.3A). The beam diameter was larger than that of the other scaffolds, in order to increase stability. The square scaffold with pore size 15 µm (SS) had a beam diameter of 1 µm and overall dimensions of 65 x 65 x 65 µm (see figure 2.3C).

The large circular scaffold (BC) had a pore diameter of 29 µm, a beam size of 1 µm and overall dimensions of 91 x 91 x 91 µm (see figure 2.3B). The smaller circular scaffold (SC) had a pore diameter of 14 µm, a beam size of 1 µm and overall dimensions of 46 x 46 x 46 µm (see figure 2.3D).

The four aforementioned scaffolds were all printed with a slicing distance of 0.3, a hatching distance of 0.2, scan speed 10 mm/s and laser power 80%. The printing time was in the order of a few minutes.

Later, we also introduced some variations to these scaffolds. First, we created the same lattices with pore size 15 µm but with the same volume as the larger pore sized scaffolds for a fairer comparison, namely the square SSB scaffold (see figure C.1A in the Appendix) and the circular SCB scaffold (C.1B). These scaffolds were only cultured with HeLa cells. Furthermore, it was noticed that the circular scaffold with diameter 29 µm showed signs of instability by incidentally deforming. Therefore the same scaffold was also printed with thicker beams with a diameter of 2 µm (BCF, see figure C.1D), this scaffold was first introduced in the ESC experiments. Lastly, a new design was proposed and validated for the large square scaffold to increase the adhesion to the substrate as it occasionally detached from the surface during cell culture (see figure C.1C).

Please note that for all structures discussed here we mentioned the dimensions as they were designed. However, they did undergo some shrinkage during printing which is a known occurrence for 2PP of IP-Dip, and also 2PP in general.

2.2 Cell culture

Prior to seeding cells, the substrates with the printed 3D scaffolds were sterilized under a UV lamp (CRF/UV 15-A, from Esco (T355)) in the cell culture hood for 1 hour. Then a Press-to-Seal (Sigma-Aldrich/Merck, 9 mm diameter and 0.9 mm thick), a silicone isolator with adhesive on one side, was pressed onto the middle of each substrate with the adhesive side downwards, creating a well of 57 µL around the array of scaffolds. This was done in order to limit the required amount of cells and media and provide a convenient configuration for confocal imaging. Afterwards, 100 µL of 70% EtOH was added to the well. After 5 minutes the EtOH was removed and this process was repeated 2 times. Then the well was washed with 100 µL of PBS for 3-4 minutes. The PBS was removed and this was repeated 3 times (total of 4 washes). Lastly, for experiments with mESCs, the substrates were coated with 0.1% (w/v) gelatin for 30 minutes at room temperature, to increase cell adhesion to the substrate and scaffolds. For the experiments with HeLa cells, the substrates were coated with 0.2% (w/v) gelatin.

For cell seeding, cells were trypsinized and counted. Cells were seeded directly onto the scaffolds at various densities (see table 2.2).

Cell culture was performed at the department of Bionanoscience (TU Delft). For initial sterilization tests, HEK293-T (human embryonic kidney) cells were used. In further experiments HeLa (cervical cancer) cells were chosen. Lastly, some preliminary experiments were performed with mESCs.

HEK293-T cells were purchased from Leibniz Institute DSMZ-German Collection of Microorganisms and Cell Cultures (DSMZ, ACC 635). HEK293-T were cultured in DMEM/F12 with GlutaMAX (Gibco) supplemented with 10% FBS (Gibco) and 1% Penicillin/Streptomycin (Pen/Strep, Gibco). HeLa cells were purchased from DSMZ and cultured in DMEM/F12+GlutaMAX (Gibco) supplemented with 10% FBS and 1% Pen/Strep.
The mESCs were a kind gift from Hyun Youklab (Delft University) and cultured according to Gaspard et al. (2009) [61] and Gazina et al. (2018) [62].
All cell types were grown at 37°C and 5% CO_2.

Table 2.2: Cell seeding densities per experiment. Most experiments were carried out using the Press-to-Seal. Experiments denoted with an asterisk (*) were carried out in a 10-cm petri dish.

Experiment	Cell type	Structure type	Seeding density (cells/cm^2)
Biocompatibility	HeLa	Pedestals	20,000 - 80,000 - 160,000
SEM dehydration*	HeLa	Scaffolds	25,000
Curvature*	HeLa	2.5D structures	25,000
Occupancy	HeLa	Scaffolds	120,000 - 160,000
Occupancy*	HeLa	Scaffolds	25,000
Occupancy	mESC	Scaffolds	30,000 - 80,000 - 160,000
Differentiation	mESC	Scaffolds	30,000 - 80,000

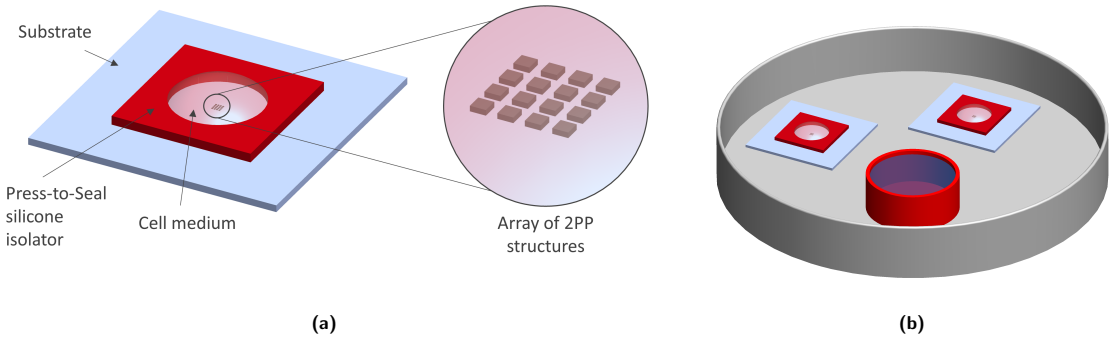

Figure 2.4: Schematic of sample and experiment configuration for growing cells on 2PP structures. a) Substrate with printed array of structures with Press-to-Seal and cell medium. b) Experimental setup during cell culture. Substrates and a container with cell medium are placed together in a petridish. Lid of petridish is not depicted but was placed on top during cell culture.

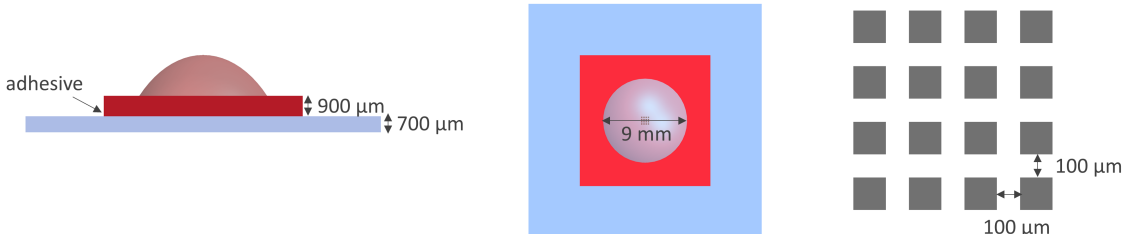

Figure 2.5: Schematic of sample configuration with dimensions. For the biocompatibility experiments an array of IP-Dip pedestals was printed, spaced spaced 100 µm apart in horizontal and vertical direction. In later experiments scaffolds were placed in a similar array.

HEK-293T, HeLa and mESCs were incubated for 2 days except for in the differentiation experiment in which mESCs were cultured for 5 days in differentiation medium. The sample configuration is depicted in figure 2.4a and the dimensions can be found in figure 2.5. A small container with ≈ 5 mL cell medium was placed together with the substrates in a petridish to keep the humidity up in order to prevent evaporation of medium from inside the wells (see figure 2.4b).

2.3 Immunofluorescence imaging

2.3.1 Immunofluorescence staining

Cells were fixed with 4% (w/v) paraformaldehyde (PFA; BosterBio) for 10 minutes. After fixation, cells were thoroughly washed 3 times for 5 minutes with phosphate buffer saline (1x PBS) and permeabilized with 0.5% Triton X-100 in PBS for 10 minutes. Cells were then blocked with 5% normal goat serum (Life Technologies) and 0.05% Tween20 in PBS for 30 minutes. Cells were incubated with 0.1% Alexa 568 Phalloidin (A12380, Invitrogen) (F-actin staining) in blocking solution for 1h at room temperature. After washing 3 times in 1x PBS and a final wash in MilliQ, 100 µl of Vectashield mounting medium with Dapi (Vector Laboratories, nucleus staining) was inserted to the well and a coverslip (thickness 170 µm) was mounted on top of the seal. In some cases this coverslip was glued down. The samples were stored in a fridge at 4°C before imaging.
In the case of the mESC differentiation experiment, an extra immunofluorescent marker was applied to indicate differentiation into NPCs. After blocking the cells with 5% normal goat serum (Life Technologies) and 0.05% Tween20 in PBS for 30 minutes, cells were incubated with primary antibody Nestin in blocking solution for 1 hour. Next, the cells were incubated with 0.1% Alexa 488 (anti rabbit, secondary antibody) and 0.1% Alexa 568 Phalloidin (A12380, Invitrogen) (F-actin staining) in

blocking solution for 1h at room temperature. The rest of the protocol was identical to the one above.

2.3.2 Confocal imaging configurations

In order to create the best 3D reconstruction possible for post-imaging analysis, imaging conditions need to be optimized to provide the best resolution. Because the structure is 3D and the light has to travel a distance through medium, diffraction, scattering and shadowing effects are present. Differences in refractive index (see table 2.3) between the different components in the configuration contribute to this, therefore different methods were explored where the objective was to minimize the difference in refractive index between the mounting medium, IP-Dip and when applicable, the coverslip. Most important is to obtain a better signal deep inside the scaffold (near the substrate) where shadow and scattering effects are largely present and obstruct the visibility of cells in that region.

There were two different confocal microscopes available to us, namely the Leica SP5 Intravital (equiped with multiphoton laser), available at Erasmus Optical Imaging Centre (Erasmus MC) and the Nikon Eclipse Ti inverted microscope with A1R confocal module at the Kavli Nanolab Imaging Centre (Department of Bionanoscience, TU Delft).

With the inverted Nikon microscope and the sample configuration with a press-to-seal, Vectashield and a coverslip, the options of objectives were limited to a 20x dry objective, numerical aperture (NA) 0.75 and working distance (WD) 1 mm (see figure 2.6A). This configuration could not reach high enough magnification for a good 3D reconstruction as no optical zoom was available. Therefore this configuration was only used for stack-analysis purposes as described in section 2.5 and was not suitable for 3D reconstruction.
The used laser lines were: 405 (DAPI), 488 (scaffold/Nestin) and 561 nm (phalloidin) and the respective filter cubes: 450/50, 525/50 and 595/50.
This configuration was used to image a sample with HeLa cells on scaffolds and a substrate with ESC on scaffolds, which were stained with DAPI and phalloidin.

At Erasmus, several configurations were tried. A water dipping objective (20x, NA 1.0 and WD 1.95mm) was combined with the regular sample configuration using a press-to-seal spacer of 900 µm thickness (see 2.6C) and the configuration where the seal was replaced by a perforated plastic sheet

Table 2.3: Refractive index of different materials used for confocal imaging.

Material	Refractive Index
BABB	1.559
IP-Dip	1.556
Immersion oil	1.518
Glass (coverslip)	1.517
IP-Visio	1.514
Vectashield	1.452
ProLong Gold (after curing)	1.46
PBS	1.335
Water	1.333
Mowiol	1.41-1.49

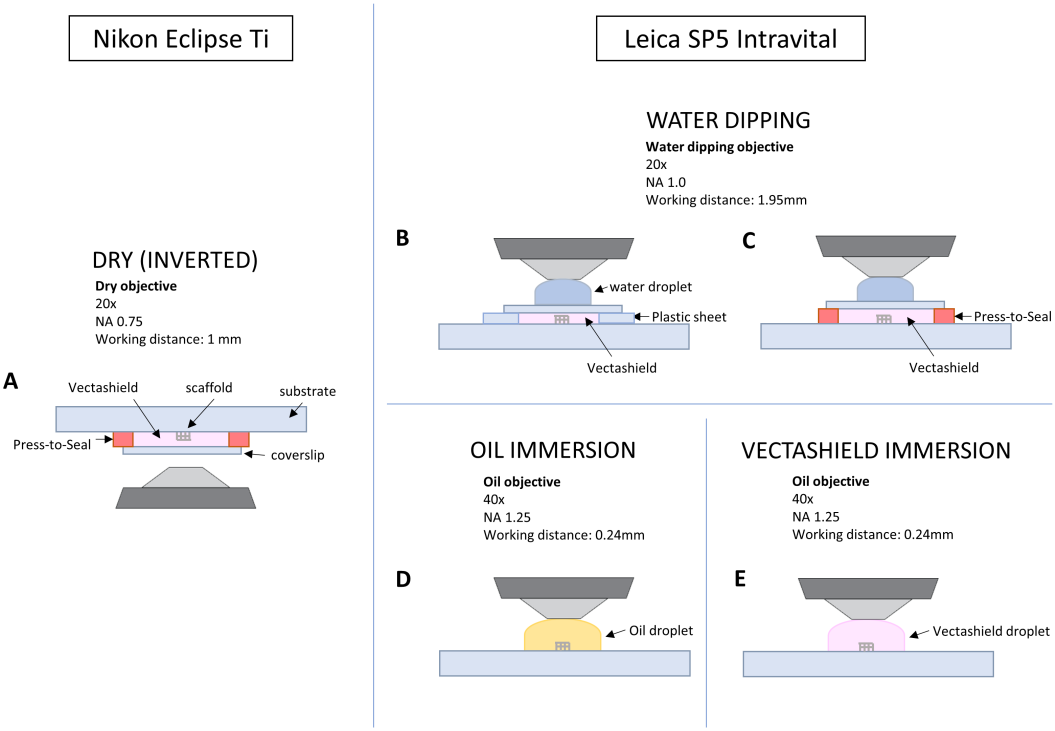

Figure 2.6: Confocal imaging configurations

of 180 µm thickness, which decreased the distance that had to be travelled by the light by a factor of 5 (see 2.6B). These configurations were applied to substrates with HeLa cells on scaffolds and later also for ESCs and differentiated ESCs on scaffolds, all stained with DAPI and phalloidin.

Furthermore, two configurations were tried with an oil immersion objective (40x, NA 1.25 and WD 0.24 mm). In the first one, a droplet of oil (type F immersion liquid, Leica Microsystems) was deposited on the scaffolds after which the objective was immersed into the oil (see 2.6D). This method was tried with a bare sample (no cells), then a sample with HeLa cells (only stained with phalloidin) and lastly with HeLa cells that were stained with phalloidin and NucBlue (an alternative for DAPI to stain nuclei blue, obtained from Thermofisher). In the second one, the oil immersion configuration was tried with Vectashield instead of oil (see 2.6E) on a sample with HeLa cells stained with DAPI and phalloidin.

In configurations B-E, an optical zoom was employed: 4x for configuration B and C and 3x for configuration D and E. The employed excitation lasers were 405, 488 and 561 nm. The emission filters were set to the following ranges: 415-480, 500-550 and 570-625 nm.

Two-photon imaging was also explored. When using two-photon microscopy, fluorophores are excited by simultaneously absorbing two photons of a long (typically near infrared) wavelength instead of a single photon of shorter wavelength as during confocal imaging. Since the two photons must be absorbed almost simultaneously, excitation is only achieved in the focal plane and background noise which has the advantage of reduced background noise.

2.4 Scanning electron microscopy

2.4.1 Sample preparation for SEM

The samples for SEM were prepared according to the protocol from the department of biomechanical engineering (TU Delft). This protocol also formed the baseline for the dehydration experiment described in 3.1.4. All steps were performed under a fume hood.

The cells were fixed in the wells formed by the press-to-seal in 100 µL of 1%GA-4%PFA in PBS for 10 minutes. The fixative was then removed and the sample washed twice for 5 minutes in 100 µL of deionised water (DIW). Lastly, the cells were dehydrated by a graded series of ethanol washes in DIW (each 100 µL): 50% for 15 minutes, 70% for 20 minutes and 96% (v/v) for 20 minutes. The sample was left to dry for three hours under the fume hood. During the protocol the media were always removed or inserted by pipette near the inner rim of the well to prevent damage to the scaffolds placed in the center.
Shortly before imaging, the samples were sputter coated (Sputter Coater JEOL JFC-1300) with gold in three consecutive sessions of 30 seconds at 20 mA, each time in a different sample mounting configuration. First on a horizontal holder (figure 2.7a), then on a 45 degree holder (figure 2.7b) with one corner of the substrate facing downwards (figure 2.7b) and lastly on a 45 degree holder with the opposite corner facing downwards. This ensured an even covering of the 3D scaffolds. The seal was not removed before sputter coating as it did not cause a hindrance during imaging and removal increases the risk of accidentally damaging the sample.
During imaging the sample was mounted on a horizontal holder with a carbon tab. For pictures under a 45 degree angle the SEM stage was tilted. In order to image the side view of the scaffolds in the dehydration experiment (see section 2.4.2), a 90 degree holder was used (see figure 2.7d). In this case, the samples were cultured without a seal and the SEM stage had to be slightly tilted (to a few degrees) in order to avoid foreground noise.
Most images were taken with an acceleration voltage of 10 kV and with a spotsize of 30.

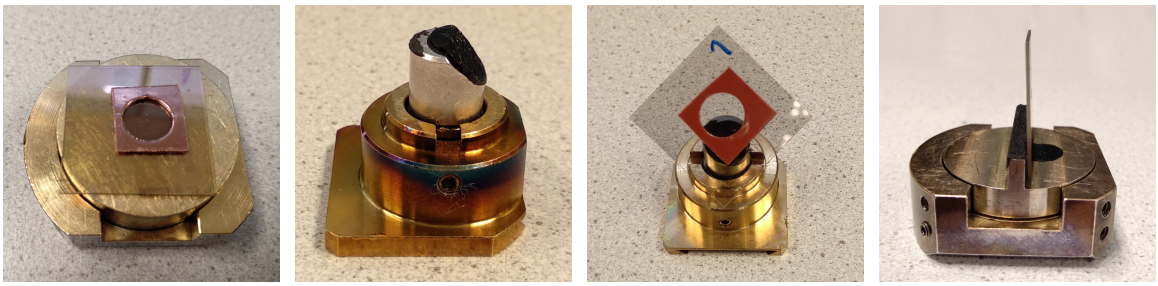

(a) (b) (c) (d)

Figure 2.7: Sample holders used for gold sputter coating of samples and during SEM imaging: (a) sample mounted on horizontal holder for sputter coating and imaging, (b) 45°-holder used during sputter coating, (c) sample mounted with one corner of the substrate facing downwards on 45°-holder for sputter coating and (d) sample mounted on 90°-holder for imaging scaffolds from the side.

2.4.2 SEM dehydration experiment

In order to find the SEM preparation protocol for the 3D scaffolds that induces the least shrinkage of cells and subsequent deformation of the scaffold, several different protocols were compared (see table 2.4).

The effect of using HMDS as a last dehydration step was explored, as well as the effect of using 2.5% GA or 4%PFA-1%GA, the fixation time and the difference between ethanol in DIW versus ethanol in PBS. Protocol 1 was described in section 2.4.1 and seen as the baseline. In the cases where HMDS was used, the sample was moved from the cell fixation lab to the chemical lab in the same building while immersed in 96% ethanol, the last step in the ethanol series. The sample was then immersed in HMDS (Sigma) and left to dry under the fume hood.

2.5 Analytical approaches

In this section the most important analysis algorithms will be explained. Data was mostly obtained using Fiji/ImageJ and later analyzed in Microsoft Excel.

Table 2.4: SEM preparation protocols used to investigate the effect on scaffold deformation due to cell shrinkage during dehydration. The graded ethanol series were either created with deionised water (DIW) or PBS. The duration of each step in the ethanol series for all protocols was: 15, 20 and 20 minutes respectively.

Protocol	Fixative	Fixation time	Washing	Ethanol series	HMDS (yes/no)
1	1%GA-4%PFA	10 min	2x 5min DIW	50, 70, 95% (DIW)	no
2	1%GA-4%PFA	10 min	2x 5min DIW	50, 70, 95% (DIW)	yes
3	1%GA-4%PFA	10 min	2x 5min PBS	50, 70, 95% (PBS)	no
4	2.5%GA	10 min	2x 5min DIW	50, 70, 95% (DIW)	no
5	2.5%GA	10 min	2x 5min DIW	50, 70, 95% (DIW)	yes
6	2.5%GA	4 h	2x 5min DIW	50, 70, 95% (DIW)	no
7	2.5%GA	4 h	2x 5min DIW	50, 70, 95% (DIW)	yes

2.5.1 Characterization of scaffold deformation

In this experiment samples that had undergone cell culture, fixation and dehydration were compared to a control: a substrate that did not undergo cell culture or any other protocol after development of the printed scaffolds. All SEM pictures of the same scaffold type were taken with the same magnification. Since the shrinkage of cells is directly related to the deformation of the scaffolds, this deformation was treated as a measure of cell shrinkage since it could be easily analysed.

A set of N points are defined on the scaffold. For the square scaffold, this means in every corner (see figure 2.8) resulting in a total of $N = 16$ points. For each protocol and each scaffold, these points were manually defined (but always in the same order) in Fiji/ImageJ. Through a macro, the coordinates of all points were measured (in µm) in terms of x and y coordinates: X_{ij} and Y_{ij}, where i is the number of the scaffold and j is the number of the point.

From the control set, one scaffold was chosen as the "ultimate control", against which all other scaffolds (including the 3 others from the control group to account for variations in fabrication) were compared. We will further refer to this ultimate control scaffold as S_0. Other scaffolds will be denoted as S_i, where i stands for the number of the scaffold.

In order to be able to compare scaffolds, the coordinates must be transformed such that the

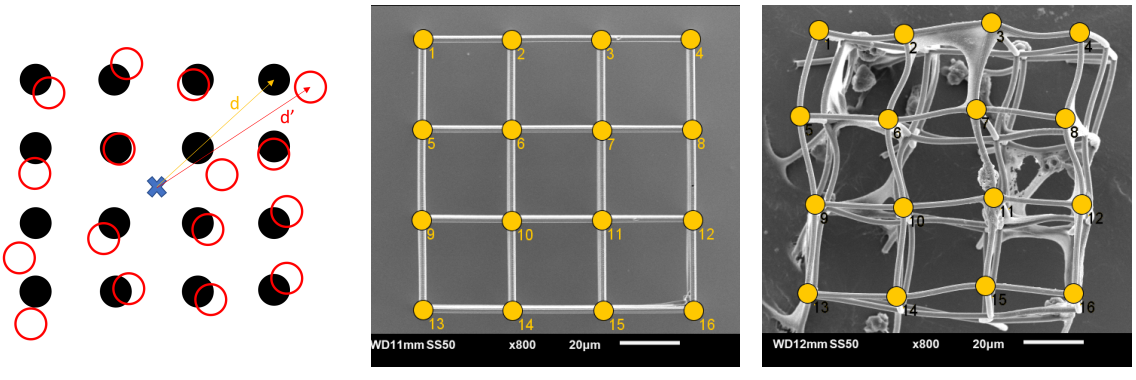

(a) (b) (c)

Figure 2.8: a) Method for calculating scaffold deformation after SEM fixation and dehydration. b) Points 1-16 defined on the control. c) Point 1-16 defined on a deformed scaffold.

centre of each scaffold coincides. This was performed in Excel. First a centre must be defined for each scaffold which is done by averaging the coordinates of certain points (for the big square scaffold these are the 4 outer corners):

$$\begin{aligned} x_{ci} &= \frac{X_{i1} + X_{i4} + X_{i13} + X_{i16}}{4} \\ y_{ci} &= \frac{Y_{i1} + Y_{i4} + Y_{i13} + Y_{i16}}{4} \end{aligned} \tag{2.1}$$

Then the values of this center point are subtracted from the other coordinate values such that the centre of each scaffold is at (0,0) and the new coordinates are x_{ij} and y_{ij}:

$$\begin{aligned} x_{ij} &= X_{ij} - x_{ci} \\ y_{ij} &= Y_{ij} - y_{ci} \end{aligned} \tag{2.2}$$

Next, the distance d from the centre of S_0 to point number j of S_0 and the distance d' from the centre of S_i to point j of S_i are calculated for $j = 1$ to N.

$$d_j = \sqrt{{x_{0j}}^2 + {y_{0j}}^2} \tag{2.3}$$

$$d'_j = \sqrt{{x_{ij}}^2 + {y_{ij}}^2} \tag{2.4}$$

The difference between d and d' is calculated, divided by d and multiplied by 100%. This results in a percentage of deformation D for point j with respect to the distance of point j of control S_0 to the centre of S_0. This method of calculating the deformation compensates for any pure rotation of scaffold.

$$D_j(\%) = \frac{|d'_j - d_j|}{d_j} \times 100\% \tag{2.5}$$

For each scaffold S_i, the deformation per point is averaged over the total number of points N:

$$D_i(\%) = \frac{\sum_{j=1}^{N} D_j}{N} \tag{2.6}$$

Per SEM protocol, these percentages are again averaged over the total amount of scaffolds of that type (in this case 4 as each substrate contains 4 scaffolds of each type) to result in one deformation value per sample preparation protocol.

The same procedure is followed for the other scaffold types and the sideview of the scaffolds. In some cases the same scaffold could be imaged from two sides, in this case these values were averaged first before averaging the scaffolds per method.

2.5.2 Comparison of confocal imaging configurations

In order to analyze and compare the quality of different confocal imaging methods of IP-Dip scaffolds (with cells) that are mentioned in section 2.3, we looked at the mean intensity of each stack layer in the green channel. This specific channel was chosen as it only contains the scaffold, therefore fluorescence signals from the cells are not present. It was important to use stacks that are cropped around the borders of each scaffold in order to maximize the mean intensity signal which decreases if there is a large surrounding area where there is no signal. After cropping the stack, the mean intensity of the green channel is measured for each slice of the stack via a for loop in a Fiji macro.

2.5.3 Characterization of cells on the 2.5D structures

In order to analyze the cells on 2.5D structures and look into the effect of curvature, we wanted to focus on the nuclei of the cells on these structures. This was done using the 'analyze particles' function in Fiji/ImageJ on a thresholded z-projection of the nuclei (2D). The measured variables were the area of the particles, the orientation of the major axis of a fitted ellipse and the aspect ratio of this fitted ellipse (see figure 2.9).

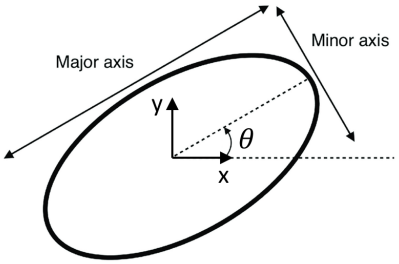

Figure 2.9: Definition of major and minor axis of a fitted ellipse around a nucleus. The angle between the major axis and the horizontal x-axis is denoted by θ and is measured to investigate nucleus alignment.

Since the nuclei were hardly distinguishable from the autofluorescent IP-Dip of the 2.5D structures, some manipulation had to be carried out on the confocal stacks in order to obtain a clear view of the nuclei in the z-projection. First, the green stack was subtracted from the blue stack, after which a sum z-projection was made. Unfortunately the structures were not evenly bright, therefore complicating the use of a threshold. This was solved by transferring the image to Adobe Photoshop where the nuclei were traced manually. Nuclei that were not surrounded by phalloidin/actin (red channel) were assumed dead and omitted during analysis. Lastly, the images were fed back into Fiji/ImageJ where a threshold now could be applied and the nuclei were analyzed. In order to make a fair comparison with cells on an empty part of the substrate, the same methods were applied there instead of directly analyzing the particles in Fiji/ImageJ.

In the case where nuclei were assigned to certain regions of the structure, this was done manually. When nuclei lay on the border of two regions, the nucleus was assigned to the region where the majority of its projected surface was located.

2.5.4 3D reconstruction of images

3D reconstructions of the acquired confocal stacks were made in Fiji/ImageJ using the 3D viewer, in some cases a macro was used to enhance the 3D image.

2.5.5 Characterization of cells in the 3D scaffolds (HeLa, ESCs)

In order to analyze cells inside the scaffolds and their reaction to different geometries, we looked at different parameters: the percentage of phalloidin/DAPI in the z-projection of the scaffold stacks, the percentage of phalloidin/DAPI in the total stack volume (volumetric occupancy), the surrounding cell density on the substrate and the location and number of cells in big square scaffolds.

An important decision in the z-projection and volumetric occupancy was which threshold algorithm to use as this could have great effects on the results. In Appendix D one can find a comparison of algorithms.

2.5.5.1 Z-projection phalloidin and DAPI occupancy

As a first indication of the number of cells inside the scaffolds, we looked at the percentage of area that was occupied by phalloidin (red channel) or DAPI (blue channel) in the maximum z-projection

of each scaffold. A maximum z-projection is a technique that turns a stack of images (taken along the z-axis) into a single 2D image by taking the brightest pixel in each layer and displaying that pixel intensity value in the final 2D image. This was performed via a Fiji/ImageJ sequence that is depicted in 2.10. First, images that were taken above and below the scaffold were removed from the stack in order to eliminate noise. The remaining substack thus only contained slices taken from the bottom of the scaffold until the top of the scaffold.

Subsequently, a region of interest (ROI) was drawn around the scaffold area and the area of this ROI was measured to obtain the total scaffold area. A maximum z-projection was done on the stack after which either the red or the blue channel was isolated depending on whether we were analysing phalloidin or DAPI. For analysis of DAPI, the results had to be corrected for the autofluorescence of the scaffold itself, which was done by subtracting the green channel (only scaffold visible) from the blue channel (scaffold plus nuclei) first.
Then a threshold was applied, turning the picture into black and white pixels. A selection was made of the white pixels and this was then measured to obtain the area of phalloidin or DAPI in the z-projection of the scaffold which was then divided by the total scaffold area to obtain the z-projection occupancy (%). The threshold was different for the red or the blue channel and had to be set by the user.

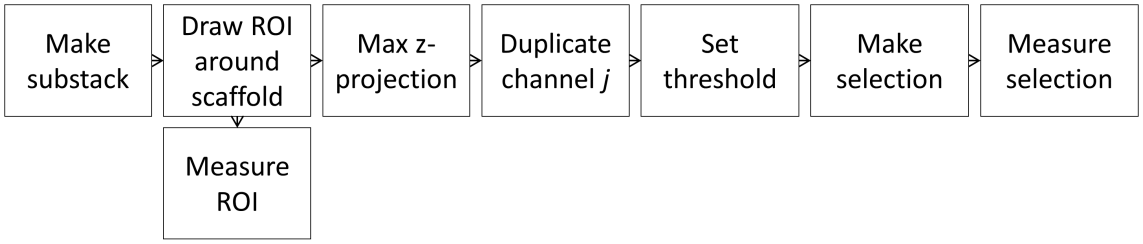

Figure 2.10: Fiji workflow for obtaining the phalloidin (j=3) and DAPI (j=1) occupancy (%) of scaffolds in maximum z-projection of stack.

2.5.5.2 Volumetric phalloidin occupancy

For the volumetric occupancy, the percentage of volume occupied by phalloidin, an algorithm was used that was based on the same principles as the z-projection macro explained above. However, here we made use of a for loop to go through each slice separately (see figure 2.11). Since the overall pixel intensity gets significantly lower as you get deeper into the scaffold, a constant threshold value would not be suitable. After trying different automatic threshold algorithms that were pre-programmed in Fiji (see Appendix D), it was decided to use a linearly varying threshold for which the values in the top and bottom slice had to be set by the user.

The volumetric occupancy O_V is finally calculated using the following equation, where A_i is the

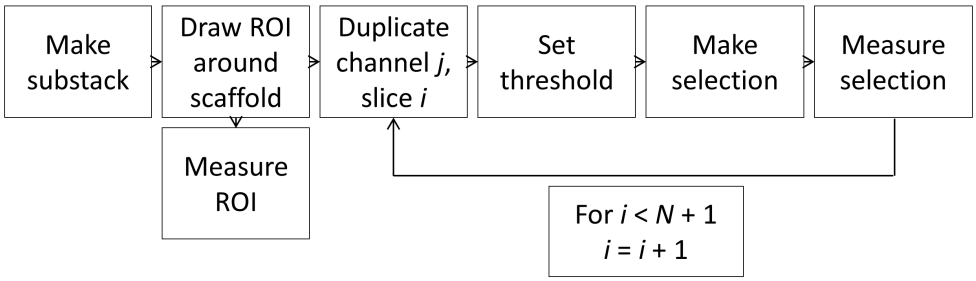

Figure 2.11: Fiji workflow for obtaining the volumetric phalloidin occupancy (%) of scaffolds. N is the total number of slices in a scaffold stack.

area of phalloidin in slice i, N is the total number of slices in a stack and A_{ROI} is the total scaffold or ROI area.

$$O_V(\%) = \frac{\sum_{i=1}^{N} A_i}{N \times A_{ROI}} \times 100\% \tag{2.7}$$

2.6.5.3 Surrounding cell density

The surrounding cell density around the scaffolds is obtained by using particle analysis (Fiji/ImageJ) on a wideview image (zoom 1x) of the surface around the scaffold, where the scaffold itself is excluded from the analysis. Via particle analysis the nuclei are counted and then divided by the total area to obtain the density.

2.6.5.4 Cell location in big square scaffold

For the big square and circular scaffolds, it was possible to count the cells manually by counting their nuclei in the slices of the stack, taking care not to count the same nucleus twice. Unfortunately, this counting was only possible for stacks imaged with the Leica SP5 Intravital. The scaffolds imaged with the Nikon were imaged with a much lower magnification and therefore the resolution was not good enough for distinguishing separate nuclei. The scaffolds with smaller pore size that were imaged with the Leica SP5 Intravital could also not be counted this way as shadowing effects in the lower layers made distinction of nuclei impossible.

2.5.6 Characterization of ESC colonies

In the ESC experiment, cell colonies inside and outside of scaffolds were compared. This was performed by analysing confocal stacks containing scaffolds and stacks of colonies in regions without scaffolds. All stacks were acquired from the same substrate. The macro for analyzing the colonies consists of two parts. In the first part, the colonies are identified and numbered and the outline of the colonies is saved as a ROI (see figure 2.12). This is done by looking at the z-projection of the blue channel, i.e. the nuclei. After setting a threshold, the image is turned black and white and if needed, autofluorescent signal from empty regions of the scaffold is manually removed using the ImageJ paint brush/bucket tool. The binary function 'fill holes' is then used to fill any holes within the colony with white pixels so that the total area of the colonies would be measured (the 'measure' funtion only measures the amount of white pixels within the ROI). Particle analysis is then used on particles with an area larger than 1000 µm^2 (which is equivalent to a colony of around 8 cells) and the regions are numbered and saved. In the second part of the macro, we selected the red channel of the stack and measured the maximum intensity of each slice within the colony. This step was repeated for all earlier identified colonies in the regions without a scaffold and was needed to determine the top height of the colonies.
For the colonies that are attached to or occupying the scaffolds, a correction was first made to the red channel of the stack since the scaffold was slightly fluorescent in this channel as well. Therefore, the the green stack was subtracted from the red stack before analysing the maximum intensity of each slice within the colony region.
The bottom slice of the stack was determined by the user by looking at where the F-actin (phalloidin) on the surface was most in focus. An appropriate cut off intensity also had to be chosen for the top height of the colonies. For most scaffolds this was determined by taking the first slice from the top where the maximum intensity of the region reached the maximum value of 255. In cases where this maximum intensity was not reached, the top slice was determined by the user. The rest of the analysis of the acquired data was carried out in Excel, where the height and projected area of each mESC colony was calculated based on the chosen bottom and top slice of each colony.

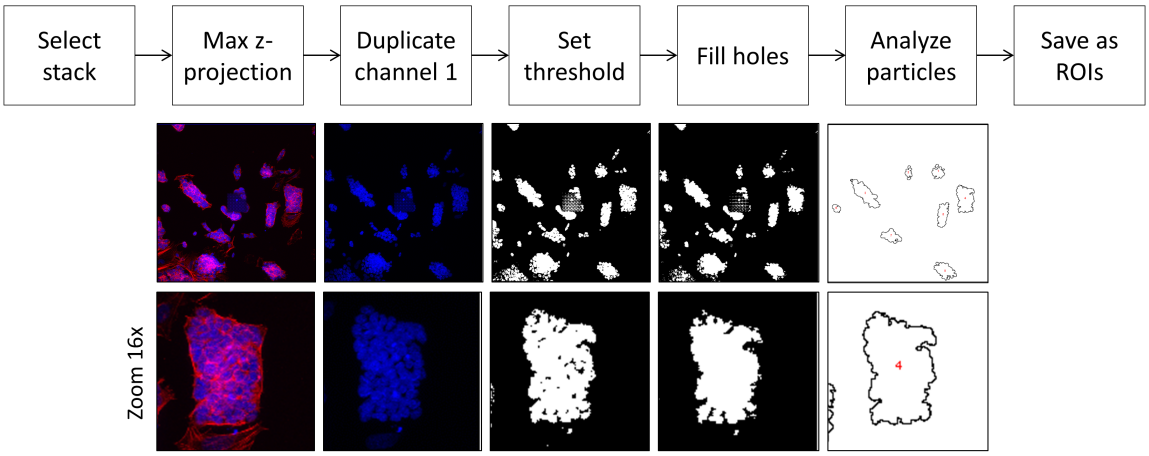

Figure 2.12: Block diagram of Fiji/ImageJ algorithm for analysis of ESC colonies on the substrate surface. For each stack colonies are found and their ROI is numbered and saved after which the area is measured.

Chapter 3

Results and Discussion

3.1 Development of the 2PP scaffold workflow for cell culture

3.1.1 Fabrication

In order to assess the cytocompatibility of the employed material, test pedestals of 140x140x50 µm were printed in an array. Several iterations of dose tests were carried out with this structure, with the goal of limiting the printing time of this relatively large structure while maintaining good quality. It was concluded that increasing the slicing and hatching distance to more than 0.4 µm resulted in detachment of the pedestals. An optimum was reached with a slicing distance of 0.4 µm, hatching distance of 0.3 µm, scan speed of 60 mm/s and laser power of 90% which resulted in a printing time of 12 minutes per pedestal (see appendix B).

Concerning the solid 2.5D structures that were used in the curvotaxis experiment the same settings were used except for the galvo acceleration which was increased from 1 to 10 V/ms^2 to decrease the printing time even more.

In order to find the correct printing parameters for the scaffolds, the results of Beatriz Costa [63] were consulted. Her design of a microcage with beam diameter 1 µm and gap diameter 9 µm and a base pedestal were used for initial dose testing. Since the best microcages were achieved at scan speed 10-15 mm/s and a laser power of 70-80% (35-40 mW), this became the base point for dose testing of our scaffolds.

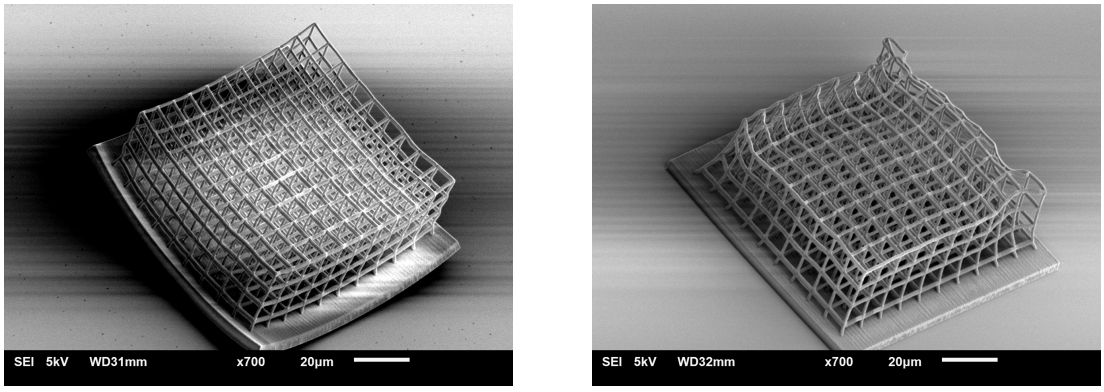

(a) (b)

Figure 3.1: 45 degree image of microcage (beam diameter 1 µm, gap size 9 µm) on pedestal. Laser power: 80%, Scan speed: 10 mm/s, slicing distance: 0.4 µm, hatching distance: 0.4 µm. a) Substrate plasma cleaned before printing. Pedestal is visibly curled up. b) Substrate spincoated with Ormoprime before printing. Pedestal lays flat on the substrate. Scalebar = 20 µm.

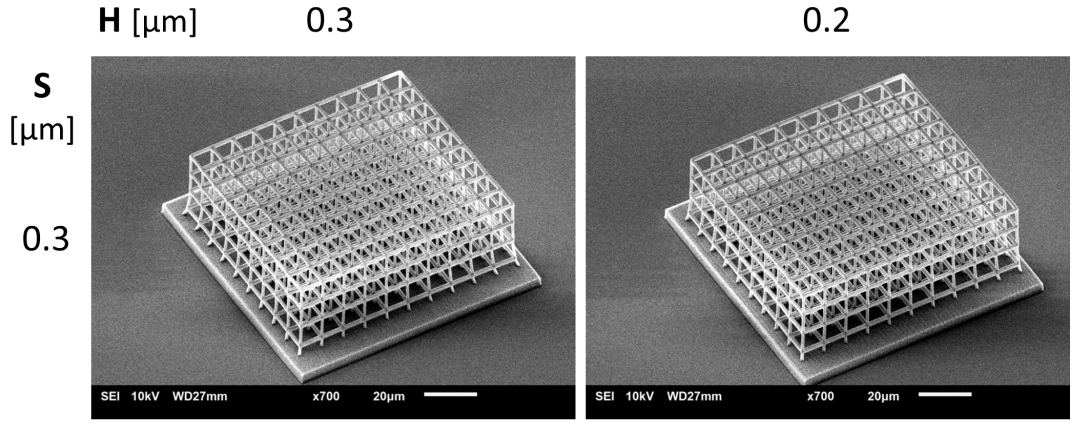

Figure 3.2: 45 degree image of microcage (beam diameter 1 µm, gap size 9 µm) on pedestal printed on substrate treated with Ormoprime. Laser power: 80%, Scan speed: 10 mm/s, slicing distance (S): 0.3 µm, hatching distance (H): 0.3 and 0.2 µm. Scalebar = 20 µm.

It was noticed that the base pedestal detached from the substrate in an upward curling motion. This is an undesirable effect, as this could cause the scaffold to detach from the substrate during cell culture. In order to counteract this effect, two methods of substrate preparation prior to printing were tried: plasma cleaning and spincoating with Ormoprime (see section 2.1 for a description of the exact steps). In figure 3.1 one can see the results for a scan speed of 10 mm/s and laser power of 80% (the full dose tests can be consulted in figures E.1 and E.2). While plasma cleaning did not seem to have an effect (figure 3.1A), Ormoprime promoted the adhesion of the structure to the substrate. However, the motion restrictions imposed on the scaffold by the now fixed base pedestal likely introduced some tension in the beams, resulting in a partial collapse of the structure (figure 3.1B).

It was found that decreasing the slicing and hatching distance increased the stability of the scaffold (see figure 3.2, full dose tests in figures E.3 and E.4). Furthermore, it was shown that a stable microcage could be printed on a substrate covered with Ormoprime without the need for a base pedestal (see figure 3.3).

It was therefore decided to print all the following scaffolds directly onto an Ormoprime covered substrate without the use of a base pedestal and with a slicing and hatching distance of 0.3 µm and 0.2 µm respectively. The combination of a scan speed of 10 mm/s and 80% laser power consistently achieved a satisfactory result for both the square and circular scaffolds of both pore sizes.

It was noticed during cell experiments that sometimes the big circular scaffold showed signs of instability, therefore another design was added in later experiments with a beam diameter of 2 µm instead of 1 µm (see appendix B for the print settings).

It should be noted that even with Ormoprime, some detachment took place during cell culture, staining, preservation, SEM preparation or confocal imaging in certain samples. The scaffold that detached often was the big square scaffold (BS), of which an average of 20% detached in cell experiments that were imaged with confocal microscopy. In these experiments none of the other scaffolds had detached. A proposed design alteration that could solve this problem is to add a base roster at the bottom of the scaffold, just as was used for the small square scaffold (see appendix A) to make the structure completely symmetrical. This would greatly enhance the contact area with the substrate and likely prevent detachment.

Detachment was more severe for the large solid 2.5D structures (e.g. sine wave, triangular lines, pyramids) of which around 50% was lost and unusable for analysis. The lost structures were included in the design table in appendix A for future reference and contain the rectangular lines, cylindrical lines and the dips and hills structure.

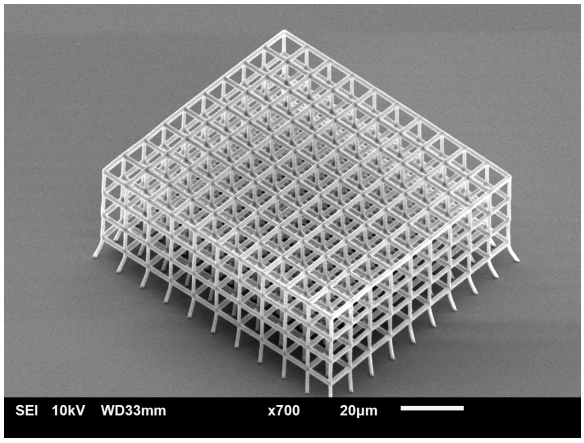

Figure 3.3: 45 degree image of microcage (beam diameter 1 µm, gap size 9 µm) printed directly onto substrate treated with Ormoprime. Laser power: 80%, Scan speed: 10 mm/s, slicing: 0.3 µm, hatching: 0.2 µm. Scalebar = 20 µm.

3.1.2 Press to seal

In the experiments that were conducted in this research, the press-to-seal silicone isolator was used during cell culture, fixation, staining or dehydration and imaging (see figure 2.4). This had many advantages but also some disadvantages (see table 3.1 for a summary).

It was shown that a successful cell culture could be grown inside the well created by a Press-to-Seal, for up to 4 days, if a container of liquid was placed with the substrates inside of the Petri dish in the incubator (see figure 2.4b). This measure was necessary to counteract evaporation of the cell medium. Since there was only 100 µL per well to begin with, a small amount of evaporation would already be detrimental to the cells.

Firstly, the press-to-seal greatly reduced the amount of cells and media that were needed for culture, fixation, staining and dehydration. Since the fused silica substrate was too large for a 6-well plate, the other option would have been to use a Petri dish which of course requires a much larger volume of media. With the seal, only 100 µL was needed each time. The advantage is that costs can be reduced, especially for more expensive cell types or media such as differentiation medium.

Furthermore, it was also possible to stain the cells with immunofluorescent dye inside the wells resulting in a good even staining through all the layers of the scaffold and on the surface. In the absence of the press-to-seal, a droplet with staining had to be deposited on top of the scaffolds which could flow away and did not cover the whole area. With regular 2D cell culture this is usually not a problem, but since we are working with 3D having a considerable height, it becomes important.

Additionally, the limited amount of media made it easier to handle the samples. Especially during elaborate fixation, washing and dehydration steps to prepare the sample for imaging, this was a great advantage. Since the volume that had to pipetted each time was so small, the process became a lot quicker and more efficient. Moreover, the substrates could be taped to a Petri dish, preventing any movement of the substrate inside the dish that could cause damage to the scaffolds. It was also easy to have a substrate that was dry except for the well created by the Press-to-Seal, which prevented the substrate from sticking to the Petri dish due to surface tension.

Lastly, a coverslip can be placed on top of the Press-to-Seal. It must be noted that the coverslip is not locked in place by the seal whenever there is liquid in between the two. Sadly, this is something that is evidently going to happen when you want to do confocal imaging because the well needs to be fully filled up with mounting medium to prevent air bubbles in the sample, thus when pressing a coverslip on top, some mounting medium will spill out. Even though the coverslip is not permanently fixed in place, experience shows that it will usually only move when a force is directly applied to it and not during confocal imaging for example. Therefore, the seal with a coverslip on top (see figure 2.6C), provides very convenient storage for an immunofluorescent stained sample of 3D scaffolds with cells. The very small contained volume prevents turbulence of the medium which

could cause damage to the sample, especially during transportation. Furthermore, evaporation is retained because the medium is closed off, thus the sample can be conserved for a long time. It is also a convenient configuration for imaging with confocal microscopy as shown in figure 2.6C.

Unfortunately, there were also some problems with the seal. First of all, the adhesive side did not stick to a wet surface. This means that either the seal should be used for the whole duration of the experiment, or not at all. It cannot be applied somewhere later in the experiment e.g. during staining. This also makes it impossible to change to a thinner spacer for imaging purposes. As mentioned before, the coverslip also does not stick to the seal if some liquid gets in between. This can form a problem if a shear force is accidentally applied to the coverslip or an inverted microscope is to be used. One solution would be to use glue, however it is difficult to prevent glue from entering the well when a coverslip is pressed on top.

The biggest disadvantage is that the seal was highly prone to detachment. In several experiments multiple seals detached from the substrate during cell culture or preparation for imaging, often severely destroying the sample. When the seal detached during culture, cell medium leaked away and cell death occurred. When the seal detached during preparation for imaging, it slipped and damaged the scaffolds and cells or the fixation process was disturbed and salt crystals remained. Interestingly, seal detachment did not occur during the first experiments with HeLa cells and ESCs on scaffolds but became a consistent problem during the experiments thereafter.

In conclusion, the aforementioned advantages of the Press-to-seal are overshadowed by the risk of detachment which may end up compromising an experiment that extends several days and includes expensive chemicals and cells. Therefore it should be examined what caused the detachment or if there is another brand of silicone isolators that works better, before one decides to make use of these isolators for cell culture. One could also think of alternative solutions such as cutting off corners of the fused silica substrate before printing so that it fits in a 6-well plate or printing the scaffolds on a coverslip or round substrate. The standard thickness for such a round substrate (compatible with the Nanoscribe) is 170 µm which could form an advantage if the sample is imaged with an inverted microscope, but the small thickness also means that they are quite fragile and thus need to be handled very carefully. However, both of these methods do not solve the problem of uneven staining (in the scaffolds).

Table 3.1: Advantages and disadvantages of Press-to-Seal use in experiments concerning cell culture in 3D scaffolds.

Advantages	**Disadvantages**
Easy handling	Coverslip does not stick to wet seal
Minimal amount of cells and media required	Seal does not stick to wet surface
Even immunofluorescent staining	Prone to detachment
Convenient storage of immunofluorescent sample	

3.1.3 Confocal imaging configurations

Inverted microscope (Vectashield seal)

As mentioned in section 3.1.2, the adhesion between the coverslip and press-to-seal was compromised when mounting medium got in between. This formed a risk of mounting medium getting on the objective when imaging with an inverted microscope. Using glue to attach the coverslip to the seal came with its own challenges. First, the glue had to be prevented from entering the well and

secondly, it was likely that air would be trapped in the well. Since such a bubble could compromise imaging, it had to be prevented that it was located above the scaffolds.

It is thus more convenient to use an upright microscope with these kind of 3D experiments. If only an inverted microscope is available, it would be advisable to look into printing on coverslips or using a glass bottom dish. If the structure is printed on a coverslip, it can be imaged from below while the sample stays upright. This also has the advantage of decreasing the needed working distance compared to the seal configuration. When using a glass bottom dish, the substrate could be inserted in it upside down while the bottom dish stays upright and can be imaged from below. However, for standard glass bottom dish sizes this does require the use of an objective with a relatively large working distance.

Upright microscope (Oil immersion)

Oil immersion (see figure 2.6D) is not a conventional method for imaging cells as an oil objective is normally used in combination with a coverslip. However, since the working distance of the oil objective was only 240 µm and thus could not bridge the seal depth, immersion was the only option to be able to use this higher magnification objective (40x, NA 1.25). Luckily the refractive index of type F immersion oil (RI=1.518, Leica Microsystems) is close to that of glass (RI=1.517, see table fig 2.3) and therefore this was possible to do without noticeably compromising image quality. The advantage of oil is that the refractive index is closer to the refractive index of IP-Dip than Vectashield is (see table 2.3) and thus may give a clearer view of the cells in the scaffolds.

In figure 3.5 one can see a comparison of images taken using the oil immersion configuration (figure 2.6D) with regular confocal and multiphoton versus images taken using the water dipping objective with Vectashield, a seal and coverslip (figure 2.6C). From this figure we can see the almost perfect reconstruction we could retrieve of the scaffold using oil immersion with the oil objective (40x, NA 1.25, WD 0.24 mm) versus the reconstruction when using Vectashield and a water dipping objective (20x, NA 1.0, WD 1.95 mm), which shows a more stretched cross-section view.

Another thing to notice is that if we compare the images at a height of around 25 µm in the scaffold (second row of images in figure 3.5), we can see that in the oil immersion cases the slices show (almost) no signal from layers of the scaffold underneath or above this slice. Meaning that the slices show an image that you would get if you section the 3D model in CAD software at that specific height. However, in the case of Vectashield plus seal, we do see signal from the surroundings. Instead of dots, we also see the circular pattern and instead of seeing just circles on top of the scaffold, we also see 'crosses' in between them.

If we compare using multiphoton versus regular confocal by looking at the images, they give almost the same result. However, if we look at the mean intensity per slice (see figure F.1) we do see two different patterns but since the lasers and their powers used are different in both stacks, it is hard to compare values. Appendix F elaborates further on the mean intensity.

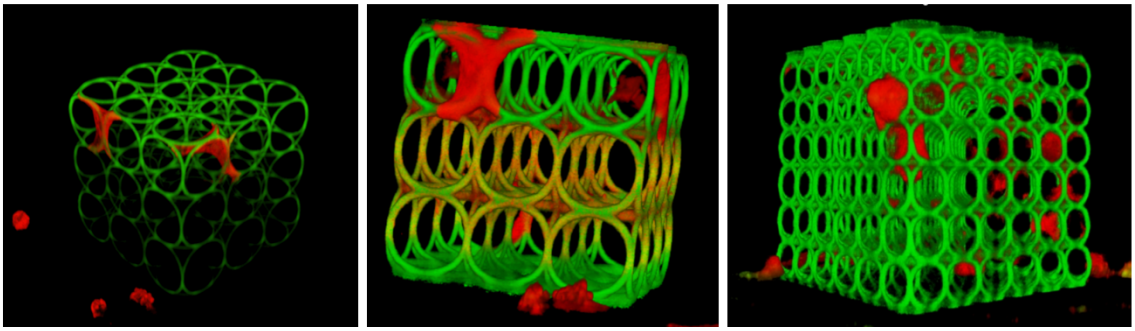

Figure 3.4: 3D reconstruction in Fiji (ImageJ) of scaffold with HeLa imaged in oil immersion configuration. HeLa stained for F-actin with phalloidin. 488 and 561 excitation laser. Stacks taken with 40x oil objective (NA 1.25, WD 0.24 mm) and Leica SP 5 Intravital confocal microscope.

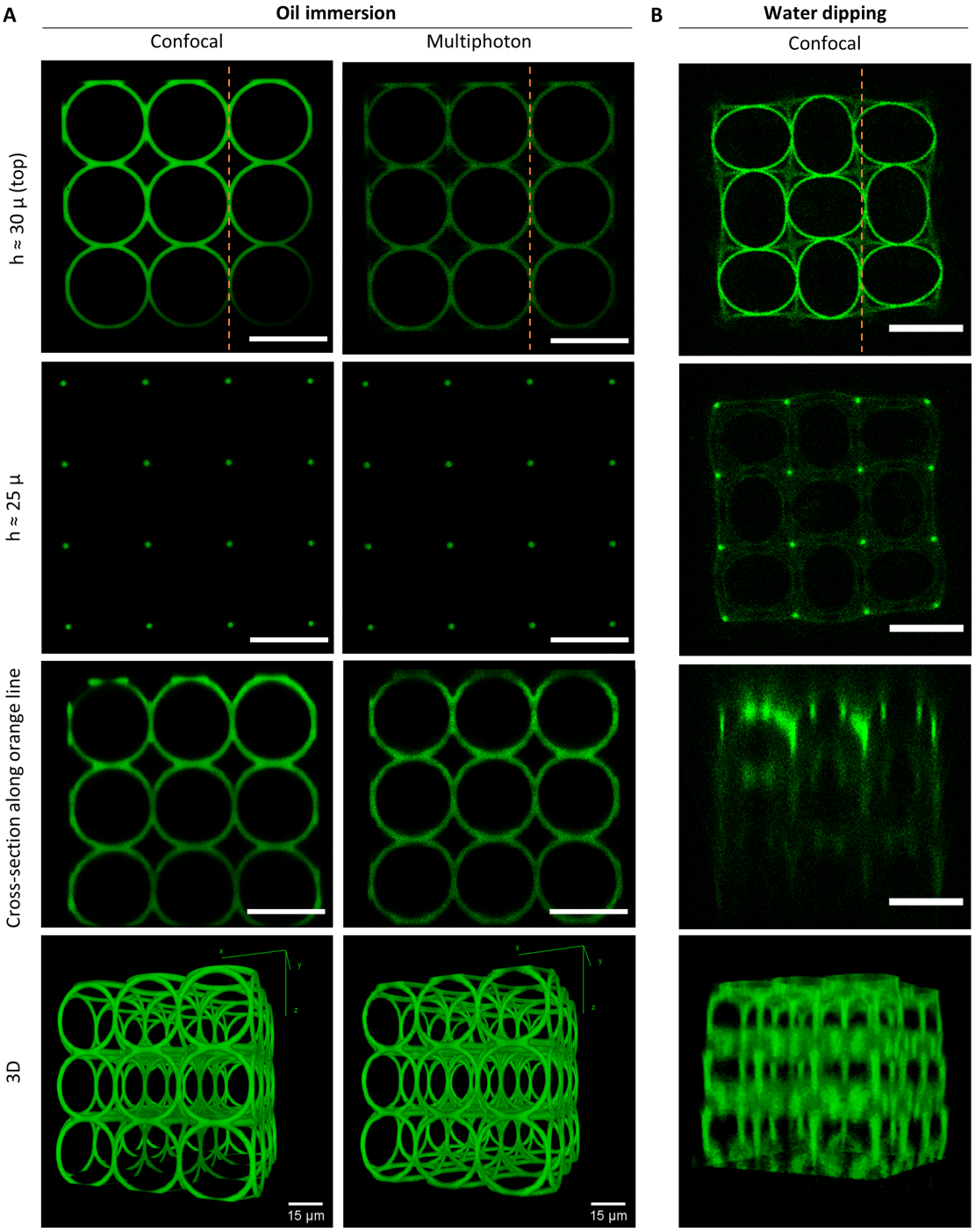

Figure 3.5: Comparison of stacks taken of a circular scaffold in different confocal imaging configurations. Top row shows the slice at the top of the scaffold (height h ≈ 30 µm). Second row is the image taken at h ≈ 25 µm. The third row shows the cross-section along the dashed orange line indicated in the images in the first row. The bottom row contains 3D reconstructions of the stacks made using Fiji (ImageJ), enhanced with macro by Gert-Jan Kremers. A) Oil immersion with 40x oil objective (NA 1.25, WD 0.24 mm), confocal versus multiphoton imaging of same circular scaffold (beam diameter 2 µm, pore diameter 30 µm). B) Water dipping imaging of circular scaffold (beam diameter 1 µm and pore diameter 30 µm). Sample was cultured with cells and conserved in Vectashield with a Press-to-Seal and coverslip. 20x water dipping objective (NA 1.0, WD 1.95 mm). Scalebar in top three rows = 30 µm. Scalebar bottom row = 15 µm. All images were taken with Leica SP 5 Intravital.

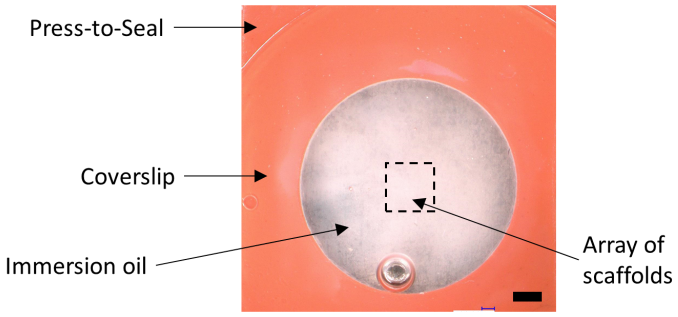

Figure 3.6: Immersion oil turned foggy after several hours of confocal imaging of HeLa cells cultured on scaffolds in well created by Press-to-Seal silicone isolator. Coverslip was not present during imaging but later applied for preservation purposes. Image taken with Keyence Digital Microscope VHX-6000. Scalebar: 1 mm.

After testing the imaging protocol with bare scaffolds, it was also tried with scaffolds that contained HeLa cells which were only stained for F-actin with phalloidin (see figure 3.4). However, after imaging for 2-3 hours the oil had turned foggy (see figure 3.6). This occurred even faster when trying to image scaffolds with HeLa stained for F-actin (phalloidin) and DNA (NucBlue). This indicates that a reaction takes place between the cells and the immersion oil, possibly from the lipid bilayer of the cell membrane breaking down.

To conclude, even though theoretically oil immersion is promising for imaging, it was shown to be incompatible with cells. However, it is a very good method when one wants to image bare scaffolds or other 3D structures.

Upright microscope (Vectashield immersion)

If we compare the method of Vectashield immersion with regular imaging (configurations B and C in figure 2.6) by looking at mean intensity graphs, we see that the mean intensity is much lower (see figure F.2) and also decreases much faster as we get deeper into the scaffold. We also cannot distinguish any peaks. From the stack images we see some barrel distortion taking place (see figure 3.7).

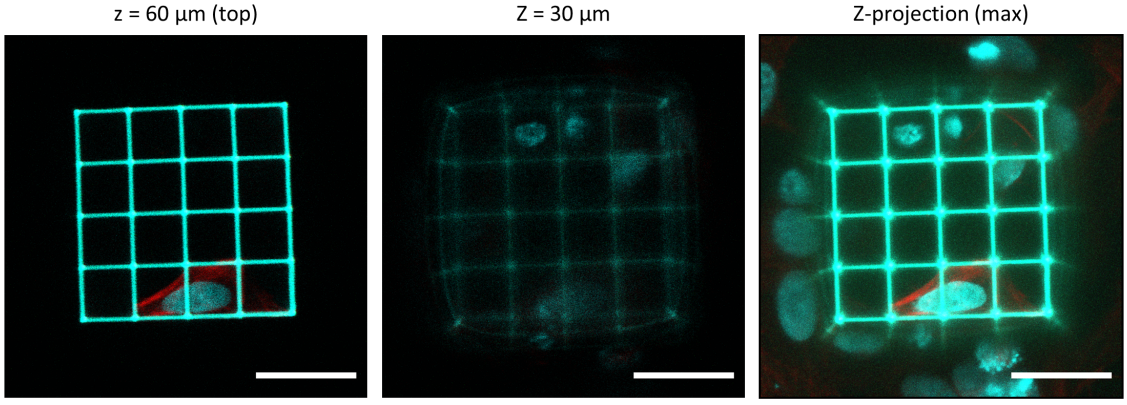

Figure 3.7: Vectashield immersion with 40x oil objective (NA 1.25). Blue = DNA (DAPI), red = F-actin (phalloidin). Small square scaffold with HeLa cells after 2 days of culture. Scalebar = 30 µm.

Upright microscope (Vectashield seal - Multiphoton)

When we compare the images taken with the water dipping objective of the sample with a Press-to-Seal, Vectashield and a coverslip (configuration C in figure 2.6) in both confocal and multiphoton

(MP) imaging configurations, we find that the latter one captures the structure slightly better, especially deeper into the scaffold (e.g. at h=20 µm the lines are clearer for MP and more grainy for confocal, see figure 3.8A). However, photobleaching (the loss of fluorescence of the fluophore due to light induced damage) occurred during imaging with MP, mostly for the red channel (see figure 3.8B). This caused some artefacts which are visible in the maximum z-projection. Because of this bleaching risk and the minimal gain in resolution, multiphoton imaging was not pursued further.

Upright microscope (Vectashield seal versus plastic sheet)

It is hard to compare the method B and C (see figure 2.6, press-to-seal versus plastic sheet) of confocal imaging because we imaged different experiments with these methods. Although the same cell type was used in these experiments (HeLa), there was some variety in scaffold type and the amount of cells located in the imaged scaffolds. Furthermore, settings such as laser power or gain were varied between the stacks. In Appendix F we compare the mean intensity per slice in the stack. From these graphs it is also clear that the geometry of the scaffold and pore size have an effect on the obtained image quality.

From our results, it does seem that there is a slight improvement in image quality when using the sheet which could be explained by the decreased working distance due to the sheet acting as a thinner spacer than the seal.

Even though the sheet might create a small increase in quality, it is a less robust method if a sample is to be stored for a longer period since the created well is not leak proof. When placing a coverslip over the well, this can also easily cause more pressure to the scaffolds since there is less mounting medium between the coverslip and the substrate with scaffolds when the spacer, in this case the sheet, is thinner (the thickness of a sheet is 180 µm and that of the seal is 900 µm). It is noteworthy that using a seal is preferred for even staining but after staining it could be carefully removed to be replaced by a sheet. However, the sheet can be used on a wet surface whereas the seal cannot.

Discussion

From the tested methods, Vectashield imaging with a water dipping lense is the best method with the thinner spacer increasing image quality slightly. The oil immersion works really well on bare scaffolds, but not in combination with cells. Multiphoton imaging also slightly improves the quality over confocal imaging, but it comes with an increased risk of bleaching the sample. Since the experiments with confocal configurations were carried out parallel to the cell experiments, you will see that both water dipping configurations (figure 2.6B and C) were used for imaging the cell experiments.

For better image quality, one could try to minimize the working distance even more by printing the scaffolds on a coverslip and imaging them from below with an inverted microscope or turning the sample upside down to image with an upright microscope. In the latter case one should watch out that no bubble formation or mounting medium leakage occur. Another solution for the inverted microscope would be to use a confocal dish. A downside of printing on a coverslip is that they are very fragile and thus require careful handling during all experiment steps.

One could also think of changing the imaging parameters. The current stacks were taken with a 700 Hz frequency. Lowering this frequency might increase the resolution, on the flip side this will also increase imaging time rapidly.

Lastly, one might also think of using a scaffold material that is not autofluorescent such as IP-Visio (Nanoscribe). This could possibly decrease diffraction effects. Alternatively, the autofluorescence of IP-Dip could be suppressed by for example Sudan black [64] [65].

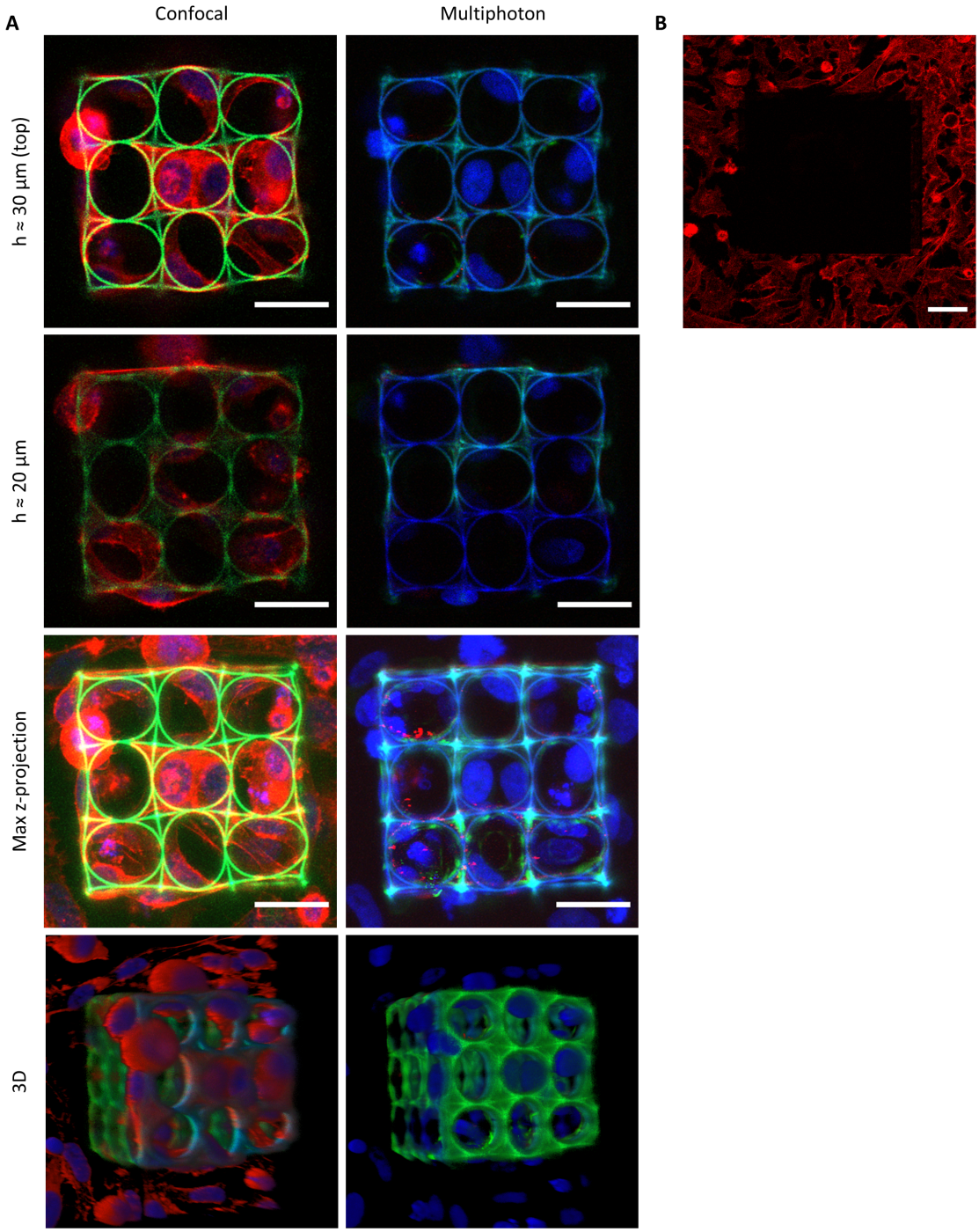

Figure 3.8: Confocal versus multiphoton imaging of big circular scaffold with HeLa cells after 2 days of culture. Images taken with 20x water dipping objective (NA 1.0, WD 1.95 mm), Leica SP 5 Intravital. A) Top row shows the slice at the top of the scaffold (height h ≈ 30 µm). Second row is the image taken at h ≈ 20 µm. The third row shows the maximum z-projection of the stacks. The bottom row contains 3D reconstructions of the stacks made using Fiji (ImageJ). Scalebar = 30 µm. B) Photobleaching occurred during multiphoton imaging. Scalebar = 50 µm.

3.1.4 SEM dehydration

Dehydration of the samples in order to image with SEM is known to cause shrinkage in cells which is undesirable if we want to know assess cell morphology or forces applied to the 3D structure. This can be especially important in our structures because a shrinking cell attached to the structure could deform the scaffold. SEM protocols to fixate and dehydrate cells vary a lot in literature concerning for instance fixation times from 10 minutes to 24 hours [66]. In the case of biological samples, a graded ethanol series is often followed by either air drying, chemical point drying (CPD) or HMDS treatment. HMDS is a chemical alternative to CPD, both methods aim to reduce the effects of surface tension during drying. In some cases HMDS was shown to reduce the amount of shrinkage of biological tissue [66] [67] [68] [69].

We explored the effect of HMDS, as well as the effect of using 2.5% GA or 4%PFA-1%GA, the length of fixation and the difference between ethanol in DIW versus ethanol in PBS on the scaffold deformation. The complete protocols are listed in table 2.4 and they are compared to protocol 1, the base protocol which was described in section 2.4.1.

Deformation was only present in 8% of the scaffolds that were imaged by confocal microscopy (5 substrates, 88 scaffolds in total), in four of these cases it concerned the big circular scaffold which was already known to be fairly unstable and in one case the small circular scaffold which also seemed to have detached from the substrate. In contrast, of 32 scaffolds (2 substrates) imaged with SEM, 91% had deformed. The 3 scaffolds that were still intact were of the SC type.

To the writer's knowledge, this observation has not been mentioned in any papers concerning 3D scaffolds for cells. The reason might that because the cells in this study are large in comparison with the scaffold beams (1-2 µm diameter versus cell nucleus of 20 µm diameter), the effects of deformation are very noticeable. Whereas, in the cases with scaffold beams that are relatively large compared to the cells, the effect of the cells on the scaffold might be minimal.

Since the deformation was not present during cell culture, it was checked if the fixation or dehydration process during SEM preparation directly affected the stability of the scaffolds. From figure 3.9 one can see that this was not the case. The hypothesis is that cells shrink during the SEM fixation/dehydration protocol and cells that are attached to the scaffolds therefore start to exert forces during drying, which in turn cause deformation.

Top view deformation

We compared the deformation of scaffolds on substrates prepared for SEM with seven different protocols (see table 2.4). Each substrate contained a 4x4 matrix of 4 different types of scaffolds

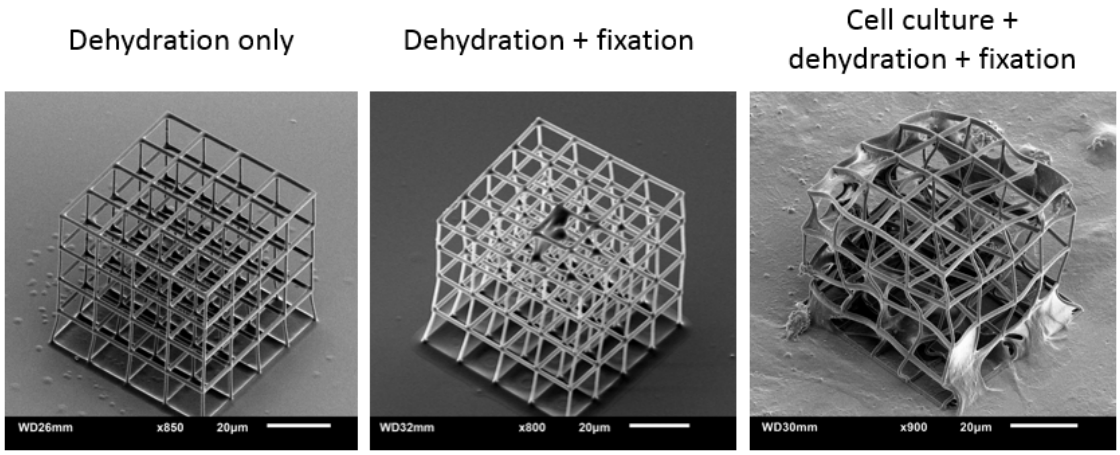

Figure 3.9: SEM images of small square scaffold after (a) sample dehydration, (b) sample fixation and dehydration and (c) after 2 days of HeLa cell culture followed by sample fixation and dehydration.

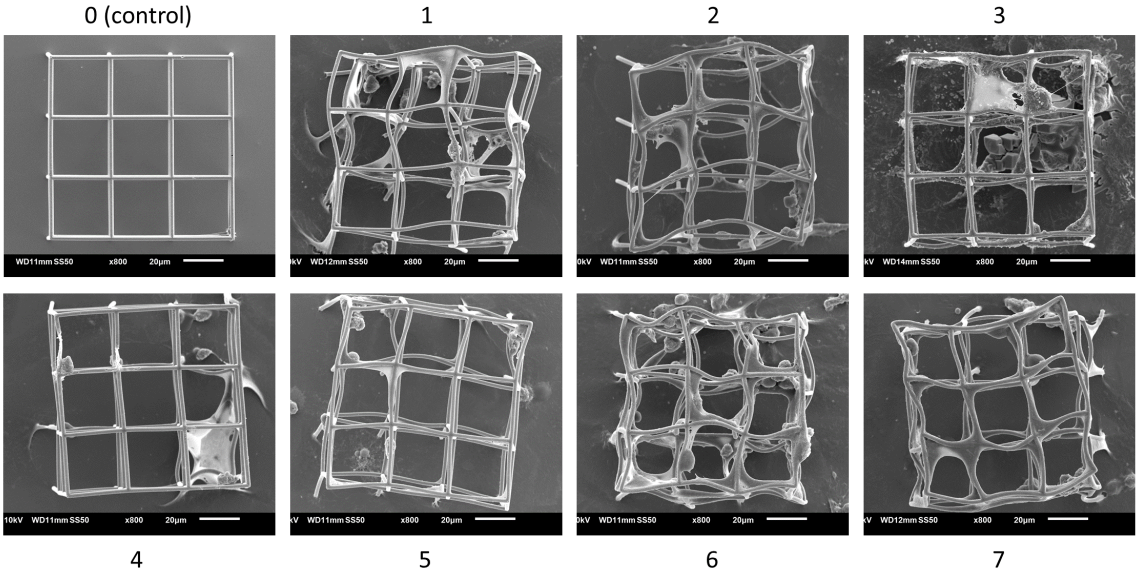

Figure 3.10: Top view SEM images of big square (BS) scaffold. HeLa cells were cultured for two days on the scaffolds after which the samples were prepared for SEM via different protocols 1-7 (see table 2.4). The control (0) did not undergo cell culture, fixation or dehydration. Scalebar = 20 µm

(thus 4 scaffolds of each type). On the substrate treated with protocol 2 one of the big circular scaffolds totally collapsed and was treated as an outlier as it most likely was a coincidence (possibly due to a fabrication defect). This scaffold was therefore excluded from the analysis. Figure 3.10 gives an overview of the SEM images taken of the big square scaffolds for each protocol (1-7) and a control (0) that had not undergone cell culture, fixation or dehydration.

From the data (see figure 3.11) of the deformation in the top view it becomes clear that the smaller scaffolds deform much less than the bigger ones. This means that these scaffolds are more stable structures. Therefore, to draw a conclusion, we focus on the deformation of the BS and BC scaffold since the differences between protocols are more significant here. In the following text, we will mention the average deformation of the BS and BC scaffolds combined.

Overall, in this experiment, protocol 4 scores the best with an average of 2% deformation and protocol 6 the worst with an average of 10% deformation. Thus the best protocol to use would be 2.5% GA for fixation for 10 minutes, followed by the regular dehydration series with ethanol in DIW. We will now further discuss the individual effects of certain elements.

It was shown in previous studies that HMDS reduced the shrinkage of cells. However, in our experiment this beneficial effect was only seen between protocol 6 and 7, for a fixation of 4 hours. In the two other two cases (protocol 1 versus 2 and protocol 4 versus 5) deformation increased with the use of HMDS (see figure 3.11). Overall, employing HMDS results in 1% more deformation versus letting the sample air dry. It could be that the HMDS procedure was carried out differently from that in literature. Moreover, the sample had to be transported from one lab to another while in 95% ethanol, which might have counteracted the advantage of HMDS.

If we compare the sample prepared with ethanol solutions in PBS instead of DIW, we see a decrease in deformation of around 1.5%. However, since the use of PBS introduces a lot of artefacts in the form of e.g. salt crystal formations (see protocol 3 in figure 3.10), it is not suitable for these kind of experiments.

Fixation in only 2.5% GA versus 1%GA-4%PFA, decreases the deformation significantly: around 50% (compare protocol 1 with 4 and 2 with 5 in figure 3.11).

Lastly, by comparing protocol 4 with 6 and 5 with 7, it is shown that a fixation time of 10 minutes is preferable over 4 hours in 2.5%GA, reducing the deformation with an average of 5% (see figure 3.11).

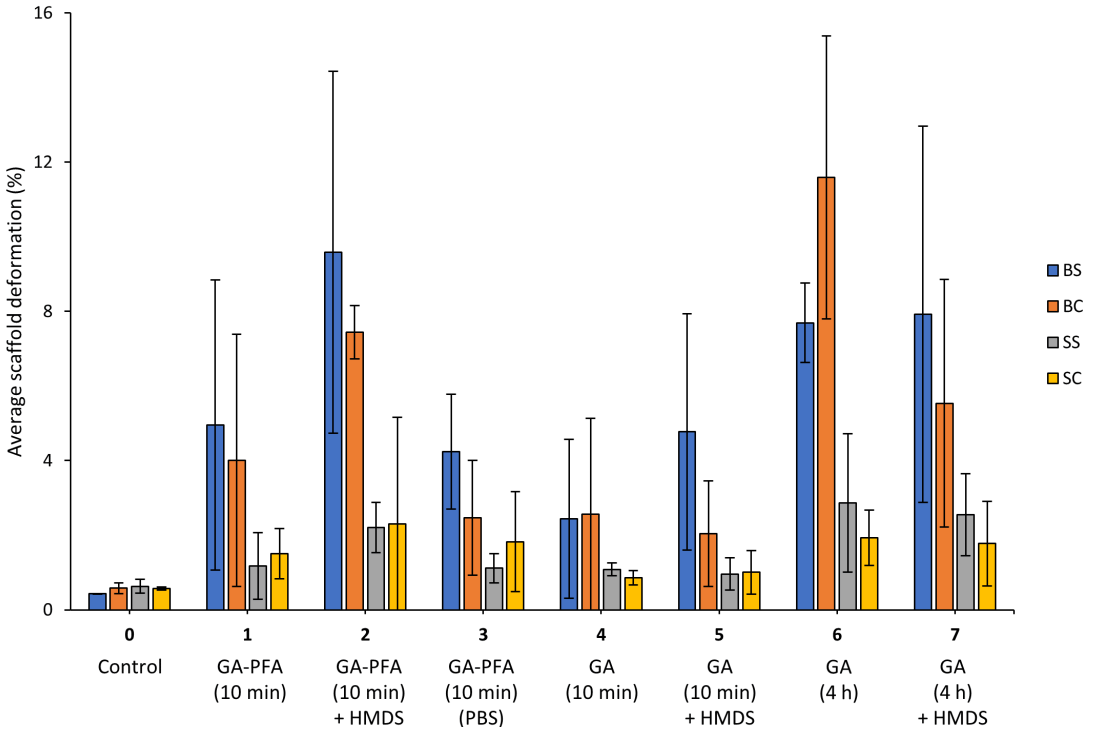

Figure 3.11: Average scaffold deformation (%) per scaffold type for sample preparation protocol 1-7 versus control (0).

Sideview deformation

Because of the order in which the scaffold types were arranged in the array, only two of the four big square scaffolds could be imaged from the side (see figure 3.12), thus the sample set was more limited. However, even when plotting the sideview distortion of these specific scaffolds versus their top view distortion (see figure G.1) there is a very weak correlation. Remarkably, the deformation of

Table 3.2: Average deformation of scaffolds in top view and side view of 3D IP-Dip scaffolds after 2 days of HeLa cell culture and preparation for SEM via protocol 1-7 versus a control (0). Protocol specifications can be found in table 2.4.

		Top (%)				Side (%)	
Protocol	**Description**	**BS**	**BC**	**SS**	**SC**	**BS**	**BC**
0	Control	0.4	0.6	0.6	0.6	0.3	1.2
1	GA-PFA (10 min)	5.0	4.0	1.2	1.5	6.2	9.2
2	GA-PFA (10 min)+HMDS	9.6	7.4	2.2	2.3	4.5	7.2
3	GA-PFA (10 min) (PBS)	4.2	2.5	1.1	1.8	3.5	5.7
4	GA (10 min)	2.4	2.6	1.1	0.9	2.7	3.1
5	GA (10 min)+HMDS	4.8	2.0	1.0	1.0	3.0	4.2
6	GA (4 h)	7.7	11.6	2.9	1.9	7.8	11.4
7	GA (4 h)+HMDS	7.9	5.5	2.6	1.8	4.1	10.0

the big circular scaffold in the sideview is less than 50% of that of the big square (see figure 3.13A). This could indicate that the circular scaffold is more stable (from the side) but it is hard to say since the measured points of distortion are of course defined differently in both scaffold types.

If we take a look at the big square scaffold, the largest discrepancies between sideview and top view deformation take place in protocol 2 and 7, both showing less deformation in the sideview (see figure 3.13B). However, the analysis of the sideview agrees with the conclusions found in the previous section. Protocol 4 still comes up as the best protocol with the least deformation whereas protocol 6 is still the worst.

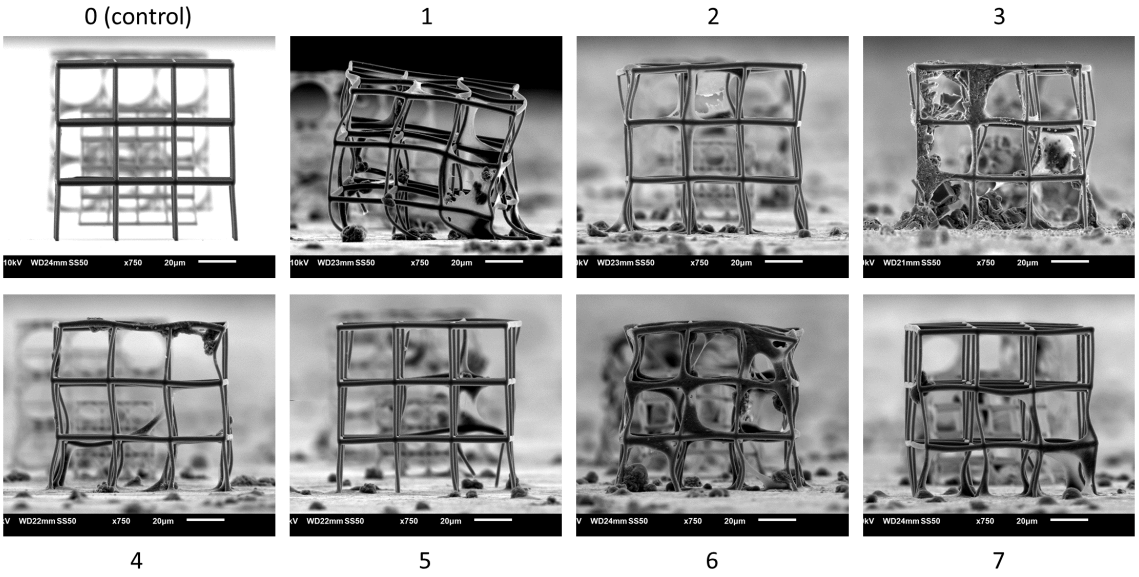

Figure 3.12: Sideview SEM images of big square scaffold. HeLa cells were cultured for two days on the scaffolds after which the samples were prepared for SEM via different protocols 1-7 (see table 2.4). The control (0) did not undergo cell culture, fixation or dehydration. Taken at 10 kV, magnification x750. Scalebar = 20 µm.

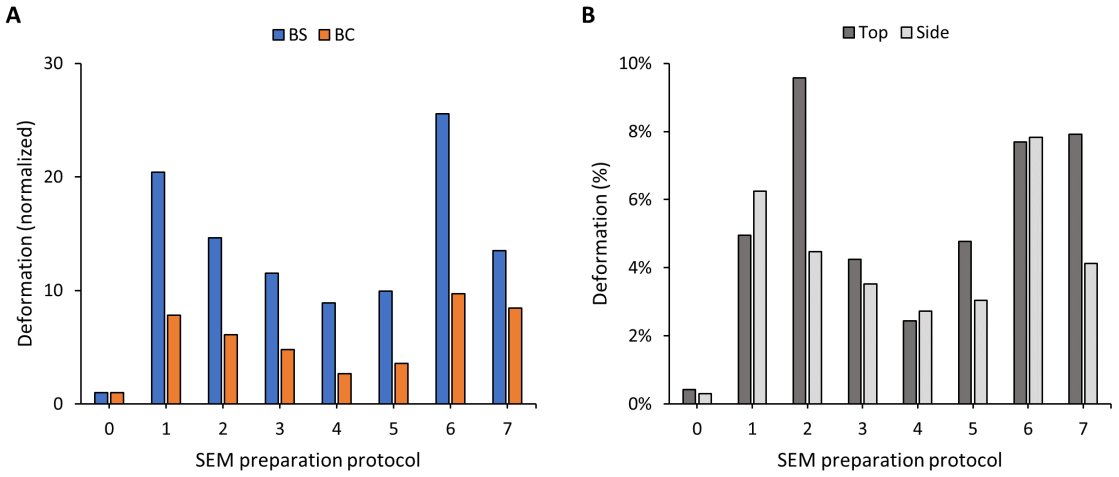

Figure 3.13: Deformation in BS and BC scaffold after two days of HeLa cell culture prepared for SEM via different protocols (see table 2.4) versus a control (0) that did not undergo cell culture, fixation or dehydration. A) Normalized deformation in sideview of big square scaffold (BS) and big circular scaffold (BC) per SEM preparation protocol. B) Comparison of deformation in the top and side view of the BS scaffold per SEM preparation protocol.

Discussion

Even though the experiment was carried out with the intention of keeping all sample conditions constant except for the SEM protocol, the validity of the results is somewhat questionable. This concern arises from the difference in cell confluency on each of the substrates that can be observed in the optical images (see appendix H). Since the same cell seeding density was used on each substrate, the variation in confluency might be due to the cell distribution during seeding or a difference in proliferation rate. In either case, since we know that cell shrinkage is responsible for deformation, a higher confluency will also result in more deformation. For example, the substrate that underwent protocol 4, which exhibited the least deformation, also looks like it has the lowest cell density.

Unfortunately, it was not possible to quantify the cell density from the optical images to correlate it with scaffold deformation thus we could not quantify how much it influenced the results. However, the effect of confluency should not be omitted in further experiments and could be decreased by increasing the sample size.

3.2 Effect of 2PP scaffolds on viability and morphology of HeLa cells

3.2.1 Cytocompatibility and seeding density

Initially, we tried to validate the biocompatibility of the IP-Dip structures and Press-to-Seal with HEK-293T (human embryonic kidney) cells. Unfortunately, none of the attempts resulted in a successful cell culture. It was thought that contamination due to insufficient sterilization of the structure and seal was at fault and therefore several different sterilization protocols were tried during these experiments (see appendix I). However, it is likely that another factor was at play such as the lack of biochemical coating or the cell seeding density. Instead of investigating further, we opted for a different cellular model, namely HeLa cells (human cervical cancer cells), since this part of the experiment was more concerned with the validation of cytocompatibility of the material rather than studying HEK-293T cells specifically.

With the sterilization protocol mentioned in section 2.2, HeLa were able to successfully grow on pedestals and scaffolds. In order to find a good cell seeding density for HeLa cell culture on the IP-Dip structures, we plated 16,000, 80,000 and 160,000 cells/cm^2 respectively (10,000, 50,000 and 100,000 cells per well). A plating density of 160,000 cells/cm^2 on IP-Dip pedestals resulted in sufficient cells covering the pedestals (see figure 3.14). Cells were viable and grew extensively on the pedestals (see figure 3.15). However, the coverage per density was heavily influenced by the cell seeding location (see figure J.1A-B).

Therefore we plated 80,000 and 120,000 HeLa cells/cm^2 on IP-Dip scaffolds and this time seeded them right on top of the structures (in the centre of the well) which gave a much better cell distribu-

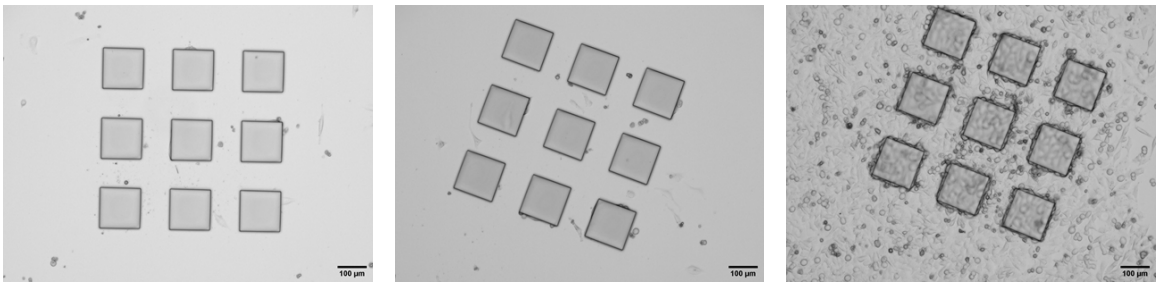

(a) (b) (c)

Figure 3.14: HeLa on IP-Dip pedestals after two days of cell culture, seeded with a) 16,000 cells/cm^2, b) 80,000 cells/cm^2 and c) 160,000 cells/cm^2. Scalebar = 100 µm.

tion (see figure J.1C-D). The results of this experiment are discussed in section 3.2. Both densities resulted in a sufficient coverage of the scaffolds for these experiments, but 120,000 cells/cm^2 had a slightly higher coverage.

For the SEM dehydration experiments and the substrate with scaffolds SSB and SCB we had to omit the Press-to-Seal and used a density of 25,000 cells/cm^2 Hela cells in a 10-cm Petri dish. This density worked well however, still not all scaffolds were covered as the local density still varied a lot.

By comparing confocal images of these experiments with the HeLa cells that were cultured on substrates with a Press-to-Seal, it seems that there is more cell death on the latter in both regions with a relatively high and low density which excludes the possibility that it is an effect of local cell density or confluency. However, it may be that the small culture volume of 100 µL causes more cell death or inhibits cell proliferation because even though the seeding density was significantly lower for the cells plated in the 10-cm dishes, the coverage was similar to the 120,000 cells/cm^2 sample. Furthermore, we cannot exclude that there is still a percentage of medium evaporating from the well during incubation.

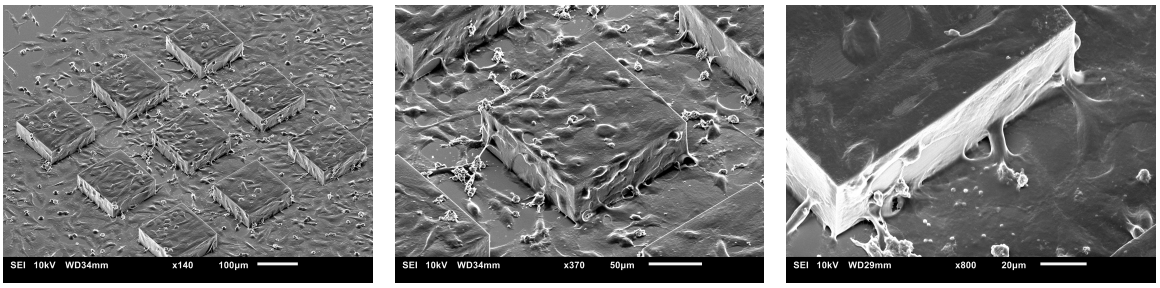

(a) (b) (c)

Figure 3.15: SEM images of HeLa on IP-Dip pedestals after two days of cell culture, seeded with 160,000 cells/cm^2. a) Scalebar = 100 µm. b) Scalebar = 50 µm. c) Scalebar = 20 µm.

3.2.2 Curvature 2.5D

For the analysis of HeLa cells on 2.5D structures, we focused on the nucleus since it is shown that it plays a role in curvotaxis. The first parameter that we measured is the the projected area of the nucleus since curvature or stiffness of the material could have an influence on the shape of the nucleus in 3D: e.g. more round or more flat. Furthermore, we wanted to investigate the aspect ratio (AR) and the alignment of the nucleus with certain structures which could indicate curvotaxis mechanisms. To find these parameters, first an ellipse is fitted to the nucleus in Fiji/ImageJ. The aspect ratio is then found by dividing the length of the major axis (or largest diameter) by the length of the minor axis (the smallest diameter which is perpendicular to the major axis). A perfectly round nucleus will have an AR of 1. The alignment of the cell is quantified by measuring the angle (θ) between the major axis of the ellipse and the x-axis (see figure 2.9), resulting in a value between 0 and 180 degrees.

3.2.2.1 Effect of pedestal thickness

In this experiment we compared cell nuclei on pedestals of 500x500 µm, featuring a height of respectively 25 and 50 µm, with cell nuclei on they underlying glass substrate (see figure 3.16).

Although the projected area distribution is spread wider for the 50 µm pedestal, the average projected area is the same as for 25 µm: 431 versus 430 µm^2 (figure 3.17A). On the other hand, the average projected area on the empty substrate is 396 µm^2, indicating that nuclei assume a more flat morphology on the fused silica than on a layer of IP-Dip which could be due to a difference in stiffness or topography. However, cells do not feel a difference between a thickness of 25 versus 50 µm.

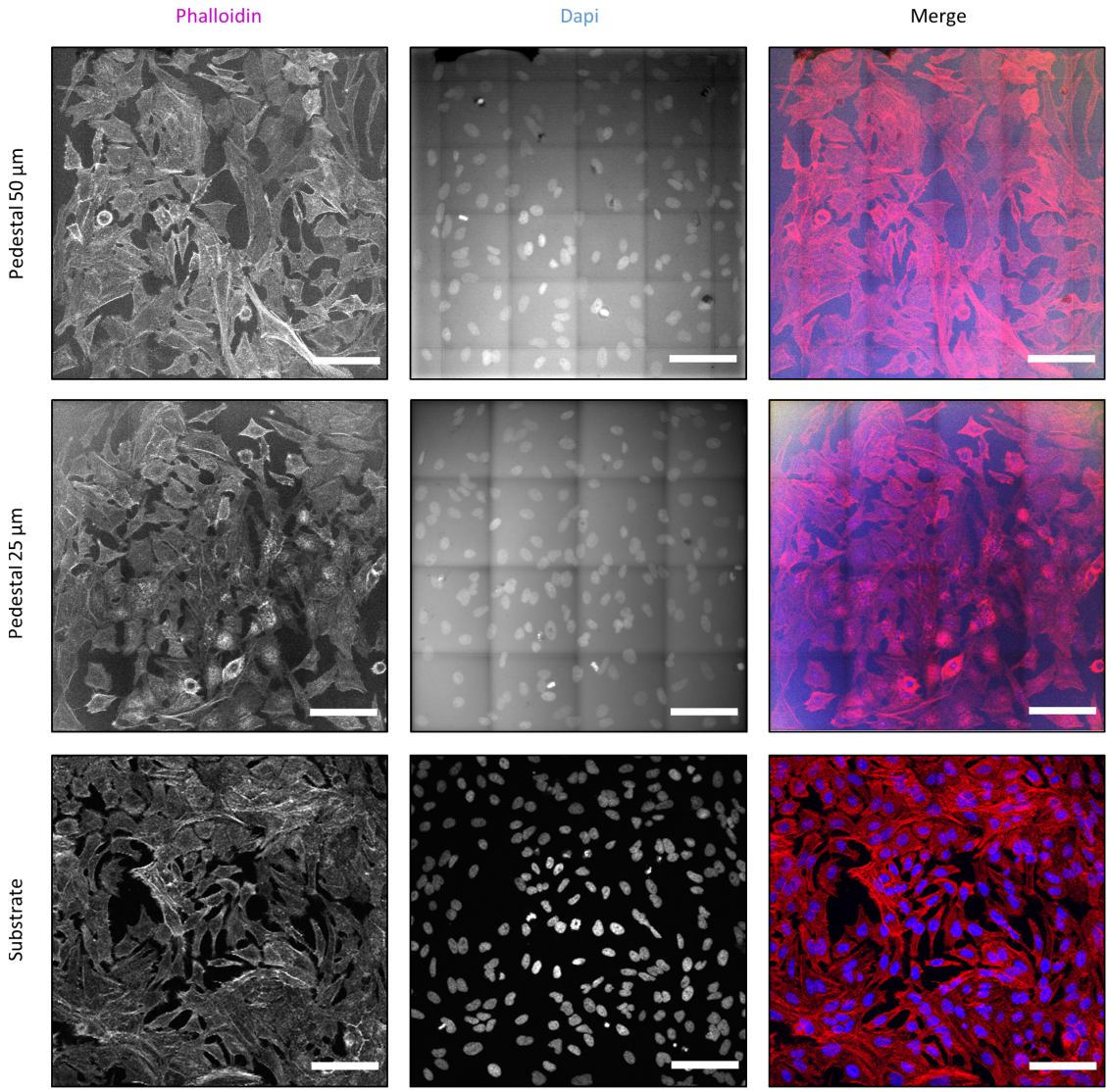

Figure 3.16: HeLa cells on 500x500 µm IP-Dip pedestals of 25 and 50 µm thickness versus on the substrate surface after 2 days of culture (seeding density 25,000 cells/cm^2). HeLa cells were stained for F-actin with phalloidin (red) and for DNA with DAPI (blue). Images taken with 20x water dipping objective (NA 1.0, WD 1.95 mm), Leica SP 5 Intravital. Scalebar = 100 µm.

The average aspect ratio is 1.7 for all cases (3.17B). There is a noticeable difference between the alignment of the nuclei on the IP-Dip pedestals versus on the bare substrate. The alignment looks random on the substrate (47% of angles between 45 and 135°, figure 3.17C and D) whereas on the pedestals the nuclei are in favor of aligning vertically: 65% and 60% of angles lie between 45 and 135° for the pedestals of 50 µm and 25 µm respectively. This alignment could be caused by the hatching direction during printing which was in line with the vertical axis. The slightly increased alignment for 50 µm versus 25 µm is likely insignificant.

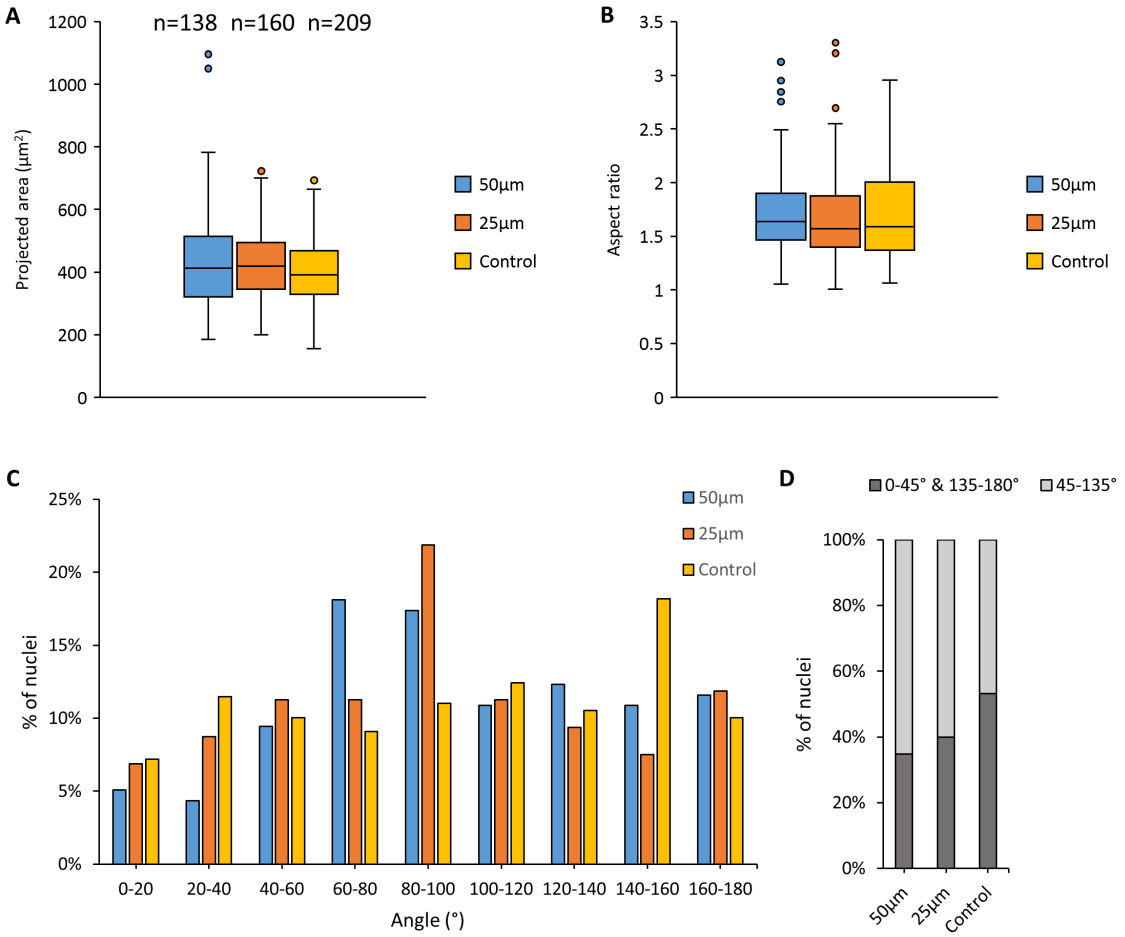

Figure 3.17: Analysis of HeLa nuclei on 500x500 µm pedestal of 25 and 50 µm thickness respectively versus on the substrate surface. A) Projected area of nuclei. B) Aspect ratio of the nuclei. C) Histogram of angle of major axis nuclei with horizontal axis per region. D) Distribution of nuclei with an angle between 0-45 & 135-180°and 45-135°.

3.2.2.2 Effect of sinusoidal structures

HeLa cells were cultured on a sinusoidal structure for 2 days after which the nuclei (n = 160) were analyzed (see figure 3.18A and B). Four regions were defined on the sinusoidal structure based on the height expressed in amplitude A: region I: $0 \leq h < -\frac{1}{2}A$, region II: $-\frac{1}{2}A \leq h < 0$, region III: $0 \leq h < \frac{1}{2}A$ and region IV: $\frac{1}{2}A \leq h < A$ (see figure 3.18C). In regions I and IV the curvature is relatively high compared to region II and III where the curvature is almost zero. Regions I and II are concave and regions III and IV are convex.

Since the regions are divided by height, the (projected) areas are not necessarily the same, depending on the exact dimensions of the sine. Of course the area is the same for regions I and IV, and both of the transitional regions also have the same area. For our dimensions (λ=100, A=25) the area ratio I/II and IV/III is 1.4, which we should keep in mind when looking at the distribution of cells.

We see that most cells (31% of the total) reside in region I, which is the most concave region, versus 22% in region IV (most convex region), which indicates that cells prefer the concave region (see figure 3.18D). However if we look at distribution overall, including regions II and III that have much lower curvature, the distribution between convex and concave is about 50/50 (figure 3.18E). Since the number of cells in region III is more than in region II, it could be that it is easier for

cells to migrate towards lower regions, whereas migrating towards higher regions costs more energy. This could result in cells being stranded on the upwards hill (region III) and not reaching the top of the hill (region IV), in contrast with regions I and II, where migrating to region II would cost more energy and thus cells reside more in the bottom of the grooves (region I). Another theory is that cells only start to feel the curvature in the top and bottom regions, where curvature is more prevalent, and therefore do not have a preference for either region II or III. However, when they reach higher curvature (near regions I and IV) they either react by entering the concave region I (thus leaving region II) or refrain from entering the convex region IV and rather stay in region III. It certainly would be interesting to explore this theory more in further research.

In comparison, Song et al. studied the migration behaviour of T lymphocytes (also called T cells, a type of white blood cell) on similar sinusoidal structures (A = 10 µm, λ = 20, 40, 80 and 160 µm) [70]. They found that most cells positioned themselves in the strongly concave region of the sine waves: for the sine structure with the same A/λ ratio as in our experiment this percentage was 53%, followed by 23% in the weakly concave region, 18% in the weakly convex region and 3% in the strongly convex region. If we compare this with the HeLa cells, their preference for concave surfaces, although present, is much less strong. This could simply be due to the cell type as for example macrophages were observed to not have any preference for a specific region in a hills and valleys array (surface could be described as the sum of two sinus waves that are mutually perpendicular) of A/λ ratio 10/100 [39]. Whereas the other cell types (Human and mouse MSCs and two types of fibroblasts) exhibited the same behaviour as T-cells: a high preference for strongly concave regions and then steadily decreasing percentages with the least amount of cells on the strongly convex region [39]. The preference was strongest in the MSCs.

Song et al. [70] and Pieuchot et al. [39] both found that you need a certain A/λ ratio for the cells to sense curvature differences. If the ratio is too small, it starts resembling a flat surface. Therefore it would be interesting to repeat the HeLa experiment with sinusoidal surfaces with a higher A/λ ratio to see if the preference effect gets stronger.

Because the analysis is carried out on a 2D projection whereas the actual cells are on a 3D structure, this has some consequences for the results.

The projected area of the nuclei is slightly smaller in regions II and III, which can be explained by the fact that projection had more influence on the area change in steep regions (figure 3.18F). Overall, the average projected nucleus area is smaller than what we found for the pedestals. It is not sure whether this discrepancy is solely because of the effect of the sinusoidal shape on the projection, or also directly due to the effect of the shape of the structure on cell/nucleus behaviour. At the 5% significance level we found that nuclei in region I had a significantly larger projected area than in regions II and III. There was no significant difference between regions I and IV and between regions II and III.

Interestingly, the nuclei on the sinusoidal structure show a strong alignment with the direction of the grooves, even more so in the regions II and III that have least curvature (see figure 3.18G and H). This could be because it costs more energy to migrate directly perpendicular to the waves (in the direction of the highest slope) versus along the wave, where the height stays constant. Since the highest and lowest regions of the sine are less steep, this effect might be less present here. The least alignment (72%) is seen in region I, which might be due to the shape that nuclei take on in a very concave region (more spherical, see [40]).

The alignment could have been increased by the hatching direction during printing (which is in line with the horizontal axis), since we also saw some alignment of nuclei on the large pedestal of IP-Dip (same hatching distance, see section 3.2.2.1) and it introduces some nano/microgrooves which we estimate to be in the order of a few hundred nm. It has been previously shown that the cell body of HeLa cells aligned up to 80% in grooves of 800 nm depth and 2 µm width [71]. However, in another research of Nagayama et al. HeLa cells were almost randomly oriented on a sinusoidal surface with 2 µm groove width and approximately 150 nm groove depth [72]. This could be explained by the fact that the percentage of aligned cells increases with increasing groove depth [71]. In any case, this illustrates the importance of groove geometry and since we do not know the

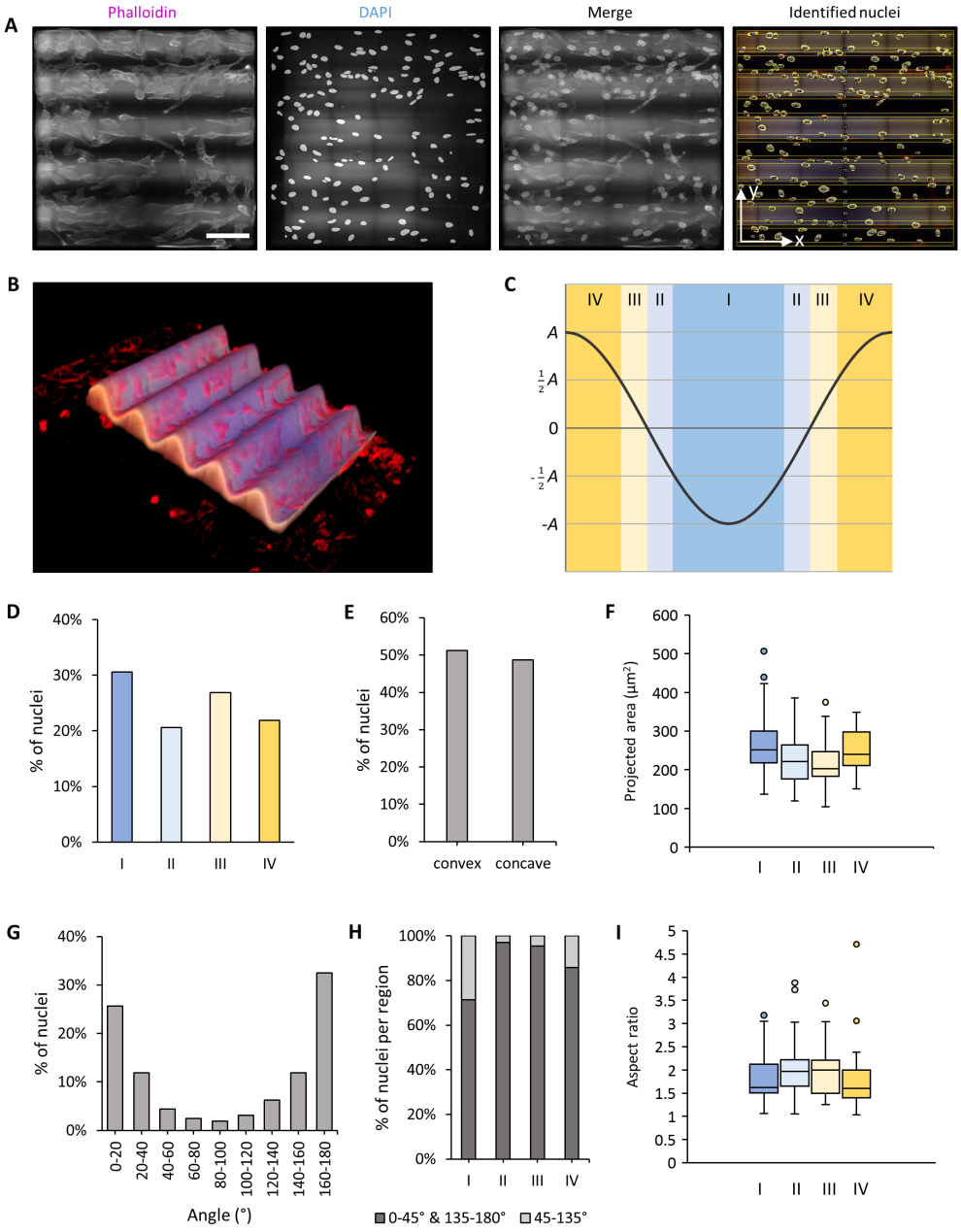

Figure 3.18: Analysis of HeLa cells on a sinusoidal structure with wavelength λ=100 and amplitude A=25. Analyzed nuclei: n = 160. A) Confocal images of sinusoidal structure with HeLa cells after two days of culture. Cells were stained for F-actin (phalloidin) and DNA (DAPI). Scalebar: 100 µm. B) 3D reconstruction of confocal images made in Fiji/ImageJ. C) Definition of regions on the sinusoidal structure based on the height h expressed in amplitude A: region I: $0 \leq h < -\frac{1}{2}A$, region II: $-\frac{1}{2}A \leq h < 0$, region III: $0 \leq h < \frac{1}{2}A$, region IV: $\frac{1}{2}A \leq h < A$. D) Distribution of nuclei per region. E) Distribution of nuclei located on convex versus concave regions. F) Projected nucleus area per region. G) Histogram of angle of major axis of nuclei with the horizontal axis. H) Distribution of nuclei with an angle between 0-45°& 135-180°and 45-135°per region. G) Aspect ratio of nuclei per region.

exact dimensions of the grooves caused by the hatching lines in our structure, it is not sure which hypothesis is more likely.

Still, the question remains: is this clear alignment that we see due to the shape and hatching direction of the structure or because of the effects of making a 2D projection? There are two ways in which the projection has an effect on the angle of the major axis with the horizontal one. The

first one is that the nuclei on the sinusoidal structure shrink in one direction when projected. This means, that if the major axis of the nucleus is not aligned with either the x or y-axis, then the major axis will rotate towards the horizontal one and the angle will become slightly less, in favour of the hypothesis of alignment. Secondly, if the ellipse is shrunk in one direction this could also mean that the initial major axis is no longer the major axis which again changes the angle that the major axis makes with the horizontal one.

In order to investigate the importance of these effects, we simulated the results that we would achieve if cells would be oriented in random directions and in random locations on the sinusoidal structure in MATLAB. We made some necessary simplifications: we assumed an ellipsoidal shape for the nuclei and only considered the sinusoidal slope at the centre of the nucleus, after which we applied the Monte Carlo method. It can be seen in Appendix K, that the simulated distribution of major axis angles is still significantly different from the distribution that we found in our experiments. Thus we conclude that indeed, the sinusoidal shaped structure aligned nuclei HeLa cells parallel with the grooves in the surface.

Alignment (and elongation) of cells parallel with the substrate grooves (not necessarily curved) is not an unfamiliar concept although it is usually measured over the whole cell body instead of focusing on the nucleus and most research was focused on micro grooves and topography instead of curvature on the cell scale. For example, microgrooves were found to align and elongate vascular smooth muscle cells (VSMCs, [72]) and HeLa cells [71]. In turn, curvature research has been mostly concerned with the difference between convex and concave surfaces on cell behaviour and not so much with alignment. Therefore our experiment with HeLa cells on a cell-scale sinusoidal structure is an interesting cross-over. In a paper by Zhang et al. PC12 cells and chick forebrain neurons (CFNs) were cultured on sinusoidal structures with A = 60 µm and λ = 350 and 180 nm [73]. They proposed a numerical model for the axonal outgrowth of the different cell types based on the Young's modulus and diameter of axons. It quite accurately predicted the behaviour of the different cell types. While PC12 cells consistently grew along the grooves, CFNs were found to grow across the ridges, again demonstrating the difference in behaviour between cell types.

The average aspect ratio (figure 3.18I) is slightly smaller in regions I and IV, indicating that nuclei are rounder there. If we compare these results with the large pedestals and the control on a bare substrate, it looks like the projected aspect ratio of the nuclei in regions I and IV coincides with the AR of nuclei on the large pedestals and control. The aspect ratio of nuclei on regions II and III is slightly higher. From our Monte Carlo simulation it followed that the observed average projected AR is slightly lower than the initial average AR.

As discussed in the overview paper by Baptista et al. [42] it is hard to isolate the effect of curvature during cell experiments. For example in the experiments above, we cannot say with certainty that the protein coating density or the roughness of the structures due to the nature of 2PP printing did not have an effect on the curvature sensing. In fact, the results indicate that the hatching direction might have played a role. Some further experiments would be needed to exclude these effects. Furthermore one can wonder whether gravity has an effect during seeding as due to gravity cells first mainly land and concentrate in the deepest part of the structure which results in a nonuniform cell distribution at the beginning of culture that could influence the results [42]. Pieuchot et al. did a test regarding sedimentation of cells due to gravity where they turned the substrate upside down halfway during cell culture and found that this did not have an effect on the results [39]. While this does indicate that gravity does not affect the migration of cells this does not exclude the influence of the initial cell distribution on the result. Another measurement did indicate a fairly uniform distribution after 2 hours of cell culture. In order to minimize the seeding effect it is important to determine a good duration for cell culture that is not too short.

Another important factor in curvature sensing of cells is the ligand density or ECM protein coating, as it has been shown this can influence the effect of curvature sensing [39] and cell alignment [71].

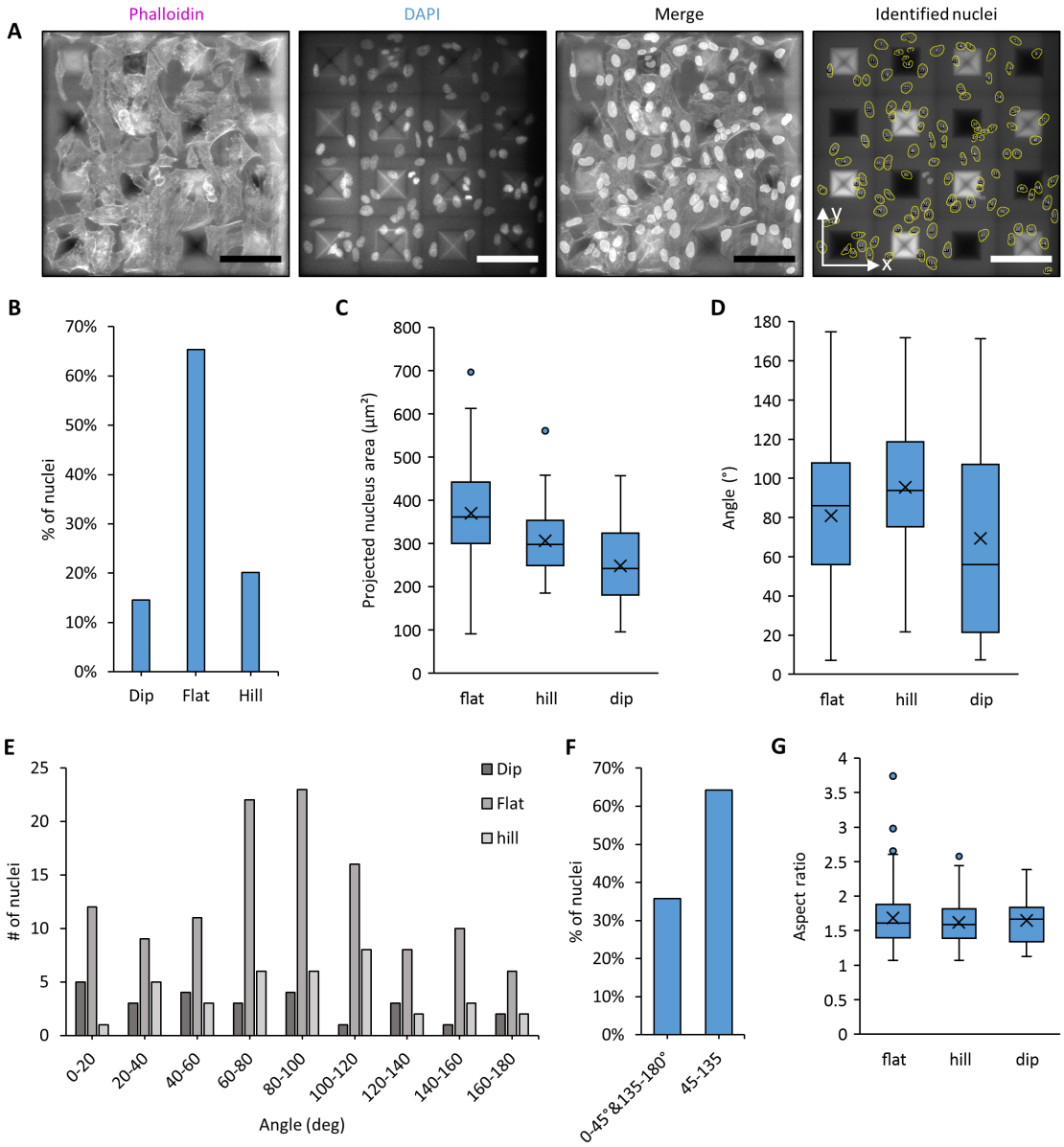

Figure 3.19: HeLa cells on pyramidal structure. Number of structures = 2 (same substrate). Analyzed nuclei: n = 179. A) Confocal images of pyramidal structure with HeLa cells after two days of culture. Cells were stained for F-actin (phalloidin) and DNA (DAPI). Scalebar: 100 µm. B) Distribution of nuclei on the different regions of the pyramid: the pyramid shaped dips, hills and the flat or horizontal region. C) Projected nucleus area per region. D) Angle of major axis nuclei with horizontal axis per region. E) Histogram of nuclei angles per region. F) Distribution of nuclei with an angle between 0-45 & 135-180°and 45-135°. G) Aspect ratio of nuclei per region.

3.2.2.3 Effect of pyramidal structures

There were two pyramidal structures on the same substrate. Their dimensions can be found in appendix A.

In total 179 nuclei were counted on the two pyramidal structures which were on the same substrate (see figure 3.19A). The majority of these nuclei, namely 65%, are located on the flat region of the structure (figure 3.19B) which takes up the largest part of the area. 15% of the nuclei were found in the pyramidal dips and 30% on a pyramidal hill. Thus, there seems to be a slight preference for

locating on the hills over the dips.

The projected area of a nucleus on the flat region is on average 370 µm^2 (3.19C). Since we look at the projected area, it makes sense that it is smaller on the dips and the hills. Interestingly, the area in the dips (249 µm^2) is on average 50 µm^2 smaller than the area of nuclei on the hills (306 µm^2).

From figures 3.19D-F we can see that there is a preference for aligning the nuclei parallel to the y-axis (as defined in figure 3.19) versus more parallel to the x-axis, namely 64% versus 36% respectively, which might be due to the hatching direction which was in line with the y-axis.

There is no significant difference in aspect ratio between the regions, the average aspect ratio being 1.67 (see figure 3.19G).

In conclusion, there is a slight preference for cells locating on the hills versus dips and for the the nuclei to align with the y-axis (as defined in figure 3.19A). The projected area of nuclei in the dips is significantly lower than the area on the hills which indicates a different 3D shape of the nucleus.

3.2.2.4 Effect of triangular structures

There were only 35 cells that grew on the triangular structure (see figure 3.20A-D) which was not enough for a statistical analysis.

In figure 3.20B, some cells were highlighted. It is clear that there is a wide variety in shape. In (1) we see cell that has a triangular shape, with the top side aligned with the ridge of the hill. Next to it we see a totally different cell that shows protrusions as if it is feeling around the hills and dips. In (2) we see a cell body that is aligned along the trench. Lastly, one very elongated and thin cell (bipolar) is spotted that is aligned parallel to the trenches on the horizontal part of the structure (3). The alignment of cell bodies that we see in the confocal images and the alignment of the nuclei (figure 3.20G-H), might be more prevalent because most cells were located near the edge between the horizontal parts of the structure and the hills. As previously mentioned, it could also have been promoted by the direction of the hatching lines.

Most cells were present on the flat area of the structure and just a few cells were located in a trench (figure 3.20E). The area of the nuclei has a very wide distribution in the dips. The average area is smallest for the hills (figure 3.20F). Furthermore, the aspect ratio is on average highest on the hills and lowest on the flat region (figure 3.20I).

Unfortunately, some structures that were intended to be used for curvature analysis, detached from the substrate before they could be imaged. Therefore we could not compare the curved structures with their straight counterparts as was initially planned. The aforementioned structures are included in Appendices A and B for future reference.

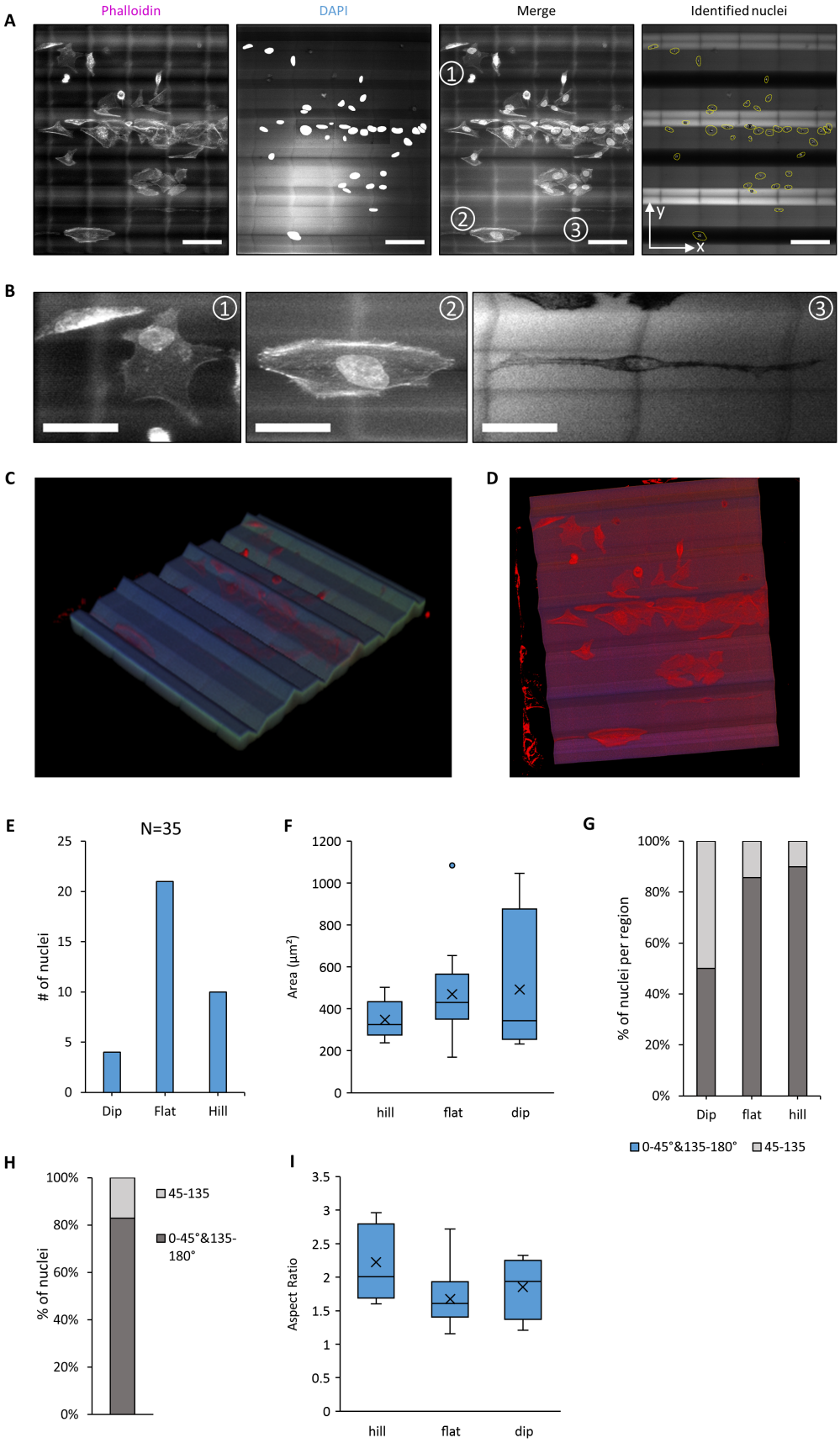

Figure 3.20: HeLa cells on a structure with triangular trenches (dips) and hills and analysis of the nuclei (N=35). A) Top view of confocal images. Cells stained for F-actin (phalloidin) and DNA (DAPI). Identified nuclei were analyzed. Scalebar: 100 µm. B) Closeup of several cells indicated in figure 3.20A. Scalebar: 50 µm. Isometric (C) and top (D) view of 3D reconstruction of the triangular structure, made with Fiji/ImageJ 3D viewer plugin. E) Distribution of nuclei on the different regions of the triangular structure: the dips, hills and flat region. F) Projected area of nuclei in respective regions. G) Distribution of nuclei with an angle between 0-45° & 135-180° and 45-135° with the horizontal axis per region. H) Distribution of nuclei with an angle between 0-45° & 135-180° and 45-135° with the horizontal axis. I) Aspect ratio of nuclei per region.

3.2.3 Culture of HeLa cells on 3D scaffolds

In order to look at the effect of 2PP scaffolds on HeLa cells, cell culture was performed on four samples with an array of 4x4 scaffolds including four different types of scaffolds of two different pore sizes: big square (30 µm pore size), big circle (29 µm pore size), small square (15 µm pore size) and a small circular scaffold (14 µm pore size). Two samples were imaged with confocal microscopy and the other two with scanning electron microscopy. In each of these duos two different cell seeding densities were used, namely 120,000 cells/cm^2 and 160,000 cells/cm^2. The substrate with seeding density of 160,000 cells/cm^2 was imaged with a Nikon Eclipse Ti inverted microscope at TU Delft (see figure 3.21A), while the substrate with 120,000 cells/cm^2 was imaged with a Leica SP5 Intravital at Erasmus MC (see figure 3.22). In the sample with the higher seeding density, two of the BS scaffolds

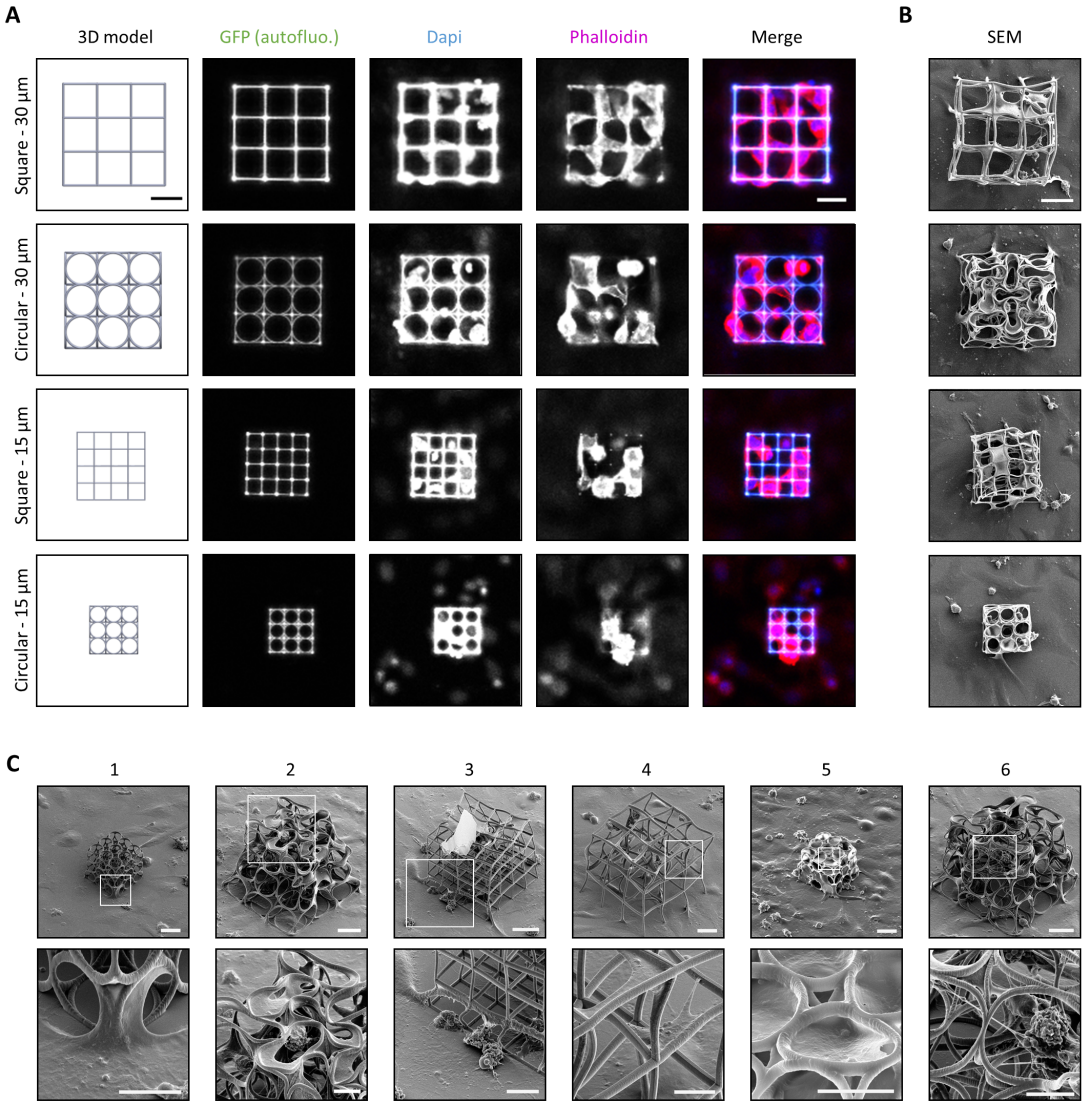

Figure 3.21: IP-Dip scaffolds (type BS, BC, SS and SC) seeded with 160,000 HeLa cells/cm^2 after 2 days of culture. A) Top view of scaffolds imaged with 20x dry lense (Nikon, TU Delft). Cells stained for F-actin with phalloidin (red) and for DNA with DAPI (blue). Scaffold is also fluorescent in green. Scalebar = 30 µm. B) Top view of scaffolds imaged with SEM. Scalebar = 30 µm. C) SEM images of scaffolds with HeLa cells at 45° tilt. Top row, scalebar: 20 µm. Bottom row are closeups of top row, scalebar: 10 µm.

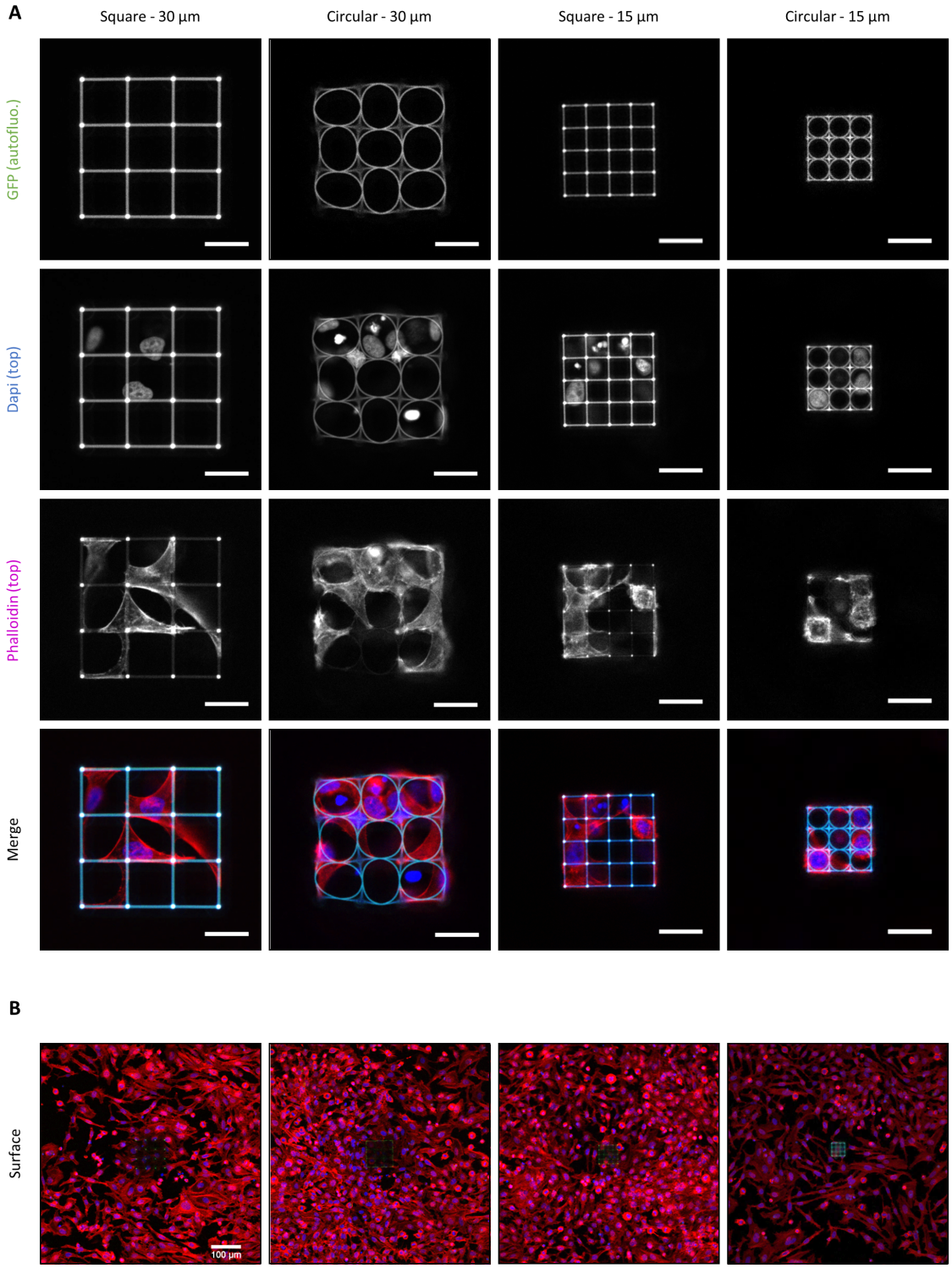

Figure 3.22: Confocal images of HeLa cells colonizing the 3D scaffolds: cell seeding density of 120,000 HeLa cells/cm^2. Grown on scaffolds for two days. 4 scaffolds types: BS, BC, SS and SC. Imaged with 20x water dipping lense (Leica, Erasmus). A) Top view of scaffolds. Scalebar: 30 µm. B) Wideview of substrate surface around scaffolds. Scalebar: 100 µm. Cells stained for F-actin (phalloidin, red) and DNA (DAPI, blue). Scaffolds were also fluorescent in the green channel.

detached and thus any analysis regarding this scaffold in the confocal images is based on a sample group of 2 units.

3.2.3.1 Cell morphology

In the SEM images of the 3D scaffolds seeded with a density of 120,000 HeLa cells/cm^2 (see figure 3.21B-C) we saw some interesting cell structures. Unfortunately, because of the dehydration effect described in section 3.1.4 we cannot be sure that these structures looked the same while the cells were in culture. Nonetheless, we found them noteworthy.

The most noticeable feature is shown in 3.21C1, where it looks like the cell follows the curvature of the scaffold, resulting in a shape that is like a sheep's horn. Interestingly the cell decided not to follow the circle completely, but extend a bit outward of the scaffold. This is different from what we see in 3.21C2, where the cell remains within the plane of the circle and forms a sort of half moon shape. In figure 3.21C3 we see a cell (or a connection of cells) that runs all across the horizontal beam of this square scaffold and continues further on the substrate on both sides. In 3.21C4 we see another characteristic of big square scaffolds where the cell occupies a corner, and in some cases forms a bridge to another beam of the structure. In presence of the small circular scaffold, we do not see the same half moon shapes as for the large circular scaffold, but the pores are often filled totally and the cell matter looks like a thin film that spans across the circle (see 3.21C5). Lastly, in 3.21C6, we see protrusions extending from a cell within the scaffold. The spherical shape and irregularly, bumpy surface of the cell indicate the process of cell death (apoptosis) [74] [75]. This was also observed in some of the other scaffolds. It would be really interesting to see if cell dehydration and deformation effects could be minimized to assess if these phenomena are still observed in SEM images or if they were only a result of dehydration.

In one of the big square scaffolds some strings of material were present that were only fluorescent in the blue channel (see figure 3.23A). Since the scaffold is intact, it is unlikely that this material is IP-Dip, especially because we would expect it to be fluorescent in the green channel too.

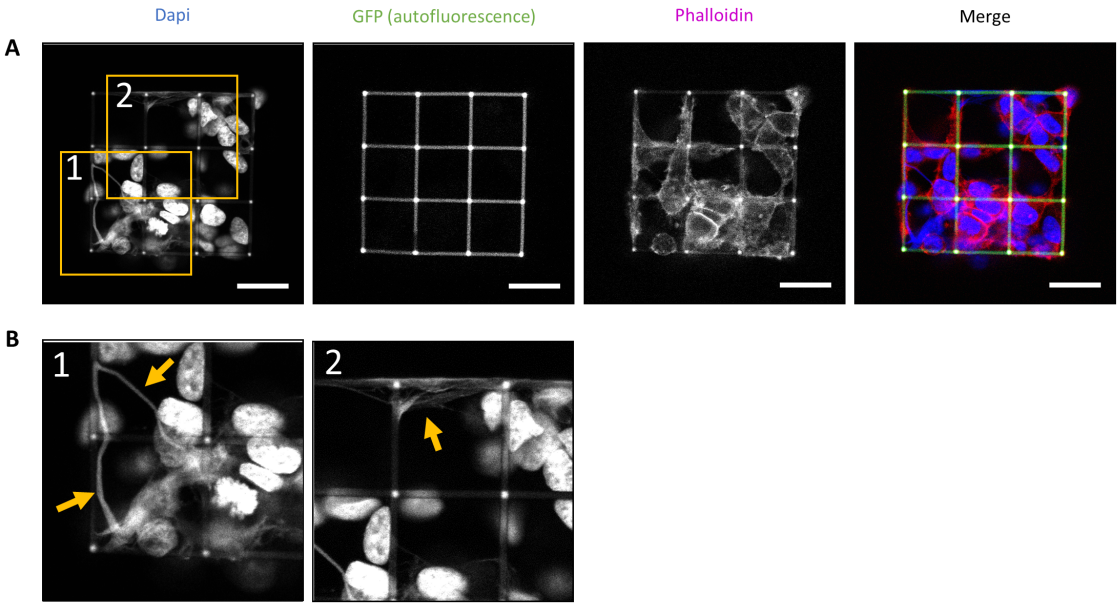

Figure 3.23: HeLa cells in BS scaffold, seeded with 25,000 cells/cm^2. Imaged with 20x water dipping lense (Leica, Erasmus). Stained for F-actin with phalloidin and for DNA with DAPI. A) Dapi "strings" visible that do not seem to be from the scaffold, as they are not fluorescent in the other channels. Scalebar: 30 µm. B) Closeups of regions indicated in A. Yellow arrows indicate DAPI "strings".

3.2.3.2 Nucleus size

Nuclei take on a different shape inside of the scaffolds versus on the substrate around the scaffold, where they have a much larger projected area (see figure 3.24B). On average, the projected area of nuclei in BS scaffolds seeded with 120,000 HeLa cells/cm^2 was 146 µm^2 whereas the projected area of the nuclei on the substrate around the scaffolds was 236 µm^2. This illustrates that the nuclei indeed react differently in a 3D surrounding and likely take on a more rounded morphology versus a flatter one on the substrate.

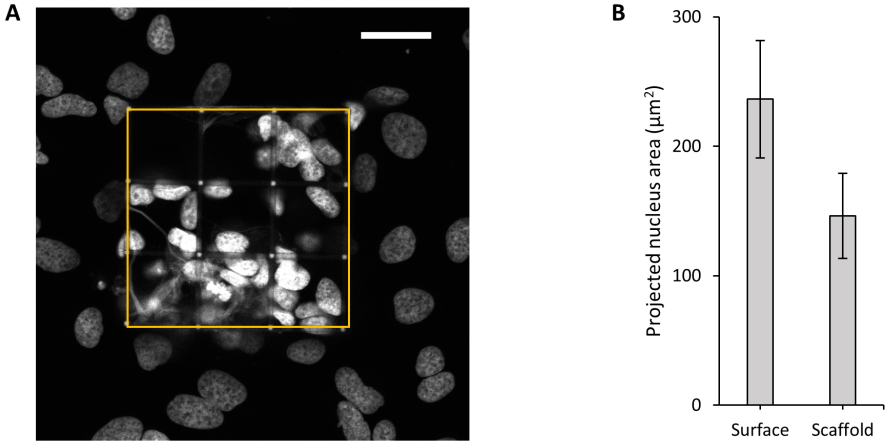

Figure 3.24: Comparison of nuclei in BS scaffolds versus on the substrate surface. A) HeLa in BS scaffold after two days of cell culture, seeded with 25,000 cells/cm^2. Blue channel, stained for DNA with DAPI. Image manipulated to show the difference in projected nucleus area/size outside and inside the scaffold. Suggesting a rounder shape inside the scaffold/flatter outside. Yellow indicates border of the scaffold. Scalebar: 30 µm. B) The projected area of nuclei in BS scaffolds seeded with 120,000 HeLa cells/cm^2 (n=33) and nuclei on the surrounding substrate surface (n=23) was obtained.

3.2.3.3 Nucleus localization within 3D scaffolds

In each scaffold type, we observed from the confocal images that most nuclei seem to be attached to a beam of the structure and rarely position themselves in the middle of a pore. It is suspected that the latter would cause more strain in the cytoskeleton. It would be interesting to test this hypothesis by examining the differences in strain of cells positioned with their nucleus in these respective positions.

In the case of the big square scaffold, we saw an even more noticeable trend where the cells were often positioned with their nuclei in corners or nodes (where two beams cross each other) and their cytoskeleton expanded towards other (nearby) nodes, resulting in a lot of triangular shapes. This can be seen in figure 3.21 as well as 3.22 and figure 3.25.

In figure 3.26 we see that this trend of nuclei centralizing around nodes can be observed in every layer of the scaffold. For the four BS scaffolds on the substrate seeded with 120,000 cells/cm^2, the location of cell nuclei were manually counted and analysed. On average, around 55% of the nuclei within the big square scaffolds can be found next to a node (94 nuclei were counted in total, divided over 4 scaffolds).

Furthermore, most cells are found in the lowest part of the BS scaffold (see figure 3.27), which is not surprising because here they can easily grow on the substrate without having to migrate upwards. Interestingly, more cells can be found in the top part of the scaffold versus in the middle part. For the BC scaffold, we also found most cells in the lowest part of the scaffold, but the number of cells in the middle and top part are equally distributed. Please note that the standard deviation is also a lot larger for the BC and overall, this scaffold was also colonized less than the BS.

Similar cell distributions as for the BS scaffold were also found in 120 µm high microtowers seeded with neural cells (Turunen et al. [53]) and a 300 µm high woodpile structures seeded with neural cells (Accardo et al. [56]). Accardo et al. hypothesized that cells could migrate into the bottom layer easily from outside the scaffold and that the top layer was more cell dense because

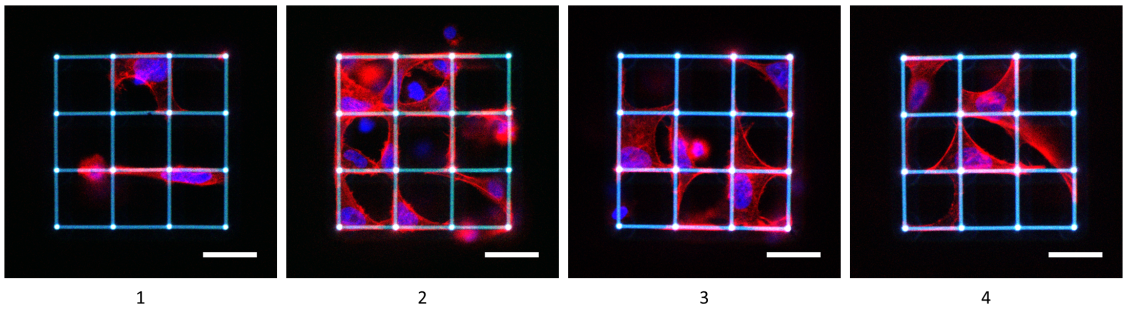

Figure 3.25: Top view of big square (BS) scaffolds seeded with 120,000 HeLa cells/cm^2 after 2 days of culture. Imaged with 20x water dipping lense (Leica, Erasmus). Stained for F-actin (phalloidin, red) and DNA (DAPI, blue). Scalebar = 30 µm.

some cells sedimented here during seeding whereas the middle region is less accessible for both cells coming from bottom and upper layers due to more obstructions. However, the scaffold beam to cell ratio was very different here: the beams of the woodpile structure had a diameter of 20 µm whereas in this research they were 1-2 µm. This significantly reduces the chance of a HeLa cell sedimenting on one of the beams, however it could be that the pore size is just small enough so that a HeLa cell could be caught "in the web". If this is the case we would expect the occupancy pattern to be even more shifted towards the top for the scaffolds with smaller pore size, especially since the cells likely migrate slower because of the higher chance of encounters with obstructions [76]. This does indeed seem to be the case if we look at the phalloidin fraction at each height (see figure L.1A-D). However, since we did find cells inside of these scaffolds we can conclude that HeLa cells are still able to invade and move around in a scaffold with a pore size of 15 µm.

It would be interesting to do some live imaging or to compare a sample fixed after 1 day versus 2 days or more to investigate the migration patterns. Given enough time to migrate, would the cells eventually distribute themselves uniformly across the scaffolds or would there still be a preference for one specific location? It could be hypothesized that if the scaffold got crowded, cells would seek a spot with optimal access to nutrients. That could be the reason why in the experiment of Turunen et al., after some time cells migrated upwards in the microtower without openings but remained mostly in the bottom of the tower with openings [53].

Further, we also tested small circular and square scaffolds that were equally big in volume as the big square and circular scaffold (see figure 3.29). Unfortunately, we were unable to count the cells for each layer because of severe shadowing in the scaffolds with smaller pore size, however it was possible to count the number of cells on top of the scaffold. We found that cells could also grow in these new scaffolds and they even reached the top, however they did seem less preferable than the BS scaffold where on average 12 cells were found compared to 4-5 on the scaffolds with smaller pore size (see figure 3.28A).

Still the standard deviation is quite large and the cell density near the scaffold (within circle of radius 105 µm) is considerably lower in all SSB and SCB scaffolds than in the BS scaffold (see figure 3.28B).

Interestingly, the BS scaffolds all have a higher density closer to the scaffold than further away, whereas the opposite trend is noticeable for the SSB, even for scaffolds where the density within a radius of 280 µm is about the same. One might wonder whether it could be that the BS scaffold attracts cells or promotes proliferation in near regions as opposed to the scaffolds with smaller pore sizes. In order to rule this trend out as a coincidence, the number of samples must be increased to ensure statistical significance.

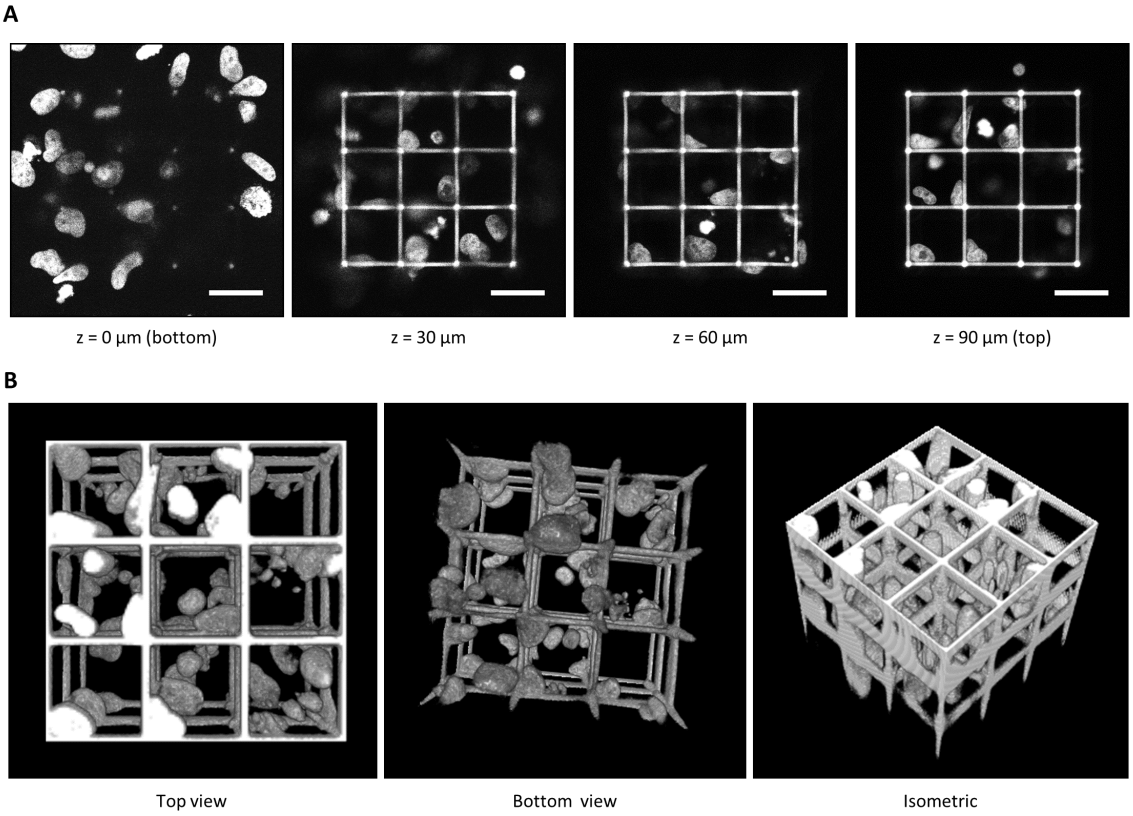

Figure 3.26: Big square (BS) scaffold seeded with 120,000 HeLa cells/cm^2 after 2 days of culture (scaffold 2 in figure 3.25). Imaged with 20x water dipping lense (Leica, Erasmus). A) 2D view of slices at different heights in blue channel (DAPI). Scalebar = 30 µm. B) 3D reconstruction of blue channel, made in Fiji/ImageJ.

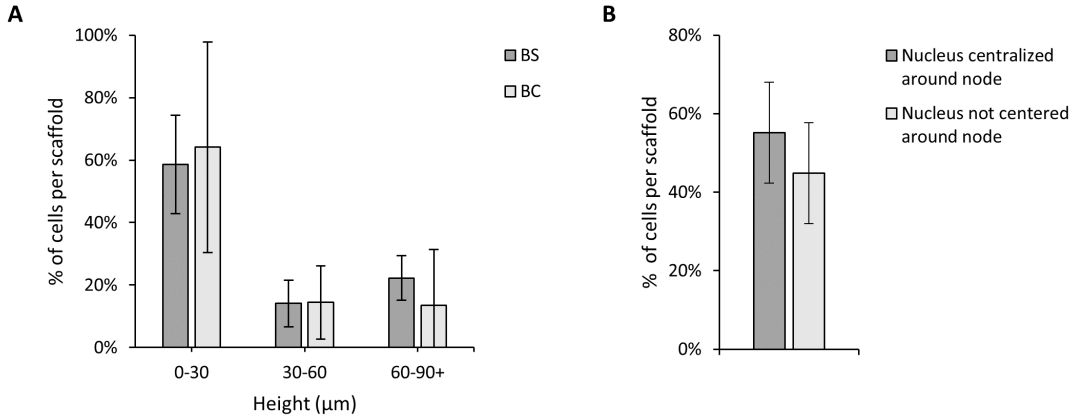

Figure 3.27: Analysis of nucleus location in scaffolds on substrate seeded with 120,000 cells/cm^2. A) Distribution of cells within big square scaffolds (N = 4) and big circular scaffolds (N = 4). B) Percentage of nuclei within big square scaffolds (N = 4) that are centralized around a node versus not centralized around a node.

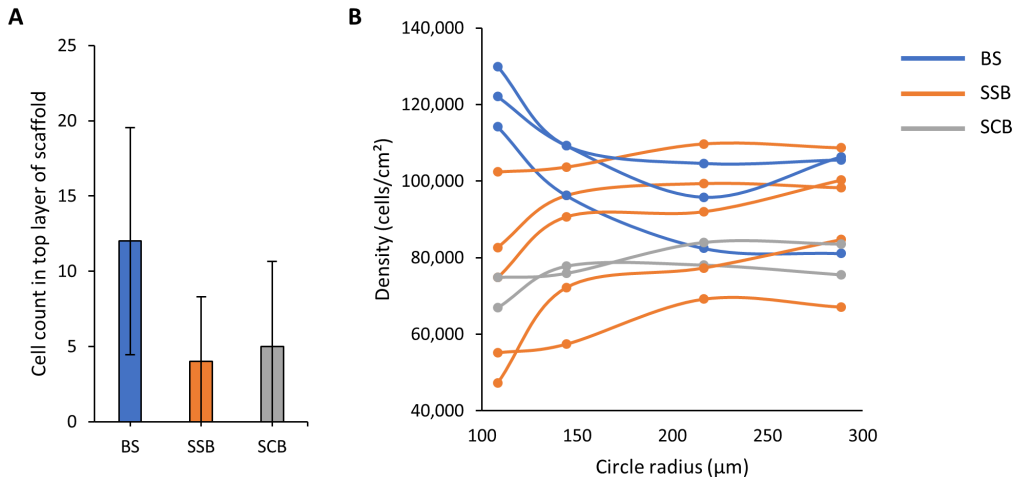

Figure 3.28: Analysis of HeLa cells in big square (BS), big small square (SSB) and big small circular (SCB) scaffolds after 2 days of culture (seeding density: 25,000 HeLa cells/cm^2). A) Cell count in top of scaffold for three scaffold types: BS (N = 3), SSB (N = 5) and SCB (N = 2) with standard deviation. B) Cell density within region of increasing circular perimeters around scaffold per scaffold type.

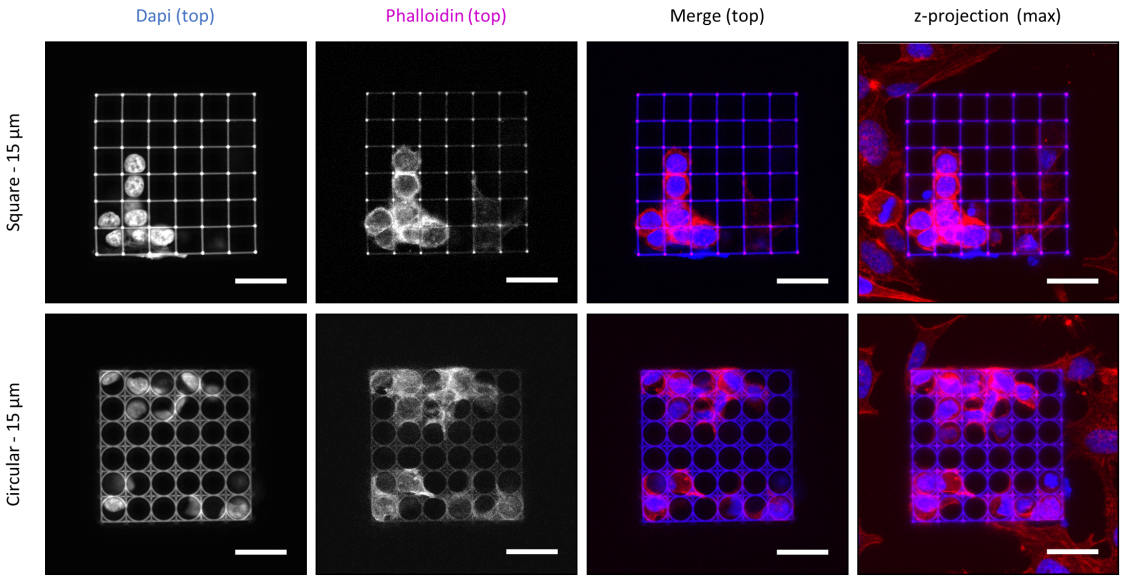

Figure 3.29: Big small square scaffold (SSB) and big small circular scaffold (SCB) with HeLa cells after two days of culture (seeding density: 25,000 HeLa cells/cm^2). Cells stained for F-actin (phalloidin, red) and DNA (DAPI, blue). Imaged with 20x water dipping lense (Leica, Erasmus). Scalebar: 30 µm.

3.2.3.4 Phalloidin and DAPI z-projection occupancy

From the percentage of phalloidin and DAPI in the z-projection of the scaffolds, we can see that the difference between a seeding density of 120,000 versus 160,000/cm^2 is quite large (see figure 3.30A and B). The amount of phalloidin is on average twice as high for the higher seeding density (56% versus 24%) and for DAPI even four times higher (40% versus 11%). However, it must be noted that for the DAPI in the z-projection, the high density values are biased towards a higher number because of strong diffraction effects in the blue channel for the images of this substrate. From the z-projection fraction it does not seem that HeLa cells have a clear preference for one scaffold geometry or pore size over another.

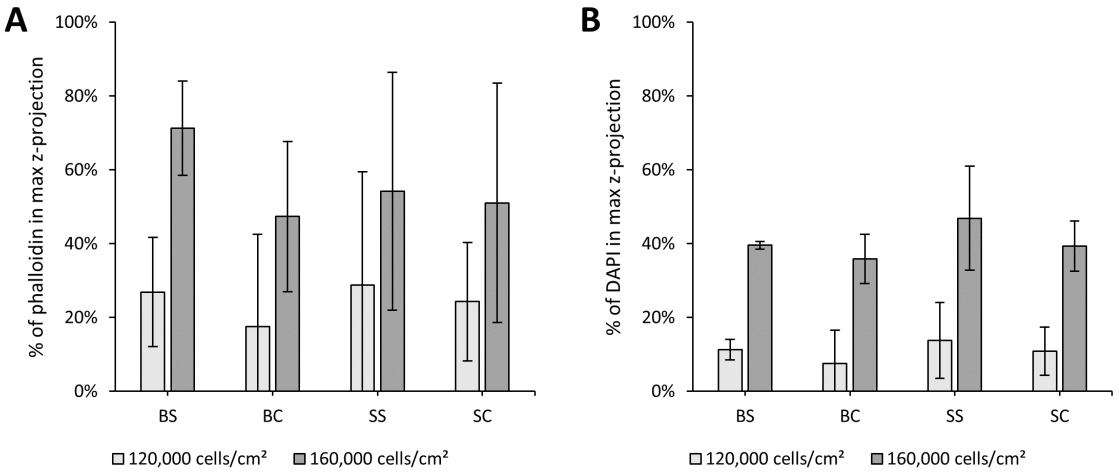

Figure 3.30: Analysis of scaffold occupancy by HeLa cells after two days of culture, based on confocal stacks. Two different seeding densities: 120,000 and 160,000 cells/cm^2 and four types of scaffolds: BS, BC, SS, and SC. Total number of analysed scaffolds is 30. N = 4 for each type of scaffold except N = 2 for the BS with seeding density of 160,000 cells/cm^2. A) Percentage of phalloidin in maximum z-projection of scaffolds. B) Percentage of DAPI in maximum z-projection of scaffolds (corrected for autofluorescence of scaffold).

3.2.3.5 Volumetric phalloidin occupancy

While the z-projection gives a good indication of scaffold occupancy by cells, it is of course an oversimplified method. Therefore we further look at the volumetric occupancy of phalloidin within the scaffold. When the same threshold is used, the volumetric occupancy should always give a lower or equal value than the area occupancy in the z-projection. This can be explained as follows.

Since the maximum z-projection selects the pixels of the highest intensity from every slice throughout the stack, the number of pixels in a slice that have an intensity higher than the threshold value can never be higher than the number of pixels in the z-projection that have an intensity higher than the threshold value. Therefore $A_i \leq A_z$ where A_i is the area of phalloidin in slice i and A_z is the area of phalloidin in the maximum z-projection. Thus $\sum A_i \leq N \times A_z$, which means that the volumetric occupancy is lower or equal to occupancy in the z-projection (see equation 2.7).

However, this is not the case here as different thresholds were used. This might be a contributor to the poor correlation between the z-projection and volumetric occupancy of phalloidin in the scaffolds (see figure M.1).

There is not a clear pattern of cell occupancy per height for each scaffold type. For the big square scaffold, the pattern does correlate with the location of nuclei, which is further discussed in section 3.2.3.3. For both densities we see that the average occupancy is lowest in the big circular scaffold, which we also saw in the z-projection, indicating that either HeLa cells prefer the other scaffolds or can grow, proliferate and migrate faster in the other scaffolds. Interestingly, for the substrate seeded with 120,000 cells/cm^2, the small circular scaffold seems to promote cell occupancy really well. This

was not observed in the z-projection. For the higher seeding density, the occupancy varies a lot between scaffolds of type SS and BC and is more constant for the scaffolds with larger pore size.

There is not a large difference between the volumetric phalloidin occupancy for the two different seeding densities ($\approx 35\%$ for 160,000/cm^2 versus $\approx 30\%$ for 120,000/cm^2), which we did see for the z-projection. It is not sure whether this is an effect of the different linear thresholds in the algorithms for both samples.

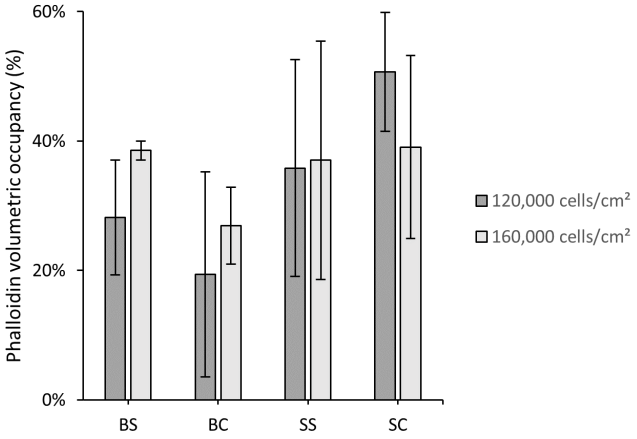

Figure 3.31: Volumetric occupancy of phalloidin in the scaffolds per scaffold type for a seeding density of 120,000 (N = 16, 4 of each scaffold type) and 160,000 HeLa cells/cm^2 (N = 14, 4 of each scaffold type except for BS) with standard deviation error bars.

Discussion

Analysing the volumetric occupancy of phalloidin in the scaffolds in this way by-passes the need for a 3D reconstruction of the stack images, thus allowing the analysis of lower resolution images such as in our case. However, the method does have its shortcomings. While it does give an indication of cell occupancy, the results are hard to interpret. Since the amount of F-actin per cell might not be constant, it could be that a scaffold with a higher occupancy does not necessarily contain more cells, but the cells in this type of scaffold rather contain more F-actin filaments.

Another difficulty of this method of analysis is how to determine an intensity threshold for each scaffold enabling a fair comparison. Even if imaging conditions such as laser power were kept constant and the scaffold were of same height and volume, the scaffolds with a smaller pore size would be more material dense and thus absorb or diffract more of the incoming light. This effect could be minimized if shorter scaffolds were used.

In our case specifically, the two substrates seeded with 120,000 and 160,000 cells/cm^2 respectively were imaged with different confocal microscopes, thus introducing even more variables to the analysis (e.g. laser intensity, excitation wavelength and resolution). Therefore it is hard to estimate the relation between seeding density and volumetric occupancy.

Another factor that contributes to this, is that the scaffold volume and height was not kept constant for each scaffold geometry and pore size. Since it costs time for cells to migrate from the substrate up to the top of a scaffold, it gives shorter scaffolds an advantage. This could explain why the small circular scaffold (height of 45 µm) on the substrate with the higher seeding density has the highest volumetric occupancy, namely 50%. This is followed by 35% in the small square scaffold (height: 60 µm), 28% in the large square scaffold and 20% in the large circular scaffold (both 30 µm high). The fact that there is a higher occupancy in the BS versus the BC which have the same volume, could be due to the fact that because of the geometry, the pore size area or free space is larger and allows for faster migration. For fibrosarcoma cells in 2PP-fabricated woodpile structures with varying lateral pore size it was indeed found that the overall mean speed of the cell increased with increasing pore size from 12 to 110 µm [76]. It was observed that the cell distribution uniformity decreased with decreasing pore size, which combined with the decreased migration speed indicates

that the matrix obstructs and prevents free movement in smaller sized pores. This difference in uniformity can also be observed for the HeLa cells if we compare the small circular and square pores in figure 3.29 with the large square scaffolds in figure 3.25.

Moreover, they saw that cells attached and moved predominantly along the beams in the 110-µm scaffold, while they occupied the entire pore in the smaller scaffolds. While we did not measure cell movement over time, the same pattern of movement seems to be present in the scaffolds of our experiments (see figure 3.21 and 3.22).

Trautmann et al. also carried out a study on 2PP scaffolds, similar to the square scaffolds of this report but with a closed outer side and different pore sizes of 10, 15, 30, 45, 60 and 90 µm [59]. From counting the nuclei present on the top of these scaffolds after 3, 6 and 9 days of cell culture they found that fibroblasts prefer to grow on scaffolds with a larger pore size, seemingly saturating at a density of 150,000 nuclei/cm^2 after 6 days of culture on the 60 and 90 µm pores and covering the scaffolds with a dense cell layer. We did not obtain the same result for HeLa cells which could be because of the varying volume as mentioned before. However, it is also questionable whether the cell density on top of the scaffold is representative for the rest of the scaffold.

Even if we find that more cells are present on or in a certain scaffold, we would need more in depth research to find out what biological processes are behind this. It could mean that the scaffold stimulates cell proliferation or growth but another explanation could be that it is easier to migrate within a certain scaffold. In turn, this promotion of certain cell processes could be due to the amount of access to nutrients, room for movement (pore size), confinement within the scaffold, a geometry or roughness that promotes focal adhesions, an uneven distribution of gelatin, the flexural stiffness of the structure, curvature and so much more.

3.2.3.6 Correlation with surrounding cell density

During cell seeding, the cells are never distributed homogeneously which may lead to unfair advantages for scaffolds if the surrounding area has a larger number of cells present (see figure 3.22B). For the scaffolds on the substrate with the seeding density of 120,000 cells/cm^2 (n = 16 scaffolds, 4 of each type), we found that the cell density in the surrounding region (740 x 740 µm) of the scaffolds ranges from 20,000 to 100,000 cells/cm^2 (see figure 3.32) which is a very large variation. Therefore, it is likely that the obtained scaffold occupancy is linked to the cell density in the surroundings of the scaffold.

In order to study the effect of cell density on the occupancy results, we plotted the surrounding cell density (based on the number of nuclei in the surrounding area of 740 x 740 µm) versus the z-projection of DAPI and phalloidin for the substrate with seeding density 120,000 cells/cm^2 (n = 16 scaffolds, 4 of each type, see figure 3.33) and the surrounding density versus the volumetric occupancy of phalloidin in scaffolds seeded with 120,000 and 160,000 cells/cm^2 (n = 30 scaffolds, see figure 3.34). We see that there is a moderate positive correlation between the fractions of DAPI and phalloidin in the z-projection and the density.

From figure 3.34A it follows that there is definitely a positive correlation between the volumetric occupancy and surrounding density of the scaffolds. This means that no conclusions can be drawn about cell preference for a scaffold based purely on the volumetric occupancy, since the results were likely influenced by the cell distribution on the substrates.

In order to have a fairer comparison, we plotted a linear trendline through the points of each scaffold type separately (see figure 3.34B). This way, we can look at the relative volumetric occupancy per cell density for each scaffold type. From this graph it seems that the circular scaffold with small pore size promotes cell colonization the best, followed by the small square scaffold. While the scaffolds with bigger pore sizes are less occupied at the same surrounding cell density. This could be an effect of the difference in overall scaffold size between the different pore sizes and namely the varying heights: while the scaffolds with larger pore sizes are about 90 µm high, the small square scaffold is 60 µm high and the small circular scaffold is even shorter with a height of 45 µm. For example, in order to obtain the same volumetric occupancy in a 90 µm-high scaffold as a 45 µm-high scaffold of the same width and length, you would need twice as many cells/cm^2. This means that either more cells should migrate inwards from outside the scaffold or the cells should proliferate

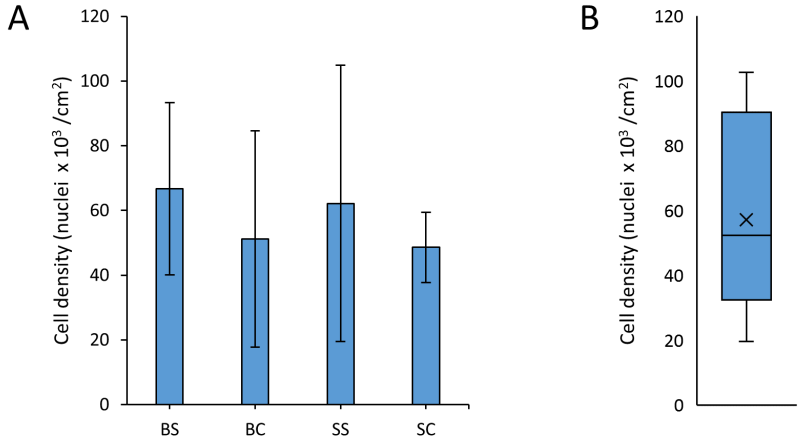

Figure 3.32: Cell density in surrounding area (740 x 740 µm) of scaffolds on substrate seeded with 120,000 cells/cm^2. A) cell density in surrounding area per scaffold type: BS, BC, SS and SC. n=4 for each scaffold type. B) Total cell density distribution for all scaffolds, N=16 (consisting of 4 scaffolds of 4 types).

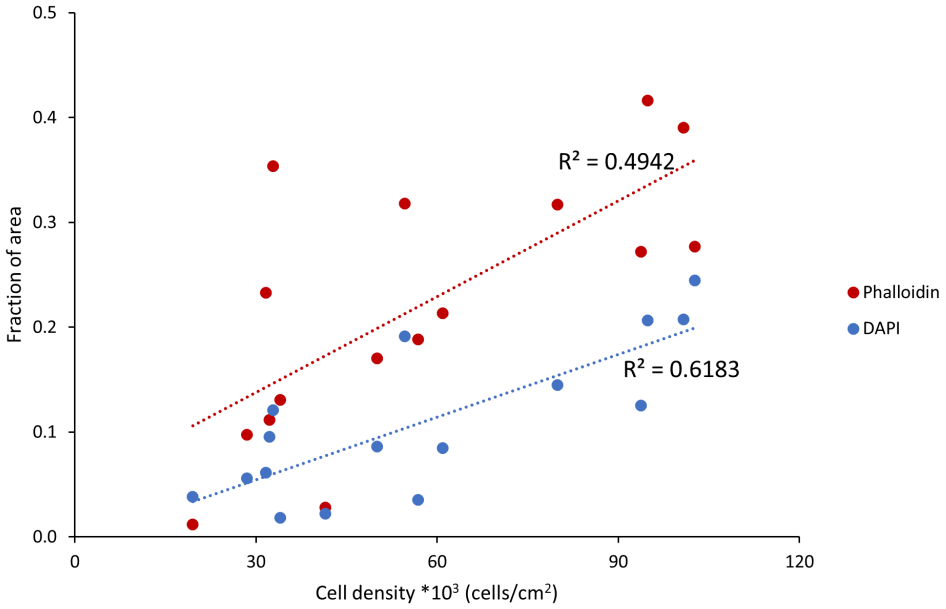

Figure 3.33: Cell density in surrounding area (740 x 740 µm) of scaffolds on substrate seeded with 120,000 cells/cm^2 plotted versus the phalloidin and Dapi fraction in the maximum z-projection of the scaffolds, including linear trendlines. N=16 (consisting of 4 scaffolds of 4 types).

more. Moreover, cells would have to migrate over a larger distance in vertical direction, which costs time. Even though the cells likely migrate somewhat faster in scaffolds with larger pore sizes, the height difference gives an unfair bias towards the scaffolds with smaller pore sizes. The difference in circumference of the scaffolds may also play a role. It might be beneficial for cell colonization to have a relatively large ratio of circumference to scaffold area as migration inwards may then be easier and the distance that has to be traveled also shorter.

In order to exclude the effect of the overall scaffold size on the volumetric occupancy, the experiment should be repeated with scaffolds of similar overall sizes. Only then can we draw a conclusion on which pore size promotes better colonization.

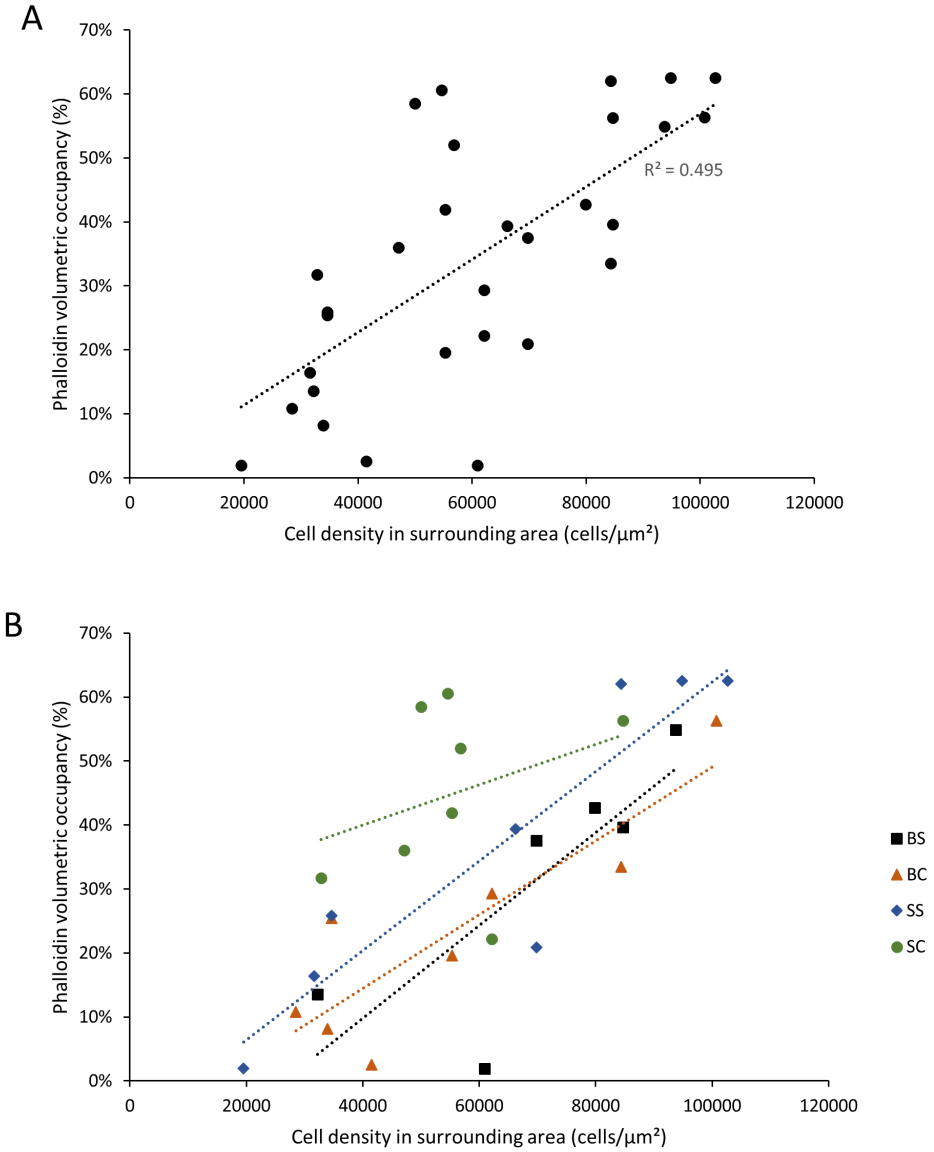

Figure 3.34: Cell density in surrounding area (740 x 740 µm) of scaffolds versus phalloidin volumetric occupancy of scaffolds. Data points collected from two substrates, seeded with respectively 120,000 and 160,000 HeLa cells/cm^2. In total 30 scaffolds were analysed: BS (6x), BC (8x), SS (8x) and SC (8x). A) Phalloidin volumetric occupancy versus cell density in surrounding area with linear trendline: R^2=0.495. B) Phalloidin volumetric occupancy versus cell density in surrounding area per scaffold type including linear trendlines for each type.

3.3 Preliminary results on the neural differentiation of embryonic stem cells growing on 2PP scaffolds

3.3.1 ESC density and viability

In order to find a good cell seeding density for mESC culture on IP-Dip scaffolds, we plated 30,000, 80,000 and 160,000 cells/cm^2 respectively. While the lowest density seemed to result in more cell death, the mESC at other densities grew well and successfully colonized the scaffolds (see figure 3.35). The samples with a seeding density of 80,000 and 160,000 cells/cm^2 are discussed in the next sections. The samples were imaged under different confocal configurations.

3.3.2 ESC morphology and location

From the confocal images of the cells in the scaffold (see figure 3.35), we observe that there are not many mESCs located in the top part of the scaffolds (at z=h). This is in contrast with the HeLa cells. It indicates that HeLa cells migrate more and tend to move separately from the other cells so they can climb up the scaffold, whereas mESCs stay adherent to the colony where they come from. We see that mESC colonies grow from the bottom up and they apparently need more time to reach higher parts of the scaffolds.

Interestingly, in figure 3.35 B, for the circular scaffold (30 µm gap size) it seems that the ESC colony has some difficulties entering the scaffold and therefore chooses to wrap around it. This phenomenon is only seen in one other scaffold. Since this happened only once and in other cases the cells clearly have no problem colonizing a scaffold, it might be related to the location where cells were initially seeded.

Furthermore, we found the same discrepancy between confocal images and SEM images (see figure 3.36) as for the HeLa cells: a distortion caused during fixation or dehydration. We can however nicely see how the e.g. small circular scaffold is immersed in the mESC colony.

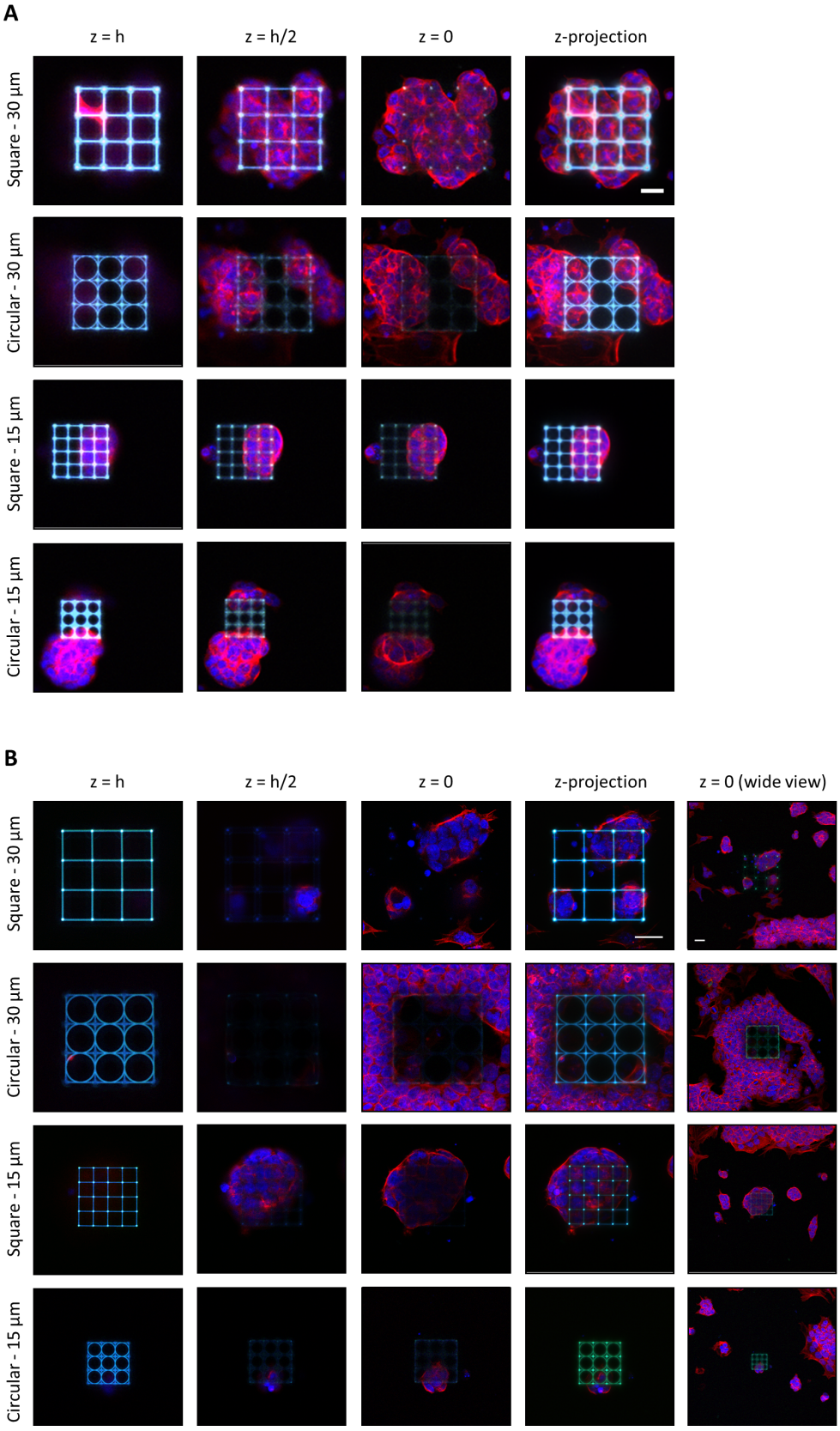

Figure 3.35: mESC in scaffolds after two days of culture. Two different seeding densities. Image at top of scaffold (z=h), halfway through scaffold (z=h/2) and at the substrate surface/bottom of scaffold (z=0), maximum z-projection and a wide view of the substrate surface. Samples stained for F-actin with Phalloidin (red) and DNA with DAPI (blue). Scaffold is autofluorescent in green and blue. Confocal stacks taken in three channels: blue, green and red. A) Seeding density 80,000 cells/cm^2. Imaged in configuration A. Scalebar = 30 µm. B) Seeding density 160,000 cells/cm^2. Imaged in configuration C. Scalebar = 30 µm.

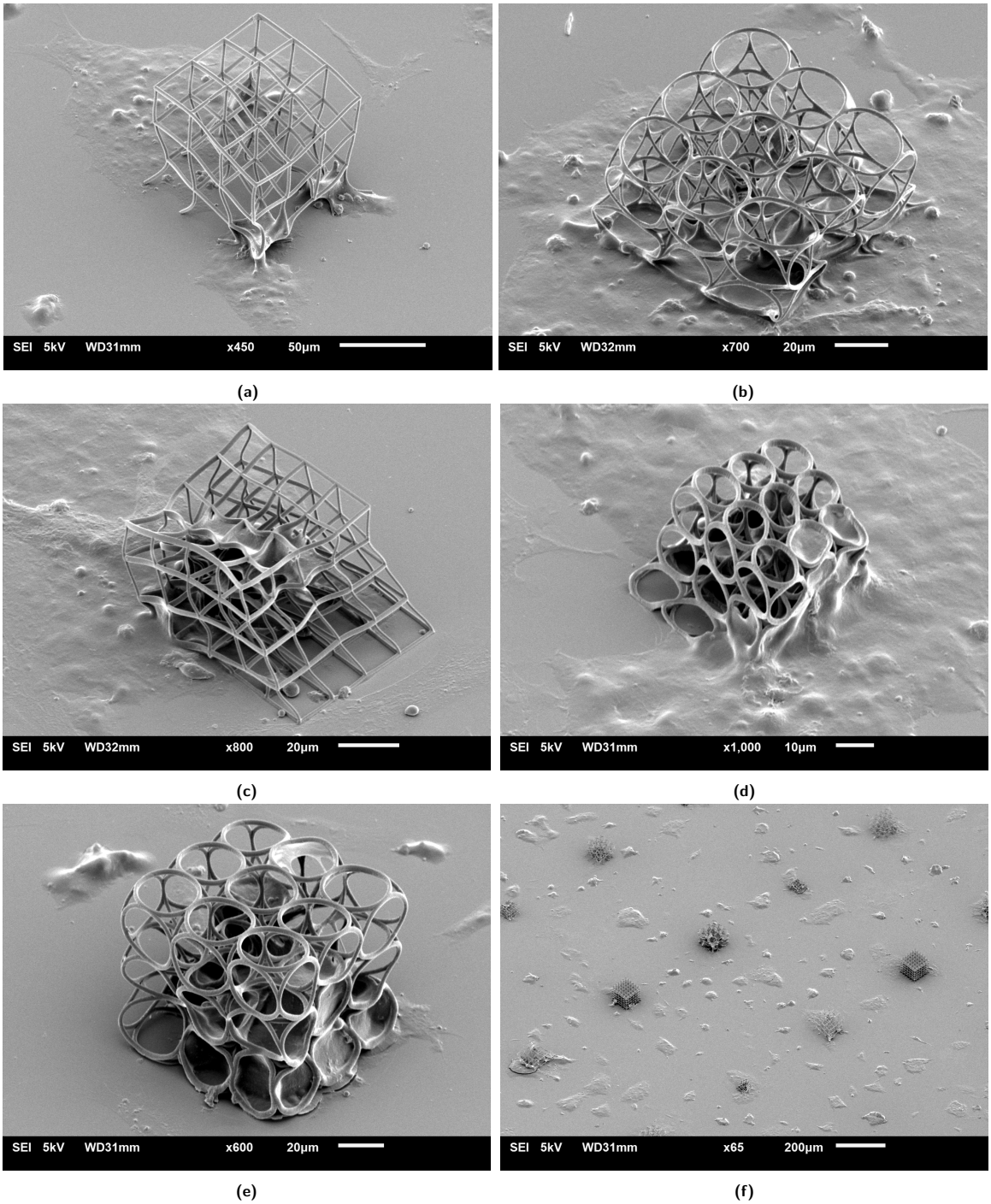

Figure 3.36: mESCs in scaffolds after two days of culture. Cell seeding density: 160,000 cells/cm^2. a) BS, b) BC, c) SS, d) SC, e) BCF and f) an overview of the scaffold placement on the substrate. (Substrate slightly damaged during handling before imaging.)

3.3.3 Occupancy of scaffolds in z-projection

The area occupancy (%) of mESC in the scaffolds in the maximum z-projection was analyzed for phalloidin (F-actin) and DAPI (nuclei). For the sample with seeding density of 160,000 cells/cm^2 there were 4 scaffolds of each type (BS, BC, SS, SC and BCF). For the seeding density of 80,000 cells/cm^2 there were 4 scaffolds of type BS, SS and BCF and 3 of type BC and SC.

For both seeding densities, the average phalloidin occupancy in the z-projection was highest for BS (50% and 76% respectively) and lowest for the SC (19% and 32% respectively). For the seeding density of 160,000 cells/cm^2 this also holds for the DAPI occupancy (69% in BS and 26% in SC). However, for the lower seeding density, the DAPI occupancy is similar in all the scaffolds: 22-29%.

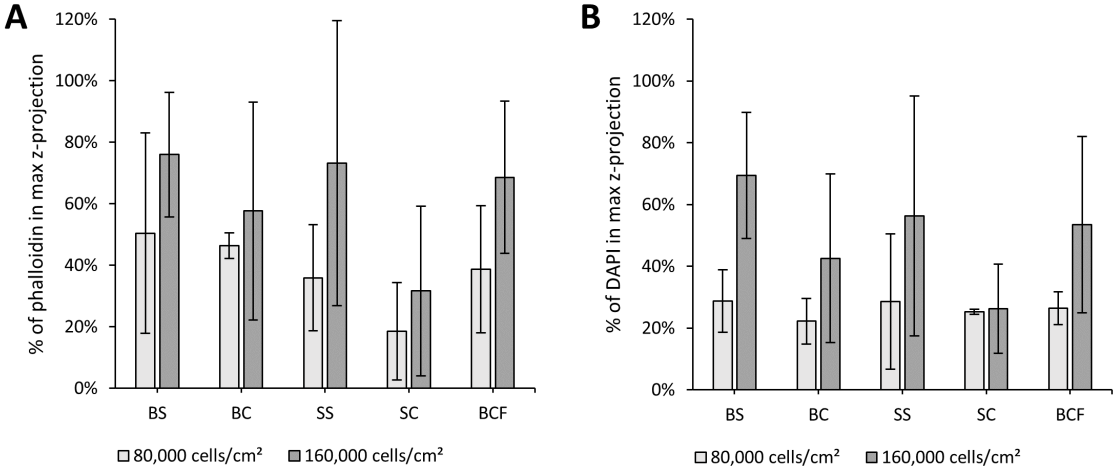

Figure 3.37: Analysis of scaffold occupancy by mESC after two days of culture, based on confocal stacks. Two different seeding densities: 80,000 and 160,000 cells/cm^2 and five types of scaffolds: BS, BC, SS, SC and BCF. Total number of analysed scaffolds is 38. N = 4 for each type of scaffold except N = 3 for the BC and SS with seeding density of 80,000 cells/cm^2. A) Percentage of phalloidin in maximum z-projection of scaffolds. B) Percentage of DAPI in maximum z-projection of scaffolds (corrected for autofluorescence of scaffold).

3.3.4 Formation of ESC colonies

A number of 91 ESC colonies in regions outside of the scaffolds were evaluated and 17 colonies that were connected to scaffolds, either occupying a scaffold completely or partly. For example, the large square scaffold in figure 3.35A is almost fully occupied by one colony whereas in 3.35B the large square scaffold contains three colonies. Even though the bottom colony in figure 3.35A attached to the small circular scaffold is mostly located outside of the scaffold, it is still counted in the scaffold group as it is attached to a scaffold. The colonies that were considered were larger than 1000 µm^2, which is a colony of about 8 cells.

As expected there is a positive correlation between the projected area of a mESC colony and the height that it reaches (see figure 3.38A). The colonies found in the scaffolds had a relatively large projected area compared to the colonies on the surface, where a large percentage of 50% are in the smallest projected area category (see figure 3.38B). Furthermore, the scaffolds contained relatively higher scaffolds than were found on the surface (see figure 3.38C). These results already indicate that the scaffolds may promote colony growth in both the horizontal and vertical direction. This hypothesis is further strengthened when we compare the height distribution of scaffolds within certain project area bins (figure 3.38D). We found that the height for the same colony footprint is about 1.5 times larger for colonies within scaffolds versus on the substrate surface.

Lastly, we investigated the colony height per scaffold type. Interestingly, none of the colonies reached a height larger than the highest scaffolds (90 µm) and the average reached height was

similar in all scaffold types which could mean that further vertical growth was limited due to the time constraint. The height of colonies within the SC scaffolds was relatively small compared to the other scaffold types, but since the sample size of colonies within SCs was 2, this has no statistical significance. However, it is in agreement with the phalloidin and DAPI occupancy in the z-projection. It is also plausible that because the SC scaffold was the lowest of all scaffolds (45 µm), the colonies did not reach a bigger height since there would be no more support on top. In order to test this hypothesis, the sample size and possibly culture time should be increased.

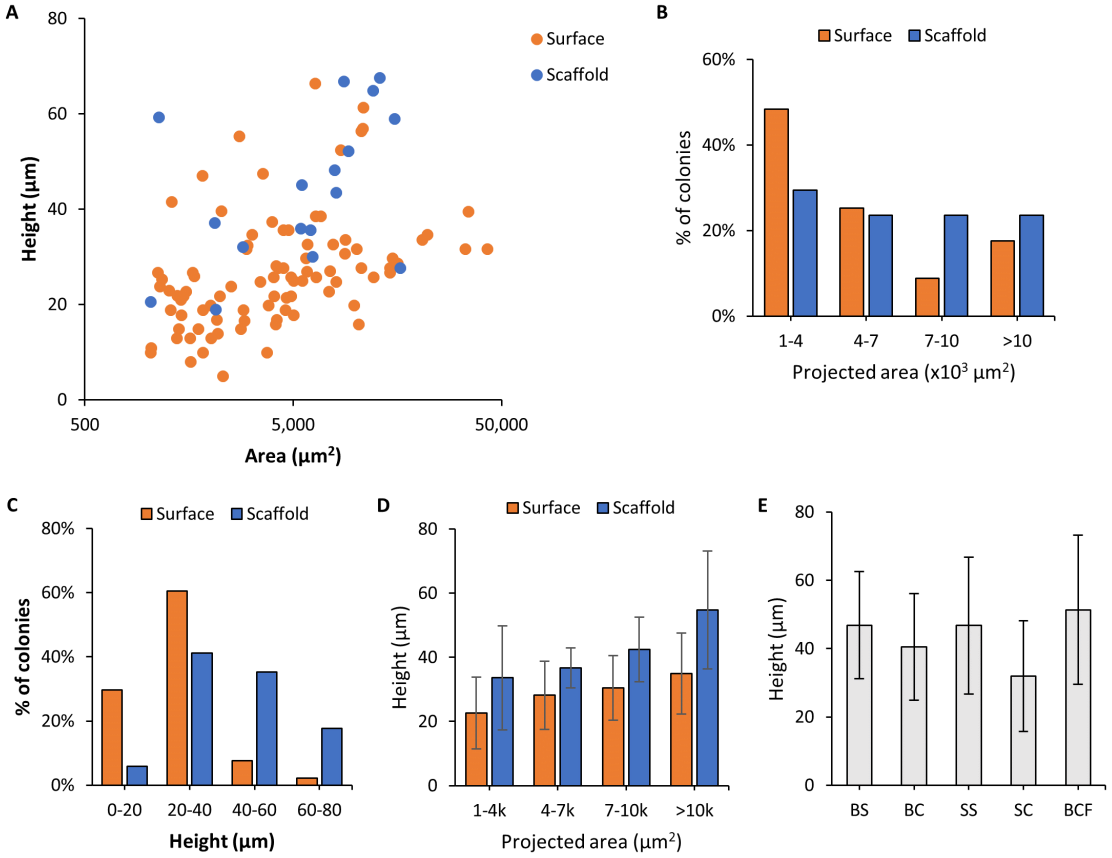

Figure 3.38: The height of mESC colonies (> 1000 µm^2) of varying sizes was analysed, the colonies were sorted by location: the region outside of the scaffolds (surface, n=91) or connected to scaffolds (scaffold, n=17). A) Height of colonies versus the colony area. B) The percentage of colonies per projected area category. C) The percentage of colonies per projected height category. D) Height per projected area category. E) The height of colonies per scaffold type.

3.3.5 ESC differentiation

In this experiment mESCs were differentiated towards neural progenitor cells (NPCs) for 5 days on a substrate that contained 4 scaffolds of each of the 5 types: BS, BC, BCF, SS and SC (a total of 20 scaffolds). An overview of the cells in the different scaffold types (except the BCF) is given in figure 3.40 and a 3D rendering was constructed for the big square scaffold (figure 3.39). Firstly, we noticed that in contrast to the previous experiment (no differentiation, culture for 2 days) cells were present in the top layer of the scaffolds more often. This is likely due to the longer culture time, namely 5 days instead of 2 days. Second, we observed differentiation marker in cells that are on top of the scaffolds, for example in the big square scaffold of figure 3.40. This could be a result of a higher motility in differentiated cells or because cells in the outer layer of an mESC colony are inclined to differentiate first.

We demonstrated that mESC colonies can successfully colonize and start to differentiate inside 2PP printed scaffolds of different geometries. Even though the signal was faint, the differentiation marker Nestin was found in colonies outside of the scaffolds as well as inside the scaffolds. The signal of differentiation marker was likely faint due to the relatively short culture time. From this experiment it is inconclusive whether the cells differentiated faster inside of the scaffolds versus on the flat substrate. However, the results obtained show how a preliminary differentiation of mESCs towards NPCs is possible within the developed 3D structures and can be starting point for future research involving longer cell culture times.

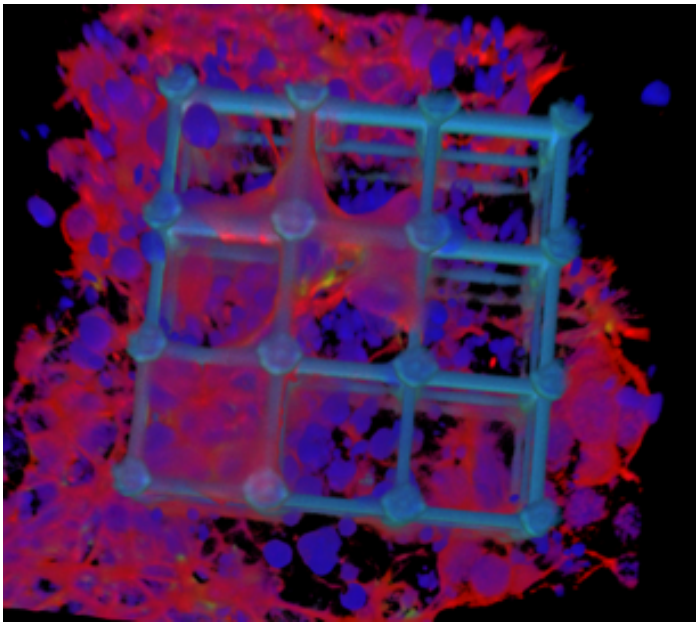

Figure 3.39: 3D rendering of differentiated ESC in big square scaffold (pore size 30 µm) of figure 3.40. Samples stained for F-actin with Phalloidin (red), DNA with DAPI (blue) and differentiation marker Nestin (green). Scaffold is autofluorescent in green and blue.

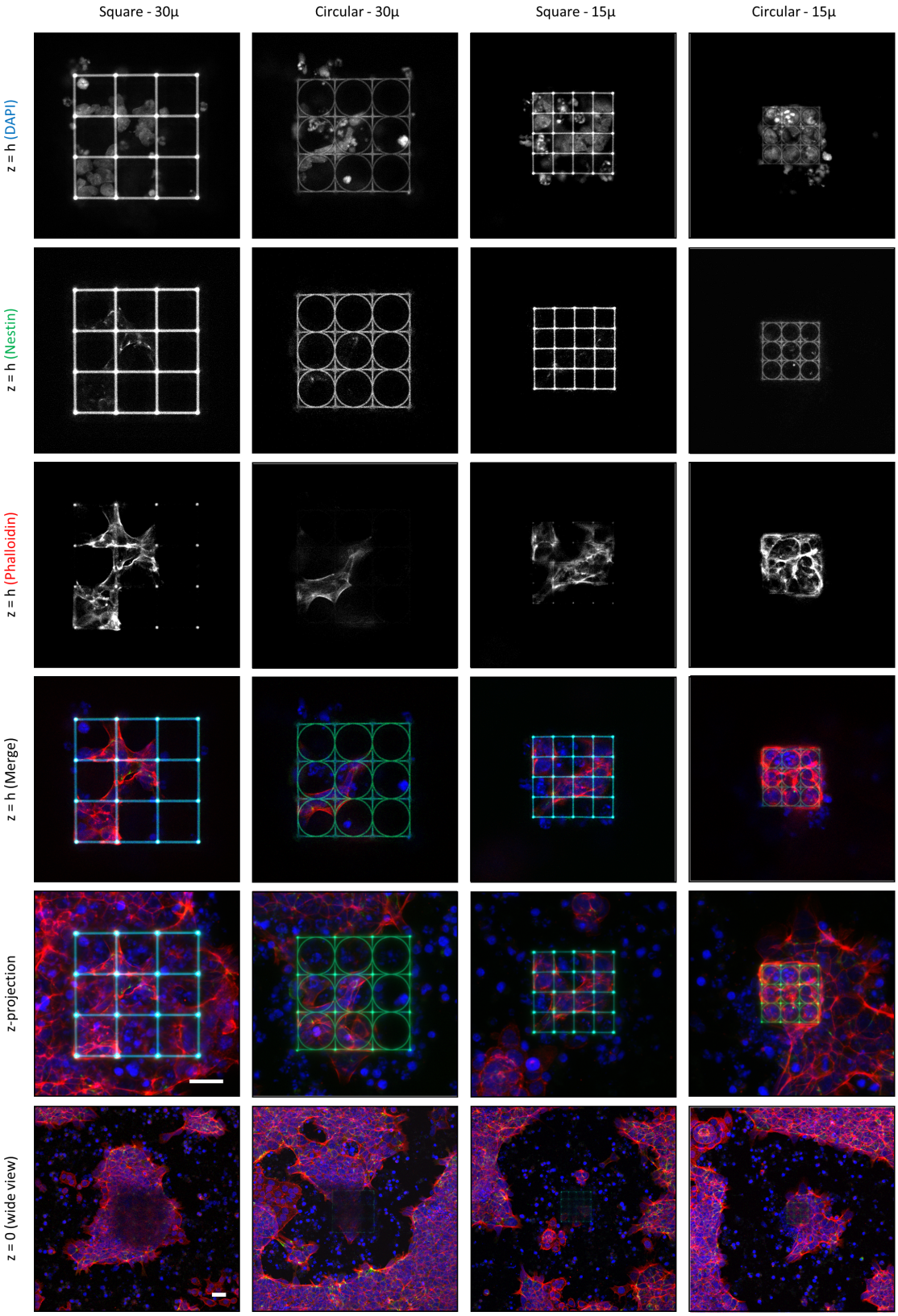

Figure 3.40: ESC after five days of differentiation into the neuronal lineage. Differentiation marker Nestin (green) is present, but in small quantities. Cells stained for F-actin (red, phalloidin) and DNA (blue, DAPI).

Chapter 4

Conclusion and Recommendations

4.1 Conclusion

During this research, we developed an approach for culturing cells on 3D 2PP IP-Dip scaffolds. Scaffold adhesion was greatly improved by employing a coating of Ormoprime on the fused silica substrate. The use of a silicone isolator (Press-to-Seal) to minimize the usage of cells and media was feasible but unfortunately not reliable. Anyhow, it could bring great advantages if the adhesion problem can be solved. It was shown to be crucial for data analysis to be able to take high resolution confocal images. Very detailed confocal reconstructions could be obtained of bare IP-Dip scaffolds via oil immersion, however this medium was not compatible with cells. The scaffolds with cells could be best imaged using a water dipping objective with the cells embedded in Vectashield. Another important factor in data analysis is determining the threshold algorithm because of the declining fluorescence intensity in the inner core of the scaffolds.

Furthermore, a clear discrepancy was observed between the images taken on a confocal and scanning electron microscope. Due to the dehydration of cells during preparation for SEM, the scaffolds severely deformed. By using only 2.5% GA instead of 1%GA-4%PFA for fixation of the cells, followed by graded ethanol series, this deformation could be somewhat decreased. Using HMDS did not show any improvement in comparison to letting the samples air dry. However, it is suspected that the variation in cell density between the substrates might have affected the outcome in favour of protocols employed with scaffolds containing a lower cell density. In any case, no method that was tried here was able to eliminate the effect of cell shrinkage which significantly decreases the amount of information we can extract from SEM images.

Next, the effect of curvature on the nuclei of HeLa cells was investigated on a sinusoidal 2.5D structure. More nuclei were found in the strongly concave region versus the strongly convex region and furthermore the nuclei aligned in the direction of least curvature. We also found that cells grown on a large flat area of IP-Dip show a smaller projected area than cells grown on a bare substrate, indicating that the small decrease in stiffness can already have an effect on the shape of nuclei.

Furthermore, we showed that HeLa cells can occupy 3D scaffolds of different geometries and migrate to the top of the scaffolds. There is no clear preference for a specific pore size (15 or 30 µm) or structure (square versus circular). The nucleus area of HeLa cells is smaller inside the scaffolds versus outside, which indicates a different cell morphology in 3D that is more spherical than flat. For the big square scaffold, the nuclei are often positioned at the nodes of the structure with their cell body expanding towards other nearby nodes. Most cells can be found at the bottom of this structure, and on average there are more cells on the top than in the middle.

Lastly, some preliminary tests were performed with mESCs. It was shown that they could successfully colonize scaffolds of all types but in some cases rather avoided the scaffolds. The mESCs occupied the small circular structure (pore size 15 µm) the least. Furthermore, the scaffolds may promote colony growth in the vertical direction. For colonies with the same projected area, the

height was increased by 1.5 times compared to the height of the colonies on the substrate surface. It was also demonstrated that mESCs that colonized scaffolds can be differentiated into the neural lineage.

All in all, these are promising results that can be used in further research regarding neural differentiation in 3D 2PP structures.

4.2 Recommendations

Here we will discuss the recommendations for further research per topic: fabrication/culture workflow, imaging, analysis, HeLa experiments and mESC experiments.

Fabrication and culture workflow

As mentioned before, the silicone isolator was able to provide great advantages when it worked properly, however it sometimes detached. It might be worth it to look into why this happened, different brands of silicone isolators or the possibility of using glue to attach the seal more securely. Another option is to omit the seal completely and go a different route such as printing the scaffolds on smaller substrates that would fit into a well-plate which is more manageable than using Petri dishes.

Regarding the scaffolds, it is recommended to have a relatively high contact area with the substrate in order to prevent detachment. For example, the big square scaffold that only touched the substrate with the cross-section of the beams detached, whereas scaffolds that had a larger footprint stayed put. Furthermore, it would be easier for analysis to start with shorter scaffolds (e.g. 60 or 30 µm high) which can be imaged better and for fair comparison, keep the inner volume the same for every pore size.

Since there will always be a bit of variation between the samples and scaffolds due to the nature of cell culture, it is wise to increase the number of duplicate samples and the number of scaffolds on each substrate.

Imaging

Since the confocal images give us a lot more information about the cells and the truthfulness of SEM images is greatly affected by the sample preparation, we find that the focus should be on confocal imaging in this kind of experiments. If one would do more research into SEM protocols, it is important to take into account the effect of cell confluency on the results.

In order to simplify the analysis of confocal images, it is suggested to carefully pick fluorescent markers. In the case of bulky IP-Dip structures, DAPI will almost hide in the background and it is hard to distinguish. Furthermore, since IP-Dip is fluorescent in the blue, automatic analysis will be easier when the nuclei are stained with a different fluorophore. Furthermore, one could think of suppressing the fluorescence of IP-Dip with Sudan black, which might also increase the image quality inside the scaffolds due to less background noise. Another option is to turn to a material that is not autofluorescent such as IP-Visio, which is also a biocompatible material.

Of course the imaging methods could always be optimized even further and it would also be really interesting to look into immersion media that have a similar refraction index to immersion oil but do not react with cells. If this is possible, it could greatly improve the imaging and analysis of larger 3D scaffolds.

Analysis

While the parameters that were measured during this research, such as volumetric dapi/phalloidin occupence, properties of the nucleus z-projection and height of mESC colonies, give an indication of preference of cells for certain structures or alignment, a lot more information can be derived from using a 3D analysis program such as Imaris. For example, for the curvature experiment one does not

have to rely on the projection which might change alignment of the nucleus and for the HeLa cells the volume and 3D shape of nuclei can be determined. However, to be able to use such a program, the image quality of the stacks must be sufficient.

It could also be beneficial to look into additional chemical markers such as for focal adhesions or proliferation to better compare the difference between cells growing in 3D scaffolds versus on the flat substrate. Do cells for example proliferate faster when in 3D?

Lastly, it would be very insightful to apply live cell imaging to track how cells move around in the 3D scaffolds.

HeLa experiments

It would be nice to repeat the curvature experiment with HeLa cells on a sine structure featuring less surface roughness. Would the alignment still take place? Furthermore, what is the effect of different curvatures on HeLa cells? Other structures, such as dips and hills could also be interesting to study in this regard.

mESC experiments and neuronal differentiation

We established that mESC can differentiate into the neural lineage inside the scaffolds, but what we would like to find out is if differentiation actually goes faster inside scaffolds compared to a 2D substrate. Therefore the mESC differentiation experiment should be extended and for example samples could be fixated at different days in order to create a timeline of differentiation. It would also be interesting to investigate whether mESC spontaneously differentiate into other lineages more on the substrate versus inside the scaffolds and to compare cell potency and death.

Furthermore, the curvature experiment could also be carried out with mESCs to see if curvature can influence their differentiation into the neural lineage.

Future steps should include differentiating the mESCs into neurons inside the scaffolds and trying to perform the neural differentiation of mESCS inside of a 3D scaffold made from a softer material (such as a hydrogel), as 2D research has shown that this could promote neural differentiation.

Chapter 5

Self-reflection

At the beginning of this project I had never seen a confocal image of a cell and had mostly seen SEM images of 3D structures with neurons which were clearly distinguishable from the structure. Therefore I expected that in my project, I would also be able to clearly see individual cells on the scaffolds and that a 3D rendering from a confocal image stack would be easy to make. I soon realized, as with many things in life, that it was more complicated than that. But I would say, that after taking and analysing many confocal and SEM images that I now have a good understanding of what is involved with growing cells on 3D microstructures.

During this project I have learned a lot, especially from doing a lot of experimental work. I can proudly say that I can now print structures with the Nanoscribe, image with SEM and confocal microscopy and have even learnt how to fix and stain cells. I feel like I have acquired quite good skills working with these instruments. I really liked that I could carry out most of the experimental work myself and gained experience in a biological lab. I definitely liked the interdisciplinary aspect of this project and that I got to learn and work with so many different knowledgeable and nice people. Additionally, I got the opportunity to present my results at a hDMT Brain-on-Chip meeting.

They say hindsight is 20/20 and I feel like that is definitely applicable to a master's thesis. There are many things that I would do differently if I had to do them again that could have simplified the analysis such as making the scaffolds shorter. However, I that is an inevitable part of research. Moreover, I feel like you only start to truly understand what to look for in literature when you have conducted experiments yourself, thus it is hard to plan well in advance.

This brings me to my next point: things do not always go as planned. My project goal started very ambitiously with multiple materials and differentiation of stem cells into neurons. However, I came to know that things took a lot more time than I estimated and there were also some delayed instrument trainings due to COVID which did not help my time management. This seems to be a trap that a lot of students fall into, but then again it is hard to estimate the time things will take when you have never done them before. In the end, my project focus had shifted multiple times but I am happy with the result and glad that we still got to differentiate mESCs on the scaffolds.

In the beginning I had trouble with determining what I wanted to do exactly, how to proceed and to take the lead. However, in the end I do feel like I brought in my own ideas. It also did not help that this field of research is relatively new, thus I could not really rely on established or standard methods of analysis.

I realize I need to work on my time management skills and found it hard to work effectively because I did not have a clear plan beforehand. Furthermore, I often found myself wanting to many different things at the same time as I had a lot of ideas and everything was interesting. This is seen in the report as I covered a broad area of subjects. I think it would have really benefited me if I was better at decision making so that I could have narrowed down my focus and perhaps perfected or researched one aspect better instead of covering more things in less depth.

Even though the project did not always go smoothly, I am glad that I persevered and finished writing the thesis and who knows, maybe this document can even form a nice starting point for the next student.

Bibliography

[1] L. Papadimitriou, P. Manganas, A. Ranella, and E. Stratakis, "Biofabrication for neural tissue engineering applications," *Materials Today Bio*, p. 100 043, 2020, ISSN: 2590-0064. DOI: 10.1016/j.mtbio.2020.100043.

[2] W. Z. Ray and S. E. Mackinnon, "Management of nerve gaps: Autografts, allografts, nerve transfers, and end-to-side neurorrhaphy," *Experimental neurology*, vol. 223, no. 1, pp. 77–85, 2010, ISSN: 0014-4886. DOI: 10.1016/j.expneurol.2009.03.031.

[3] C. Tomba, "Primary brain cells in in vitro controlled microenvironments : Single cell behaviors for collective functions.," Ph.D. dissertation, Université de Grenoble, 2014.

[4] U. of California - San Diego, *Why are neuron axons long and spindly? study shows they're optimizing signaling efficiency*, 2018. [Online]. Available: https://medicalxpress.com/news/2018-07-neuron-axons-spindly-theyre-optimizing.html (visited on 04/19/2020).

[5] H. Fischer, *Glial cell types*, n.d. [Online]. Available: https://en.wikipedia.org/wiki/Glia (visited on 04/19/2020).

[6] I. E. Palamà, S. D'Amone, and B. Cortese, in *Nanomaterials and Regenerative Medicine*, Y. Lin and T. Gong, Eds. 2016, ch. Mechanical guidance of cell migration, pp. 563–580, ISBN: 978-953-56942-3-6. DOI: DOI:10.5599/obp.9.0.

[7] M. Jones, *Stem cells diagram*, n.d. [Online]. Available: https://en.wikipedia.org/wiki/Embryonic_stem_cell (visited on 04/19/2020).

[8] V. M. Lee, S. A. Louis, and B. A. Reynolds, "The Central Nervous System," *Neural Stem Cells*, p. 6, 2015.

[9] S. Casarosa, Y. Bozzi, and L. Conti, "Neural stem cells: Ready for therapeutic applications?" *Molecular and cellular therapies*, vol. 2, p. 31, Oct. 2014. DOI: 10.1186/2052-8426-2-31.

[10] A. Trubelja and G. Bao, "Molecular mechanisms of mechanosensing and mechanotransduction in living cells," *Extreme Mechanics Letters*, vol. 20, pp. 91–98, 2018, ISSN: 2352-4316. DOI: 10.1016/j.eml.2018.01.011.

[11] T. R. Cox and J. T. Erler, "Remodeling and homeostasis of the extracellular matrix: Implications for fibrotic diseases and cancer," *Disease Models & Mechanisms*, vol. 4, pp. 165–178, 2011.

[12] K. Saha, A. J. Keung, E. F. Irwin, *et al.*, "Substrate Modulus Directs Neural Stem Cell Behavior," *Biophysical Journal*, vol. 95, no. 9, pp. 4426–4438, 2008, ISSN: 0006-3495. DOI: 10.1529/biophysj.108.132217.

[13] A. J. Engler, S. Sen, H. L. Sweeney, and D. E. Discher, "Matrix Elasticity Directs Stem Cell Lineage Specification," *Cell*, vol. 126, no. 4, pp. 677–689, 2006, ISSN: 0092-8674. DOI: 10.1016/j.cell.2006.06.044.

[14] S. Ali, I. B. Wall, C. Mason, A. E. Pelling, and F. S. Veraitch, "The effect of Young's modulus on the neuronal differentiation of mouse embryonic stem cells," *Acta Biomaterialia*, vol. 25, pp. 253–267, 2015, ISSN: 1742-7061. DOI: 10.1016/j.actbio.2015.07.008.

[15] A. Banerjee, M. Arha, S. Choudhary, *et al.*, "The influence of hydrogel modulus on the proliferation and differentiation of encapsulated neural stem cells," *Biomaterials*, vol. 30, no. 27, pp. 4695–4699, 2009, ISSN: 0142-9612. DOI: 10.1016/j.biomaterials.2009.05.050.

[16] P. C. Georges, W. J. Miller, D. F. Meaney, E. S. Sawyer, and P. A. Janmey, "Matrices with Compliance Comparable to that of Brain Tissue Select Neuronal over Glial Growth in Mixed Cortical Cultures," *Biophysical Journal*, vol. 90, no. 8, pp. 3012–3018, 2006, ISSN: 0006-3495. DOI: 10.1529/biophysj.105.073114.

[17] Y. Sun, K. M. A. Yong, L. G. Villa-Diaz, *et al.*, "Hippo/YAP-mediated rigidity-dependent motor neuron differentiation of human pluripotent stem cells," *Nature materials*, vol. 13, no. 6, pp. 599–604, 2014, ISSN: 1476-1122. DOI: 10.1038/nmat3945.

[18] S. K. Seidlits, Z. Z. Khaing, R. R. Petersen, *et al.*, "The effects of hyaluronic acid hydrogels with tunable mechanical properties on neural progenitor cell differentiation," *Biomaterials*, vol. 31, no. 14, pp. 3930–3940, 2010, ISSN: 0142-9612. DOI: 10.1016/j.biomaterials.2010.01.125.

[19] "Mechanosensitivity of astrocytes on optimized polyacrylamide gels analyzed by quantitative morphometry," vol. 22, p. 194 114, 2010. DOI: 10.1088/0953-8984/22/19/194114.

[20] L. A. Flanagan, Y.-E. Ju, B. Marg, M. Osterfield, and P. A. Janmey, "Neurite branching on deformable substrates," *Neuroreport*, vol. 13, no. 18, pp. 2411–2415, 2002, ISSN: 0959-4965. DOI: 10.1097/01.wnr.0000048003.96487.97.

[21] C. R. Kothapalli and R. D. Kamm, "3D matrix microenvironment for targeted differentiation of embryonic stem cells into neural and glial lineages," *Biomaterials*, vol. 34, no. 25, pp. 5995–6007, 2013, ISSN: 0142-9612. DOI: 10.1016/j.biomaterials.2013.04.042.

[22] A. I. Teixeira, S. Ilkhanizadeh, J. A. Wigenius, J. K. Duckworth, O. Inganäs, and O. Hermanson, "The promotion of neuronal maturation on soft substrates," *Biomaterials*, vol. 30, no. 27, pp. 4567–4572, 2009, ISSN: 0142-9612. DOI: 10.1016/j.biomaterials.2009.05.013.

[23] X.-f. Jiang, K. Yang, X.-q. Yang, *et al.*, "Elastic modulus affects the growth and differentiation of neural stem cells," *Neural Regeneration Research*, vol. 10, no. 9, pp. 1523–1527, 2015, ISSN: 1673-5374. DOI: 10.4103/1673-5374.165527.

[24] N. D. Leipzig and M. S. Shoichet, "The effect of substrate stiffness on adult neural stem cell behavior," *Biomaterials*, vol. 30, no. 36, pp. 6867–6878, 2009, ISSN: 0142-9612. DOI: 10.1016/j.biomaterials.2009.09.002.

[25] C. Cha, J. H. Jeong, J. Shim, and H. Kong, "Tuning the dependency between stiffness and permeability of a cell encapsulating hydrogel with hydrophilic pendant chains," *Acta Biomaterialia*, vol. 7, no. 10, pp. 3719–3728, 2011, ISSN: 1742-7061. DOI: 10.1016/j.actbio.2011.06.017.

[26] R. K. Willits and S. L. Skornia, "Effect of collagen gel stiffness on neurite extension," *Journal of Biomaterials Science, Polymer Edition*, vol. 15, no. 12, pp. 1521–1531, 2004, ISSN: 0920-5063. DOI: 10.1163/1568562042459698.

[27] A. P. Balgude, X. Yu, A. Szymanski, and R. V. Bellamkonda, "Agarose gel stiffness determines rate of DRG neurite extension in 3D cultures," *Biomaterials*, vol. 22, no. 10, pp. 1077–1084, 2001, ISSN: 0142-9612. DOI: 10.1016/s0142-9612(00)00350-1.

[28] J. W. Gunn, S. D. Turner, and B. K. Mann, "Adhesive and mechanical properties of hydrogels influence neurite extension," *Journal of Biomedical Materials Research Part A*, vol. 72A, no. 1, pp. 91–97, 2005, ISSN: 1552-4965. DOI: 10.1002/jbm.a.30203.

[29] J. B. Leach, X. Q. Brown, J. G. Jacot, P. A. Dimilla, and J. Y. Wong, "Neurite outgrowth and branching of PC12 cells on very soft substrates sharply decreases below a threshold of substrate rigidity," *Journal of Neural Engineering*, vol. 4, no. 2, pp. 26–34, 2007, ISSN: 1741-2560. DOI: 10.1088/1741-2560/4/2/003.

[30] C.-M. Lo, H.-B. Wang, M. Dembo, and Y.-l. Wang, "Cell Movement Is Guided by the Rigidity of the Substrate," *Biophysical Journal*, vol. 79, no. 1, pp. 144–152, 2000, ISSN: 0006-3495. DOI: 10.1016/S0006-3495(00)76279-5.

[31] L. G. Vincent, Y. S. Choi, B. Alonso-Latorre, J. C. d. Álamo, and A. J. Engler, "Mesenchymal stem cell durotaxis depends on substrate stiffness gradient strength," *Biotechnology Journal*, vol. 8, no. 4, pp. 472–484, 2013, ISSN: 1860-7314. DOI: 10.1002/biot.201200205.

[32] A. Marino, G. Ciofani, C. Filippeschi, *et al.*, "Two-Photon Polymerization of Sub-micrometric Patterned Surfaces: Investigation of Cell-Substrate Interactions and Improved Differentiation of Neuron-like Cells," *ACS Applied Materials & Interfaces*, vol. 5, no. 24, pp. 13 012–13 021, 2013, ISSN: 1944-8244. DOI: 10.1021/am403895k.

[33] M. Kabiri, M. Soleimani, I. Shabani, *et al.*, "Neural differentiation of mouse embryonic stem cells on conductive nanofiber scaffolds," *Biotechnology Letters*, vol. 34, no. 7, pp. 1357–1365, 2012, ISSN: 1573-6776. DOI: 10.1007/s10529-012-0889-4.

[34] F. Yang, C. Y. Xu, M. Kotaki, S. Wang, and S. Ramakrishna, "Characterization of neural stem cells on electrospun poly(L-lactic acid) nanofibrous scaffold," *Journal of Biomaterials Science, Polymer Edition*, vol. 15, no. 12, pp. 1483–1497, 2004, ISSN: 0920-5063. DOI: 10.1163/1568562042459733. (visited on 03/28/2020).

[35] B. Carlberg, M. Z. Axell, U. Nannmark, J. Liu, and H. G. Kuhn, "Electrospun polyurethane scaffolds for proliferation and neuronal differentiation of human embryonic stem cells," *Biomedical Materials*, vol. 4, no. 4, p. 045 004, 2009, ISSN: 1748-605X. DOI: 10.1088/1748-6041/4/4/045004.

[36] N. Abbasi, S. Soudi, N. Hayati-Roodbari, M. Dodel, and M. Soleimani, "The Effects of Plasma Treated Electrospun Nanofibrous Poly (e-caprolactone) Scaffolds with Different Orientations on Mouse Embryonic Stem Cell Proliferation," *Cell Journal (Yakhteh)*, vol. 16, no. 3, pp. 245–254, 2014, ISSN: 2228-5806.

[37] J. Wei, J. Han, Y. Zhao, *et al.*, "The importance of three-dimensional scaffold structure on stemness maintenance of mouse embryonic stem cells," *Biomaterials*, vol. 35, no. 27, pp. 7724–7733, 2014, ISSN: 0142-9612. DOI: 10.1016/j.biomaterials.2014.05.060.

[38] G. T. Christopherson, H. Song, and H.-Q. Mao, "The influence of fiber diameter of electrospun substrates on neural stem cell differentiation and proliferation," *Biomaterials*, vol. 30, no. 4, pp. 556–564, 2009, ISSN: 0142-9612. DOI: 10.1016/j.biomaterials.2008.10.004.

[39] L. Pieuchot, J. Marteau, A. Guignandon, *et al.*, "Curvotaxis directs cell migration through cell-scale curvature landscapes," *Nature Communications*, vol. 9, no. 1, p. 3995, 2018, ISSN: 2041-1723. DOI: 10.1038/s41467-018-06494-6.

[40] M. Werner, S. B. G. Blanquer, S. P. Haimi, *et al.*, "Surface Curvature Differentially Regulates Stem Cell Migration and Differentiation via Altered Attachment Morphology and Nuclear Deformation," *Advanced Science*, vol. 4, no. 2, 2016, ISSN: 2198-3844. DOI: 10.1002/advs.201600347.

[41] C. M. Hwang, Y. Park, J. Y. Park, *et al.*, "Controlled cellular orientation on PLGA microfibers with defined diameters," *Biomedical Microdevices*, vol. 11, no. 4, pp. 739–746, 2009, ISSN: 1572-8781. DOI: 10.1007/s10544-009-9287-7.

[42] D. Baptista, L. Teixeira, C. van Blitterswijk, S. Giselbrecht, and R. Truckenmüller, "Overlooked? Underestimated? Effects of Substrate Curvature on Cell Behavior," *Trends in Biotechnology*, vol. 37, no. 8, pp. 838–854, 2019, ISSN: 0167-7799. DOI: 10.1016/j.tibtech.2019.01.006.

[43] L. E. Sperling, K. P. Reis, L. G. Pozzobon, C. S. Girardi, and P. Pranke, "Influence of random and oriented electrospun fibrous poly(lactic-co-glycolic acid) scaffolds on neural differentiation of mouse embryonic stem cells," *Journal of Biomedical Materials Research Part A*, vol. 105, no. 5, pp. 1333–1345, 2017, ISSN: 1552-4965. DOI: 10.1002/jbm.a.36012.

[44] A. Bozza, E. E. Coates, T. Incitti, *et al.*, "Neural differentiation of pluripotent cells in 3D alginate-based cultures," *Biomaterials*, vol. 35, no. 16, pp. 4636–4645, 2014, ISSN: 0142-9612. DOI: 10.1016/j.biomaterials.2014.02.039.

[45] P. Soman, B. T. D. Tobe, J. W. Lee, *et al.*, "Three-dimensional scaffolding to investigate neuronal derivatives of human embryonic stem cells," *Biomedical microdevices*, vol. 14, no. 5, pp. 829–838, 2012, ISSN: 1387-2176. DOI: 10.1007/s10544-012-9662-7.

[46] X. Tu, L. Wang, J. Wei, *et al.*, "3D printed PEGDA microstructures for gelatin scaffold integration and neuron differentiation," *Microelectronic Engineering*, Micro and Nano Technologies for Biology and Life Sciences, vol. 158, pp. 30–34, 2016, ISSN: 0167-9317. DOI: 10.1016/j.mee.2016.03.007.

[47] LeeSe-Jun, NowickiMargaret, HarrisBrent, and Z. Grace, "Fabrication of a Highly Aligned Neural Scaffold via a Table Top Stereolithography 3D Printing and Electrospinning," *Tissue Engineering Part A*, 2017. DOI: 10.1089/ten.tea.2016.0353.

[48] K. S. Worthington, L. A. Wiley, E. E. Kaalberg, *et al.*, "Two-photon polymerization for production of human iPSC-derived retinal cell grafts," *Acta Biomaterialia*, vol. 55, pp. 385–395, 2017, ISSN: 1742-7061. DOI: 10.1016/j.actbio.2017.03.039.

[49] *3D printing goes micro*, Library Catalog: physicsworld.com Section: Optics and photonics, 2017. [Online]. Available: https://physicsworld.com/a/3d-printing-goes-micro/ (visited on 04/21/2020).

[50] D. Ricci, M. M. Nava, T. Zandrini, G. Cerullo, M. T. Raimondi, and R. Osellame, "Scaling-Up Techniques for the Nanofabrication of Cell Culture Substrates via Two-Photon Polymerization for Industrial-Scale Expansion of Stem Cells," *Materials*, vol. 10, no. 1, p. 66, 2017. DOI: 10.3390/ma10010066.

[51] M. T. Raimondi, S. M. Eaton, M. Laganà, *et al.*, "Three-dimensional structural niches engineered via two-photon laser polymerization promote stem cell homing," *Acta Biomaterialia*, vol. 9, no. 1, pp. 4579–4584, 2013, ISSN: 1742-7061. DOI: 10.1016/j.actbio.2012.08.022.

[52] G. Della Giustina, A. Gandin, L. Brigo, *et al.*, "Polysaccharide hydrogels for multiscale 3D printing of pullulan scaffolds," *Materials & Design*, vol. 165, p. 107 566, 2019, ISSN: 0264-1275. DOI: 10.1016/j.matdes.2018.107566.

[53] S. Turunen, T. Joki, M. L. Hiltunen, T. O. Ihalainen, S. Narkilahti, and M. Kellomäki, "Direct Laser Writing of Tubular Microtowers for 3D Culture of Human Pluripotent Stem Cell-Derived Neuronal Cells," *ACS Applied Materials & Interfaces*, vol. 9, no. 31, pp. 25 717–25 730, 2017, ISSN: 1944-8244. DOI: 10.1021/acsami.7b05536.

[54] A. Accardo, M.-C. Blatché, R. Courson, I. Loubinoux, C. Vieu, and L. Malaquin, "Two-photon lithography and microscopy of 3D hydrogel scaffolds for neuronal cell growth," *Biomedical Physics & Engineering Express*, vol. 4, no. 2, p. 027 009, 2018, ISSN: 2057-1976. DOI: 10.1088/2057-1976/aaab93.

[55] V. Melissinaki, A. A. Gill, I. Ortega, *et al.*, "Direct laser writing of 3D scaffolds for neural tissue engineering applications," *Biofabrication*, vol. 3, no. 4, p. 045 005, 2011, ISSN: 1758-5090. DOI: 10.1088/1758-5082/3/4/045005.

[56] A. Accardo, M.-C. Blatché, R. Courson, *et al.*, "Multiphoton Direct Laser Writing and 3D Imaging of Polymeric Freestanding Architectures for Cell Colonization," *Small*, vol. 13, no. 27, p. 1 700 621, 2017, ISSN: 1613-6829. DOI: 10.1002/smll.201700621.

[57] A.-I. Bunea, N. del Castillo Iniesta, A. Droumpali, A. E. Wetzel, E. Engay, and R. Taboryski, "Micro 3d printing by two-photon polymerization: Configurations and parameters for the nanoscribe system," *Micro*, vol. 1, no. 2, pp. 164–180, 2021, ISSN: 2673-8023. DOI: 10.3390/micro1020013.

[58] *Processing Guidelines - OrmoPrime08*, Micro resist technology GmbH, 2012. [Online]. Available: https://wiki.nanotech.ucsb.edu/w/images/f/f3/OrmoPrime-NIL-Adhesion-RevA.pdf (visited on 05/03/2020).

[59] A. Trautmann, M. Rüth, H.-D. Lemke, T. Walther, and R. Hellmann, "Two-photon polymerization based large scaffolds for adhesion and proliferation studies of human primary fibroblasts," *Optics & Laser Technology*, vol. 106, pp. 474–480, 2018, ISSN: 0030-3992. DOI: 10.1016/j.optlastec.2018.05.008.

[60] A. Pillarisetti, H. Ladjal, A. Ferreira, C. Keefer, and J. P. Desai, "Mechanical characterization of mouse embryonic stem cells," *2009 Annual International Conference of the IEEE Engineering in Medicine and Biology Society*, vol. 2009, pp. 1176–1179, 2009, ISSN: 1557-170X. DOI: 10.1109/IEMBS.2009.5333954.

[61] N. Gaspard, T. Bouschet, A. Herpoel, G. Naeije, J. van den Ameele, and P. Vanderhaeghen, "Generation of cortical neurons from mouse embryonic stem cells," *Nature Protocols*, vol. 4, no. 10, pp. 1454–1463, 2009, ISSN: 1750-2799. DOI: 10.1038/nprot.2009.157.

[62] E. V. Gazina, E. Morrisroe, G. D. C. Mendis, *et al.*, "Method of derivation and differentiation of mouse embryonic stem cells generating synchronous neuronal networks," *Journal of Neuroscience Methods*, vol. 293, pp. 53–58, 2018, ISSN: 0165-0270. DOI: 10.1016/j.jneumeth.2017.08.018.

[63] B. N. L. Costa, "Fabrication and mechanical characterization of polymer/hydrogel 3d scaffolds for cell culture," Unpublished report., 2020.

[64] I. H. Jaafar, C. E. LeBlon, M.-T. Wei, D. Ou-Yang, J. P. Coulter, and S. S. Jedlicka, "Improving fluorescence imaging of biological cells on biomedical polymers," *Acta Biomaterialia*, vol. 7, no. 4, pp. 1588–1598, 2011, ISSN: 1742-7061. DOI: 10.1016/j.actbio.2010.12.007.

[65] L. Qi, E. K. Knapton, X. Zhang, T. Zhang, C. Gu, and Y. Zhao, "Pre-culture sudan black b treatment suppresses autofluorescence signals emitted from polymer tissue scaffolds," *Scientific Reports*, vol. 7, 2017, ISSN: 2045-2322. DOI: 10.1038/s41598-017-08723-2.

[66] J. T. Y. Lee and K. L. Chow, "SEM sample preparation for cells on 3d scaffolds by freeze-drying and HMDS," *Scanning*, vol. 34, no. 1, pp. 12–25, 2012, ISSN: 1932-8745. DOI: 10.1002/sca.20271.

[67] S. Nikara, E. Ahmadi, and A. A. Nia, "Effects of different preparation techniques on the microstructural features of biological materials for scanning electron microscopy," *Journal of Agriculture and Food Research*, vol. 2, p. 100 036, 2020, ISSN: 2666-1543. DOI: 10.1016/j.jafr.2020.100036.

[68] A. Katsen-Globa, N. Puetz, M. M. Gepp, J. C. Neubauer, and H. Zimmermann, "Study of SEM preparation artefacts with correlative microscopy: Cell shrinkage of adherent cells by HMDS-drying," *Scanning*, vol. 38, no. 6, pp. 625–633, 2016, ISSN: 1932-8745. DOI: https://doi.org/10.1002/sca.21310.

[69] N. H. Hazrin-Chong and M. Manefield, "An alternative SEM drying method using hexamethyldisilazane (HMDS) for microbial cell attachment studies on sub-bituminous coal," *Journal of Microbiological Methods*, vol. 90, no. 2, pp. 96–99, 2012, ISSN: 0167-7012. DOI: 10.1016/j.mimet.2012.04.014.

[70] K. H. Song, S. J. Park, D. S. Kim, and J. Doh, "Sinusoidal wavy surfaces for curvature-guided migration of T lymphocytes," *Biomaterials*, vol. 51, pp. 151–160, 2015, ISSN: 0142-9612. DOI: 10.1016/j.biomaterials.2015.01.071.

[71] X. Zhou, J. Shi, J. Hu, and Y. Chen, "Cells cultured on microgrooves with or without surface coating: Correlation between cell alignment, spreading and local membrane deformation," *Materials Science and Engineering: C*, vol. 33, no. 2, pp. 855–863, 2013, ISSN: 0928-4931. DOI: 10.1016/j.msec.2012.11.011.

[72] K. Nagayama and T. Hanzawa, "Cell type-specific orientation and migration responses for a microgrooved surface with shallow grooves," *Bio-Medical Materials and Engineering*, pp. 1–14, 2022, ISSN: 0959-2989. DOI: 10.3233/BME-211356.

[73] D. Zhang, H. Suo, J. Qian, J. Yin, J. Fu, and Y. Huang, "Physical understanding of axonal growth patterns on grooved substrates: Groove ridge crossing versus longitudinal alignment," *Bio-Design and Manufacturing*, vol. 3, no. 4, pp. 348–360, 2020, ISSN: 2522-8552. DOI: 10.1007/s42242-020-00089-1.

[74] S. Rello-Varona, J. Stockert, V. Moreno, *et al.*, "Morphological criteria to distinguish cell death induced by apoptotic and necrotic treatments," *Apoptosis : an international journal on programmed cell death*, vol. 10, pp. 201–8, 2005. DOI: 10.1007/s10495-005-6075-6.

[75] P. Acedo, J. Stockert, M. Cañete, and A. Villanueva, "Two combined photosensitizers: A goal for more effective photodynamic therapy of cancer," *Cell death & disease*, vol. 5, e1122, 2014. DOI: 10.1038/cddis.2014.77.

[76] P. Tayalia, C. R. Mendonca, T. Baldacchini, D. J. Mooney, and E. Mazur, "3D Cell-Migration Studies using Two-Photon Engineered Polymer Scaffolds," *Advanced Materials*, vol. 20, no. 23, pp. 4494–4498, 2008, ISSN: 1521-4095. DOI: 10.1002/adma.200801319.

[77] C. H. Li and P. K. S. Tam, "An iterative algorithm for minimum cross entropy thresholding," *Pattern Recognition Letters*, vol. 19, no. 8, pp. 771–776, 1998, ISSN: 0167-8655. DOI: 10.1016/S0167-8655(98)00057-9.

[78] C. A. Glasbey, "An Analysis of Histogram-Based Thresholding Algorithms," *CVGIP: Graphical Models and Image Processing*, vol. 55, no. 6, pp. 532–537, 1993, ISSN: 1049-9652. DOI: 10.1006/cgip.1993.1040.

[79] L.-K. Huang and M.-J. J. Wang, "Image thresholding by minimizing the measures of fuzziness," *Pattern Recognition*, vol. 28, no. 1, pp. 41–51, 1995, ISSN: 0031-3203. DOI: 10.1016/0031-3203(94)E0043-K.

[80] N. Otsu, "A Threshold Selection Method from Gray-Level Histograms," p. 5, 1979.

Appendix A

Design table

Table A.1: Design table scaffolds

Structure	Dimensions (µm)	Top view and trimetric view
Pedestal	Overall size: • Length (L): 140 • Width (W): 140 • Height (H): 50	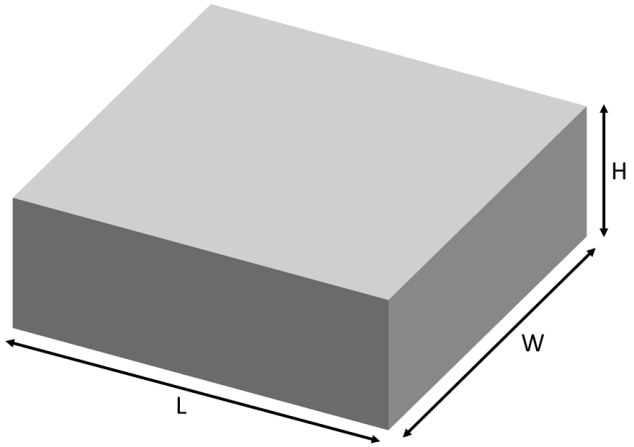
Big square (BS) scaffold	Feature sizes: • Beam diameter (D_b): 2 • Gap length (l): 30 • Gap width (w): 30 • Gap height (h): 30 • Initial gap height (h_i): 31 Overall size: • Length (L): 98 • Width (W): 98 • Height (H): 97	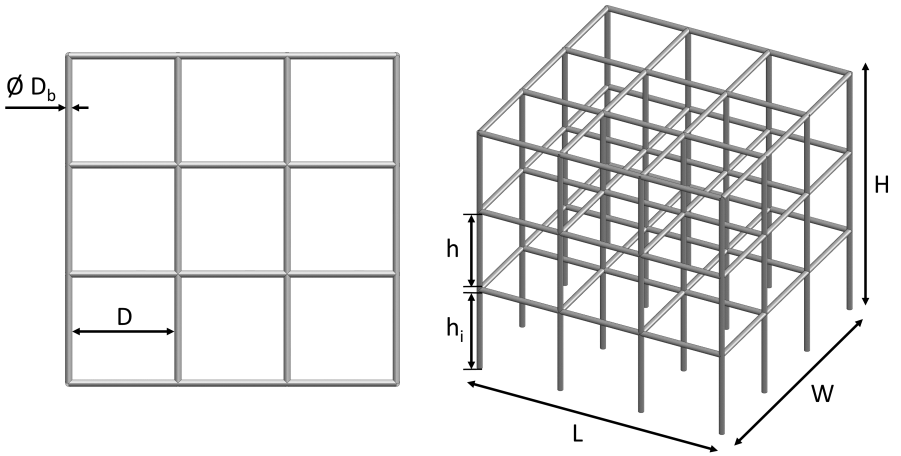

Small square (SS) scaffold	Feature sizes: • Beam diameter (D_b): 1 • Gap length (l): 15 • Gap width (w): 15 • Gap height (h): 15 Overall size: • Length (L): 65 • Width (W): 65 • Height (H): 65	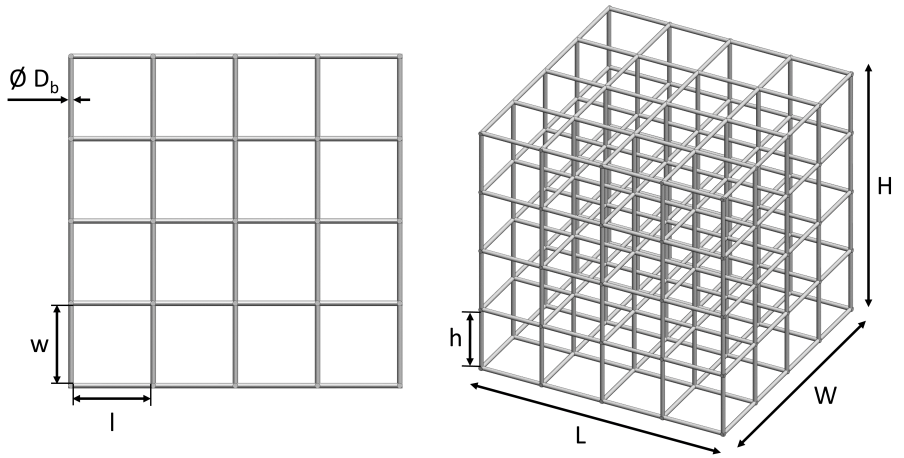
Big small square (SSB) scaffold bd1	Feature sizes: • Beam diameter (D_b): 1 • Gap length (l): 15 • Gap width (w): 15 • Gap height (h): 15 Overall size: • Length (L): 97 • Width (W): 97 • Height (H): 97	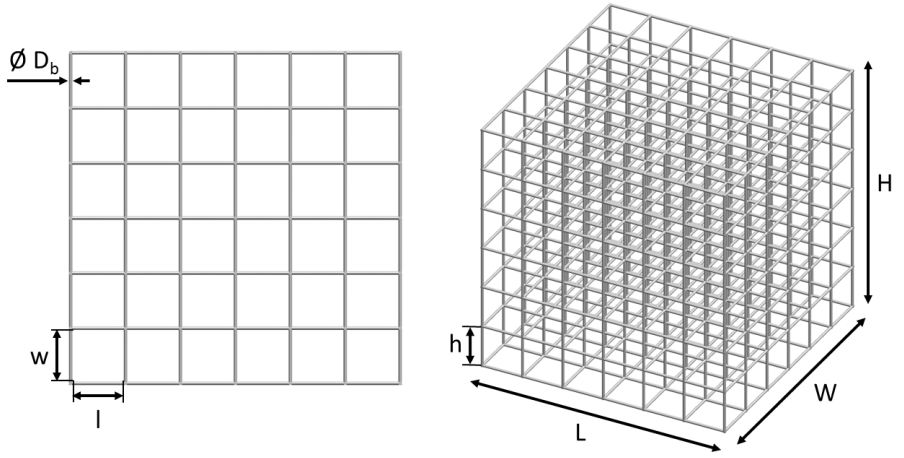

Big circular (BC) scaffold	Feature sizes: • Beam diameter (D_b): 1 • Gap diameter (D): 29 Overall size: • Length (L): 91 • Width (W): 91 • Height (H): 91	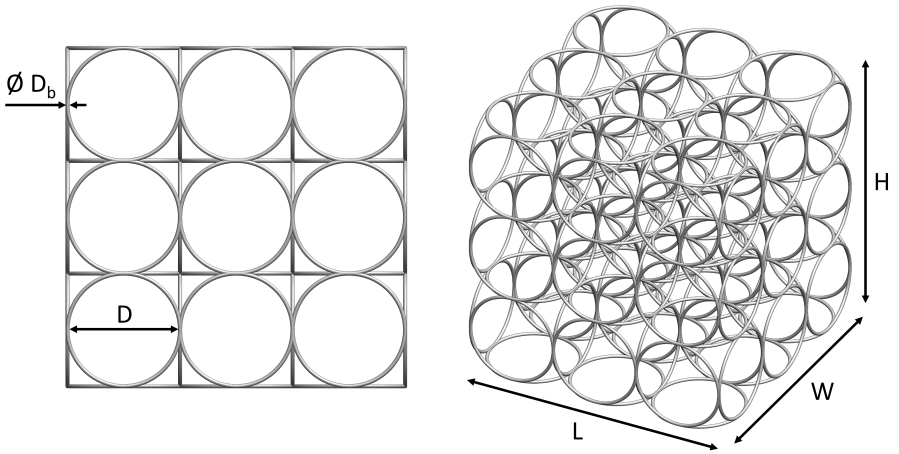
Big circular bd2 (BCF) scaffold	Feature sizes: • Beam diameter (D_b): 2 • Gap diameter (D): 28 Overall size: • Length (L): 92 • Width (W): 92 • Height (H): 92	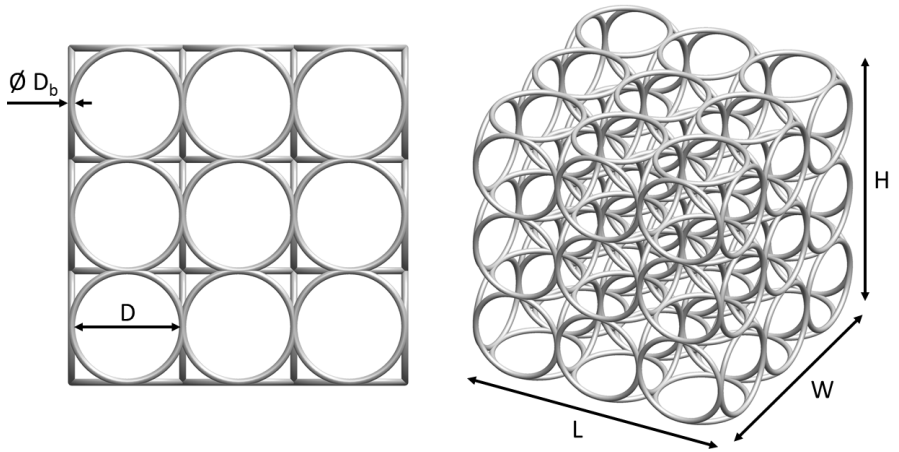

Small circular (SC) scaffold	Feature sizes: • Beam diameter (D_b): 1 • Gap diameter (D): 14 Overall size: • Length (L): 46 • Width (W): 46 • Height (H): 46	
Big small circular (SCB) scaffold	Feature sizes: • Beam diameter (D_b): 1 • Gap diameter (D): 14 Overall size: • Length (L): 91 • Width (W): 91 • Height (H): 91	

Sinusoidal scaffold/Sine wave	Feature sizes: • Period (P): 100 • Amplitude (A): 25 • Base height (h_B): 25 • Height left (h_L): 50 • Height right (h_R): 50 Overall size: • Length (L): 500 • Width (W): 500 • Height (H): 75	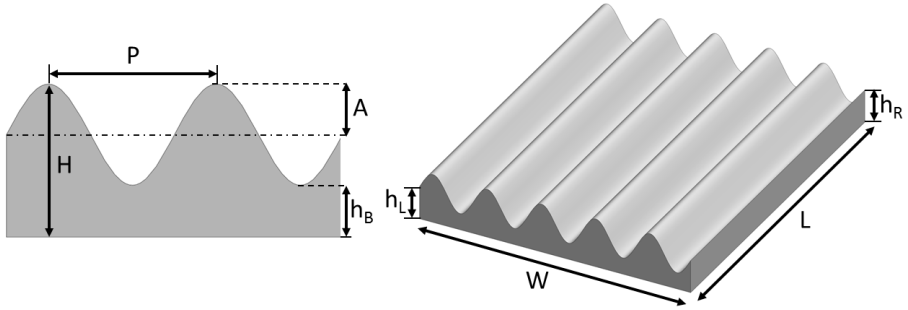
Triangular scaffold/lines	Feature sizes: • Base height (h_B): 50 • Spacing (a): 50 • Triangle height/depth (b): 25 Overall size: • Length (L): 500 • Width (W): 600 • Height (H): 75	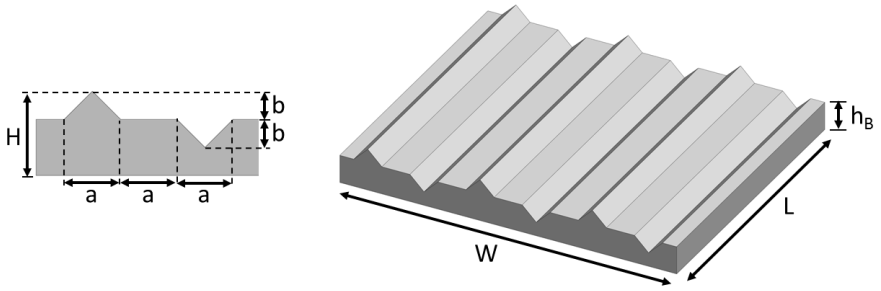

Pyramidal scaffold/pyramids	Feature sizes: • Base height (h_B): 50 • Spacing (a): 50 • Pyramid height/depth (b): 25 Overall size: • Length (L): 400 • Width (W): 400 • Height (H): 75	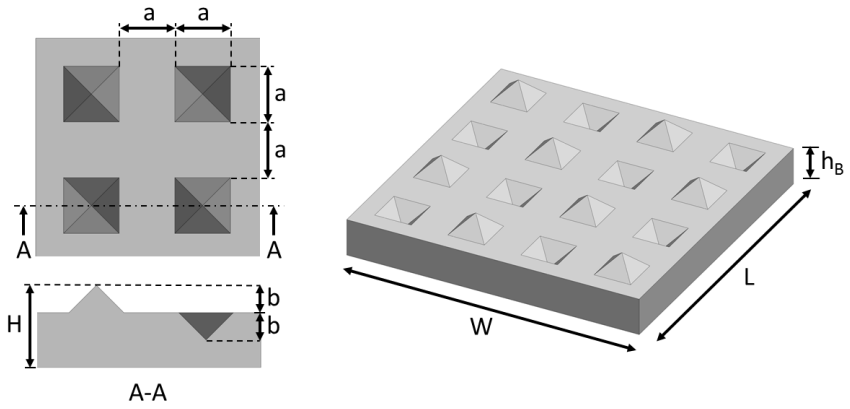
Large pedestal 25 µ	Overall size: • Length (L): 500 • Width (W): 500 • Height (H): 25	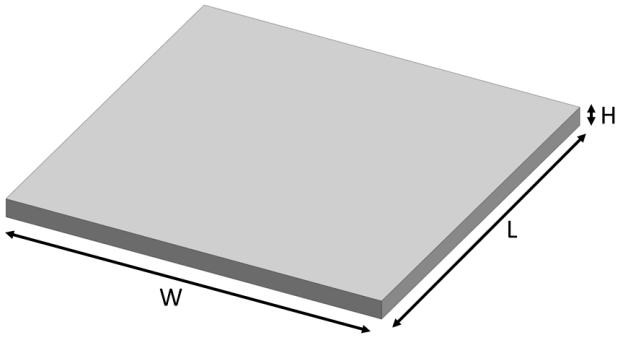

Large pedestal 50 µ	Overall size: • Length (L): 500 • Width (W): 500 • Height (H): 50	
Rectangular lines	Overall size: • Length (L): 500 • Width (W): 500 • Height (H): 50	

Cylindrical lines	Overall size: • Length (L): 500 • Width (W): 600 • Height (H): 50	
Spherical hills and valleys	Overall size: • Length (L): 500 • Width (W): 500 • Height (H): 50	

Appendix B

Print settings table

Table B.1: Printing parameters per scaffold. These settings apply for DiLL mode printing of IP-Dip with the 63x objective on the Nanoscribe.

Structure	**Slicing distance (µm)**	**Hatching distance (µm)**	**Scan speed (mm/s)**	**Laser power (%)**	**Interface position**	**Galvo acceleration (V/ms^2)**	**Printing time (hr:min:sec)**
Pedestal	0.4	0.3	60	90	0.5	1	11:48
Big square (BS) scaffold	0.3	0.2	10	80	1.0	1	1:38
Small square (SS) scaffold	0.3	0.2	10	80	1.0	1	1:52
Big circular (BC) scaffold	0.3	0.2	10	80	1.0	1	3:56
Big circular bd2 (BCF) scaffold	0.3	0.2	50	100	0.5	10	-
Small circular (SC) scaffold	0.3	0.2	10	80	1.0	1	1:43
Big Small circular (SCB) scaffold	0.3	0.2	10	80	1.0	1	-
Sine wave	0.4	0.3	60	90	0.5	10	1:25:59
Triangular lines	0.4	0.3	60	90	0.5	10	1:26:37
Pyramids	0.4	0.3	60	90	0.5	10	42:31
Rectangular lines	0.4	0.3	60	90	0.5	10	1:05:02
Large pedestal 25mu	0.4	0.3	60	90	0.5	10	00:29:24
Large pedestal 50mu	0.4	0.3	60	90	0.5	10	1:10:25

Appendix C

Extra 3D scaffold designs

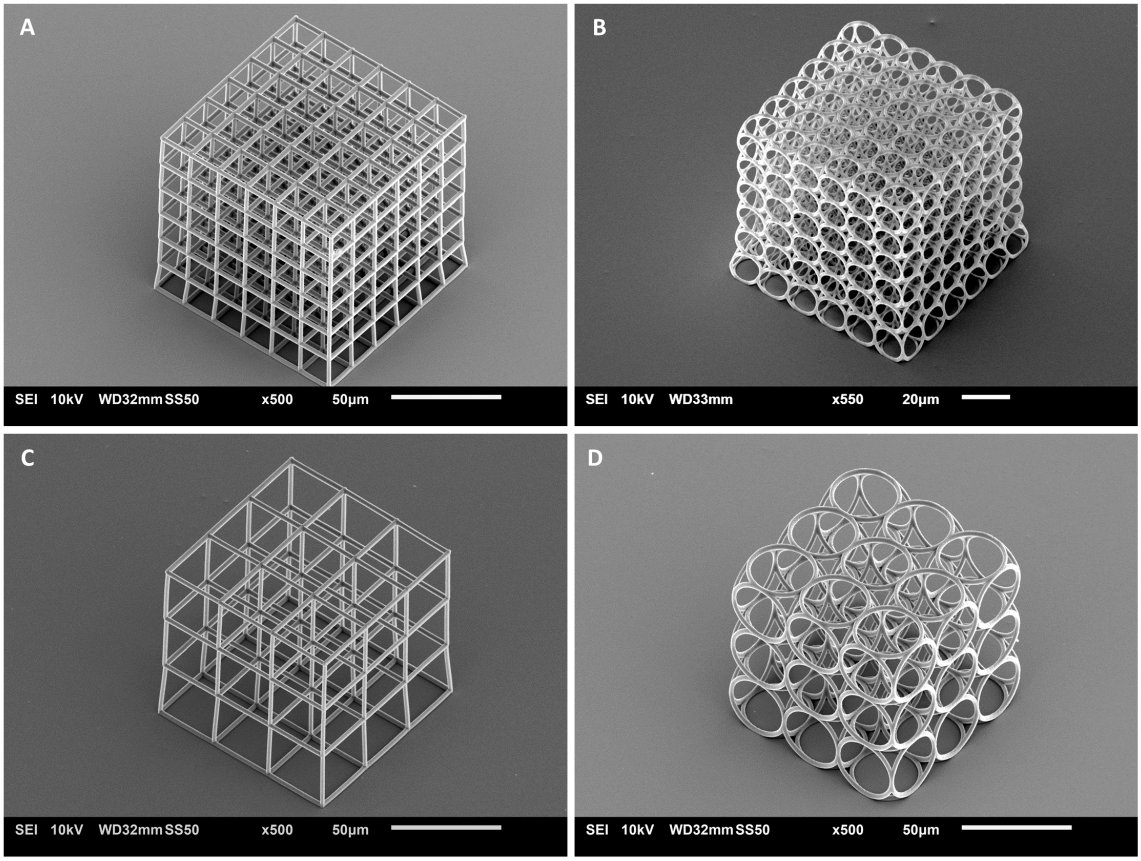

Figure C.1: SEM images of 3D scaffold designs for cell culture.

Appendix D

Comparison threshold algorithms

Since the method for finding the fraction of DAPI or phalloidin in the z-projection of a stack and the volumetric occupancy of the scaffolds is based on a threshold algorithm, different threshold methods were compared in Fiji/ImageJ to determine the effect they have on the results that are obtained.

The experiments that were used for comparison were with HeLa on scaffolds (CF078) and mESC on scaffolds (CF080). Each of the experiments consisted of two samples that had a different seeding density and different method of confocal imaging, namely method A and C.

Threshold influence on fraction of phalloidin in z-projection

The wide range of available threshold algorithms was first reduced by comparing the result of said thresholds on the z-stack of one particular scaffold with the actual z-projection by eye and choosing the most applicable algorithms. From this comparison, it was decided to continue with the following methods: default (the original method of autothresholding in ImageJ), Li [77], Mean [78], Huang [79] and Otsu [80], which were readily available in ImageJ. These methods were then compared with a manually chosen threshold that was set by the user, based on the threshold result compared to the actual colored z-projection. The same threshold was set for each scaffold of the sample.

For each of these methods, the data were analyzed for the fraction of phalloidin in the z-projection and averaged per type of scaffold. In figure D.1 the results are shown for sample 3 of the Hela experiment and sample 5 of the mESC experiment. It is seen that while the methods do not quantitatively agree with each other, they more or less do qualitatively. For the HeLa cells of sample 3, the default, Li and Otsu method give similar results, which are slightly different from the Mean, Huang and manual method which in turn are similar in result. However, all methods agree that the big circular scaffold contains the least amount of phalloidin. For the mESC, the results of all methods are really similar, with the exception of the manual method. However, again, all methods agree on the scaffold with the least amount of phalloidin, the small circular scaffold.

Now we look at the distribution of the average phalloidin fraction per type of scaffold for each of the automatic methods (excluding the manual method) for all four samples of the experiments.

Interestingly, there is a visible difference for the variation in distributions for each microscope configuration (independent of the cell type). The distributions for stacks taken at Delft is much narrower than the distributions for the stacks taken at EMC.

Threshold influence on phalloidin occupancy per slice

In order to figure out the effect of the threshold algorithm on the volumetric occupancy, we look at the area occupied by phalloidin per slice of the stack of a specific scaffold for both samples of the HeLa experiment. Some extra algorithms were added here: Isodata and Moments. Furthermore, a different method is proposed where the lower bound of the threshold is varied linearly with the depth of the stack ("Linear" in figure D.3). The lower threshold value linearly increases with increasing stack number, thus as we get deeper into the scaffold, to account for the decreasing signal intensity.

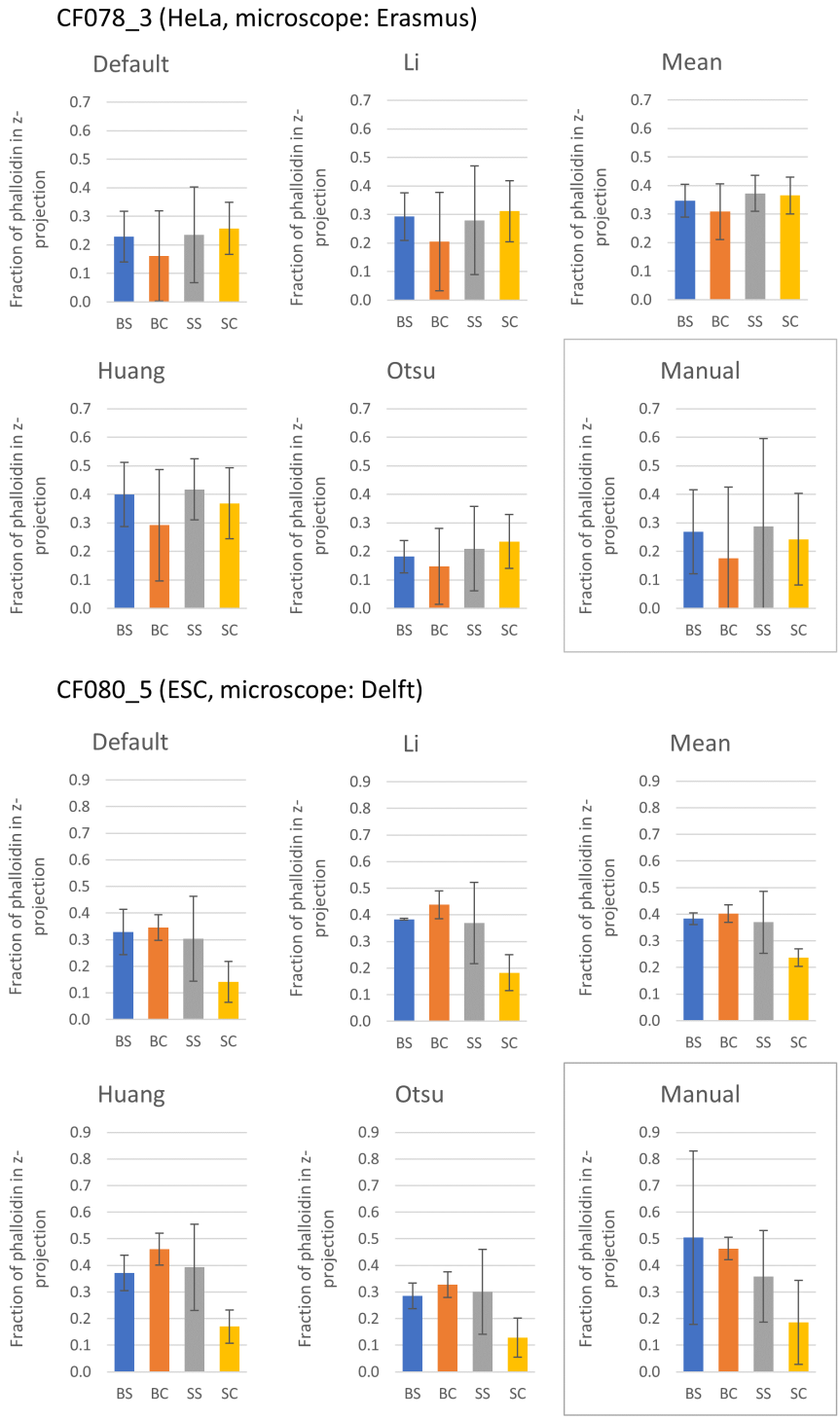

Figure D.1: Influence of threshold algorithm (Fiji/ImageJ) on phalloidin fraction in z-projection of scaffolds with HeLa cells (CF078) and in the z-projection of scaffolds with mESCs (CF080). Substrate 3 of CF078 was imaged with method C, substrate 5 of CF080 with A.

The upper bound is always set to the maximum. The minimum and maximum lower bound are manually inserted. The same bounds are then used for each scaffold of the sample but they are

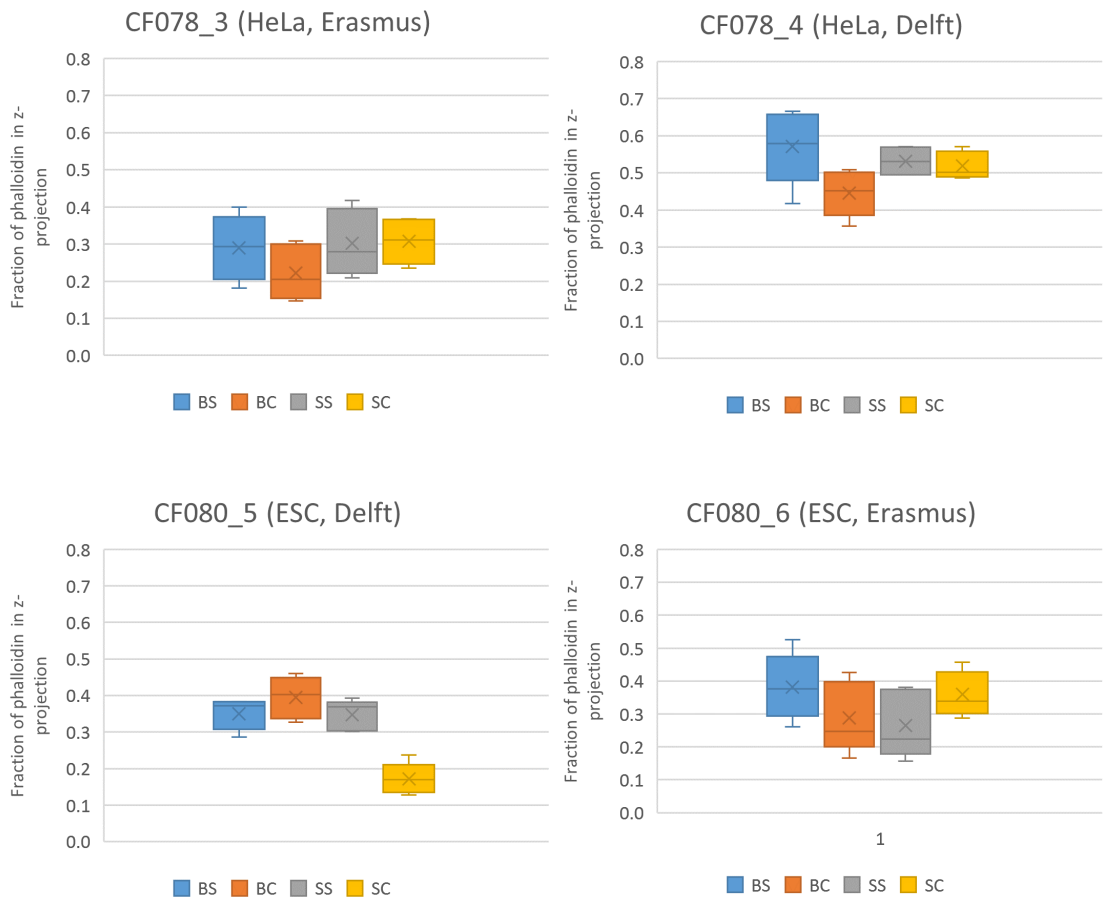

Figure D.2: Distribution of fraction of phalloidin in z-projection per scaffold type for Hela and mESC experiment, calculated by five different threshold algorithms in ImageJ: default, Li, Mean, Huang and Otsu.

adjusted for each sample. In figure D.3 one can see the results for scaffold 6 of substrate 4 and scaffold 6 of substrate 3 of experiment CF078.

We notice that the graphs for substrate 4 start at almost the same point, but vary wildly in shape after that, whereas for substrate 6, the opposite seems to be the case. The zig-zag behaviour that is mostly seen in the graphs of substrate 3 can be accounted for by the discrete essence of pixel intensity and intensity thresholds. It is more prevalent in this stack, because it consists of more slices.

Based on a comparison with the graphs and the actual slices judged by the eye of the user, it seems that the linear varying threshold gives the most accurate representation of the amount of phalloidin per slice. For the analysis of the volumetric occupancy of all scaffolds, it was decided to continue with this method.

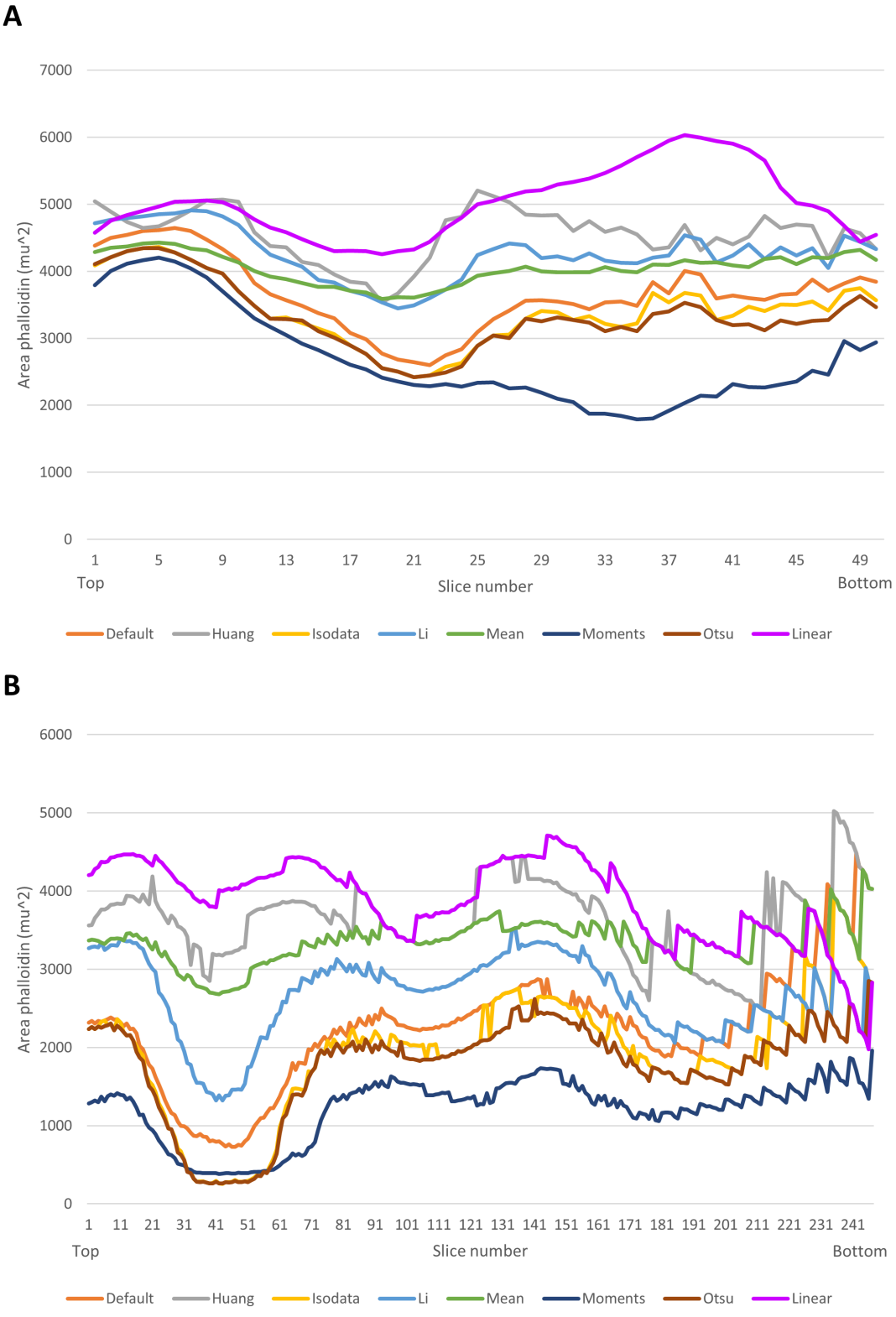

Figure D.3: Threshold influence on phalloidin area per slice of scaffold stack for both seeding densities of HeLa in big square scaffold. Compared methods: Default, Huang, Isodata, Li, Mean, Moments, Otsu and a linear varying threshold ("Linear"). A) Seeding density of 120,000 cells/cm^2, stack imaged with Leica SP5 Intravital. B) Seeding density of 160,000 cells/cm^2, stack imaged with Nikon Eclipse Ti.

Appendix E

Dose tests

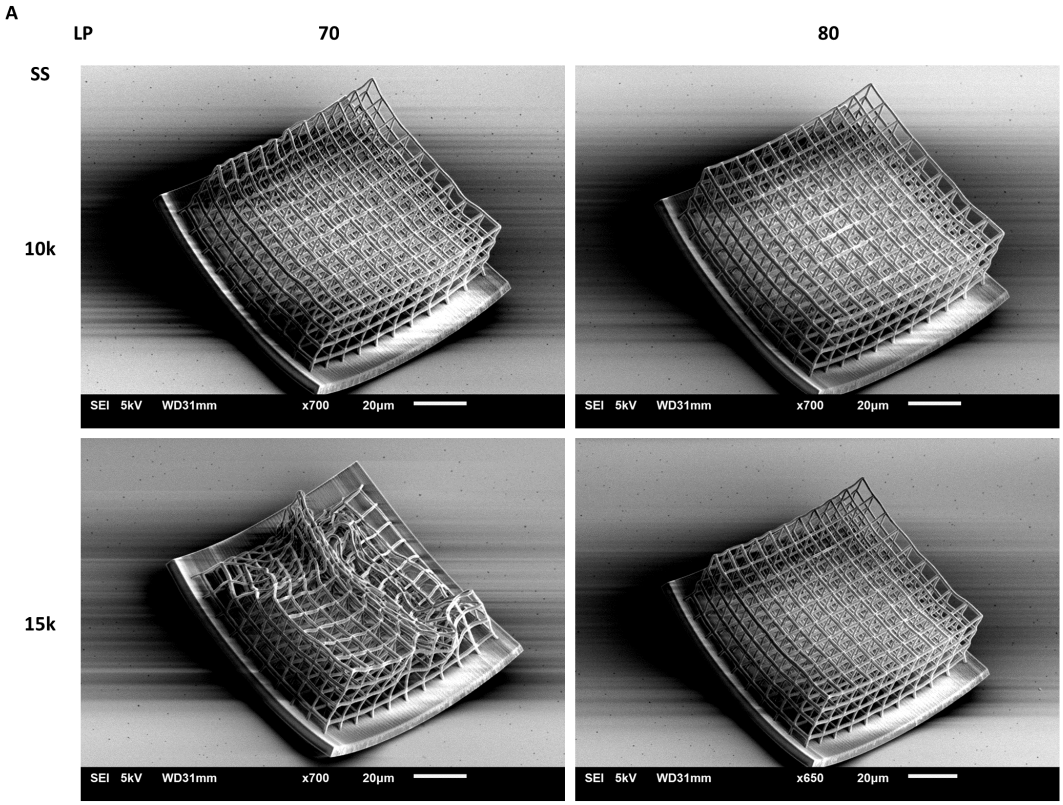

Figure E.1: Dose test of IP-Dip microcage (gap diameter 1 µm and beam diameter 1 µm) on base pedestal, printed with Nanoscribe in DiLL configuration with 63x objective. Slicing distance: 0.4 µm, hatching distance: 0.4 µm. Scan speed (SS) 10k and 15k µm/s and laser power (LP) 70 and 80%. Structure was printed on a substrate that was plasma cleaned with O_2 for 5 minutes before applying the resist.

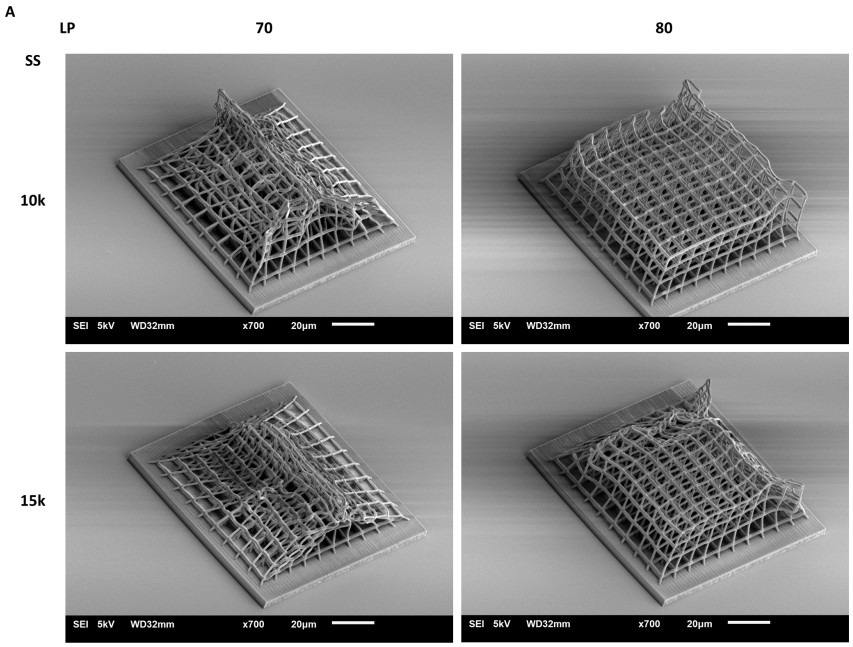

Figure E.2: Dose test of IP-Dip microcage (gap diameter 1 µm and beam diameter 1 µm) on base pedestal, printed with Nanoscribe in DiLL configuration with 63x objective. Slicing distance: 0.4 µm, hatching distance: 0.4 µm. Scan speed (SS) 10k and 15k µm/s and laser power (LP) 70 and 80%. Structure was printed on a substrate that was spincoated with Ormoprime before applying the resist.

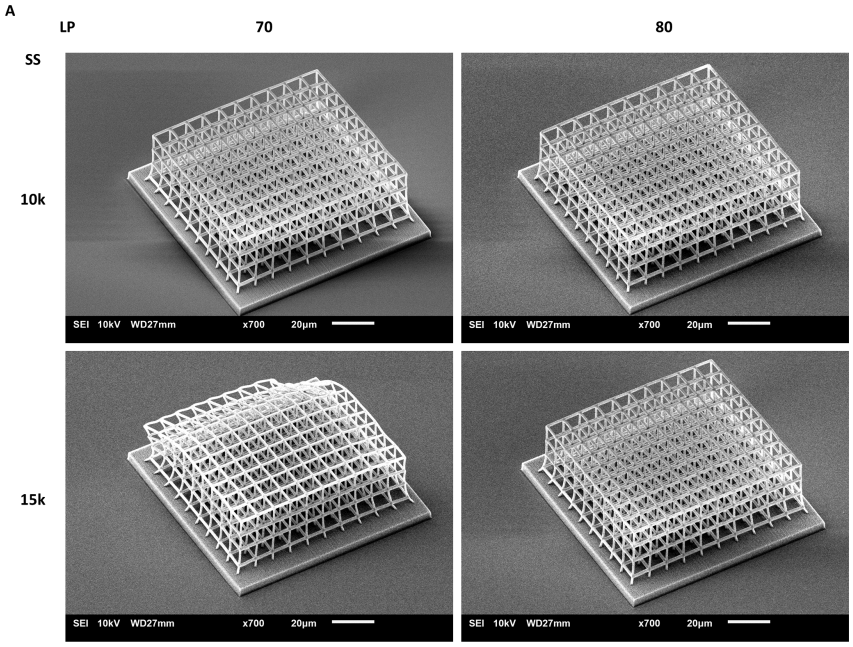

Figure E.3: Dose test of IP-Dip microcage (gap diameter 1 µm and beam diameter 1 µm) on base pedestal, printed with Nanoscribe in DiLL configuration with 63x objective. Slicing distance: 0.3 µm, hatching distance: 0.3 µm. Scan speed (SS) 10k and 15k µm/s and laser power (LP) 70 and 80%. Structure was printed on a substrate that was spincoated with Ormoprime before applying the resist.

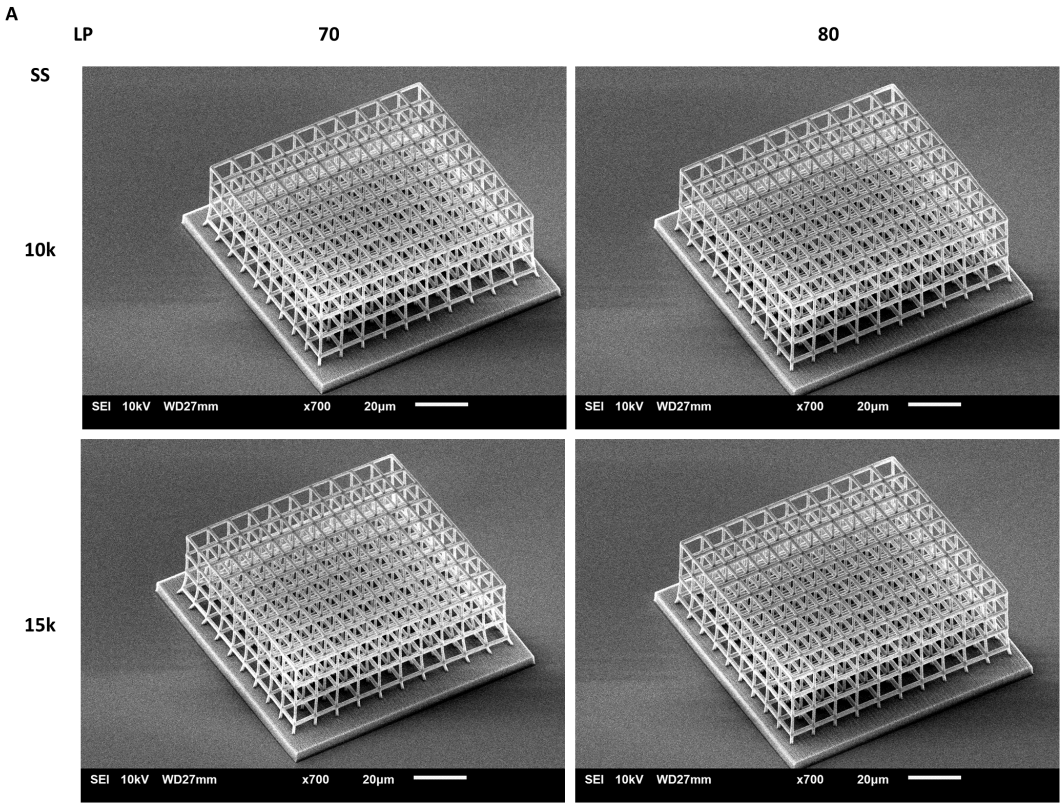

Figure E.4: Dose test of IP-Dip microcage (gap diameter 1 µm and beam diameter 1 µm) on base pedestal, printed with Nanoscribe in DiLL configuration with 63x objective. Slicing distance: 0.3 µm, hatching distance: 0.2 µm. Scan speed (SS) 10k and 15k µm/s and laser power (LP) 70 and 80%. Structure was printed on a substrate that was spincoated with Ormoprime before applying the resist.

Appendix F

Mean intensity comparison confocal imaging configurations

F.1 MP versus confocal in oil immersion configuration

What is interesting is that the multiphoton mean intensity is very low in the top part of the scaffold whereas this is not the case for the regular confocal (both stacks imaged in oil immersion configuration). The result for the multiphoton laser is counter intuitive as we expect most light to reach the top part of the scaffold and as we go deeper and more light diffracts this intensity goes down. It could be that parts of the structure got bleached while choosing the settings.

From the graph we scan also see the high resolution for oil imaging as the peaks are narrow and we can distinguish all four circle layers (or plateaus) that the circular scaffold has. Moreover the valleys are approximately on the same level of intensity, indicating the absence of signal interference from other layers. The overall mean intensity of the peaks does decline as we go deeper into the scaffold, as is to be expected but the signal is still high enough for a nice reconstruction.

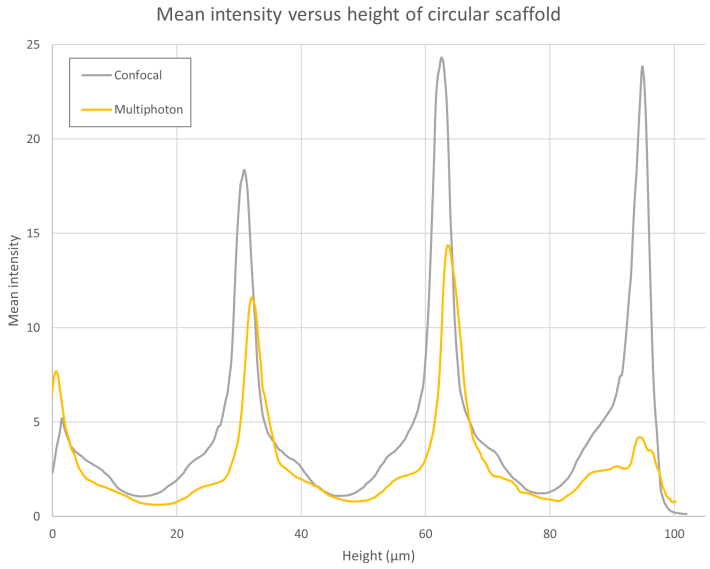

Figure F.1: Mean intensity of green channel per slice of circular scaffold (beam diameter 2 µm, pore diameter 30 µm) for oil immersion confocal imaging versus oil immersion multiphoton imaging with Leica SP 5 Intravital. 40x Oil objective (NA 1.25)

F.2 Confocal in vectashield immersion configuration

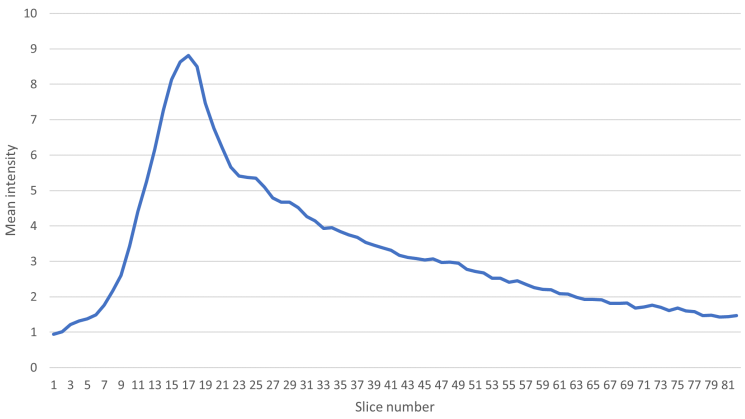

Figure F.2: Mean intensity of green channel per slice of small square scaffold (beam diameter 1 µm, pore diameter 15 µm) for Vectashield immersion confocal imaging with Leica SP 5 Intravital. 40x Oil objective (NA 1.25)

F.3 Confocal with press-to-seal versus plastic sheet in water dipping configuration

The peaks are more clearly distinguishable for the scaffolds imaged with the sheet configuration and if we look at scaffolds that contain almost no cells, we see the same as for the oil immersion, that the dips are more or less on the same mean intensity level. When a seal is used, the dips are declining more rapidly in intensity with increasing depth. For scaffolds with more cells, this effect is also present for the scaffolds imaged with a sheet.

F.4 Confocal imaging with Vectashield and seal per scaffold type

The obtainable image quality also depends on the scaffold type. For scaffolds with large pore sizes it is almost always possible to distinguish the peaks whereas for the smaller pore size of 15 µm, this is not the case even though these scaffolds are less high. There also seems to be a slight difference between squares and circular scaffolds, square scaffolds resulting in a slightly better image quality deeper in the scaffold. Both these phenomena are likely a result of the material density inside the scaffold, with more material leading to more diffraction and shadowing and thus a loss or "smudging" of signal. Thus the bigger scaffolds are more suitable for 3D analysis.

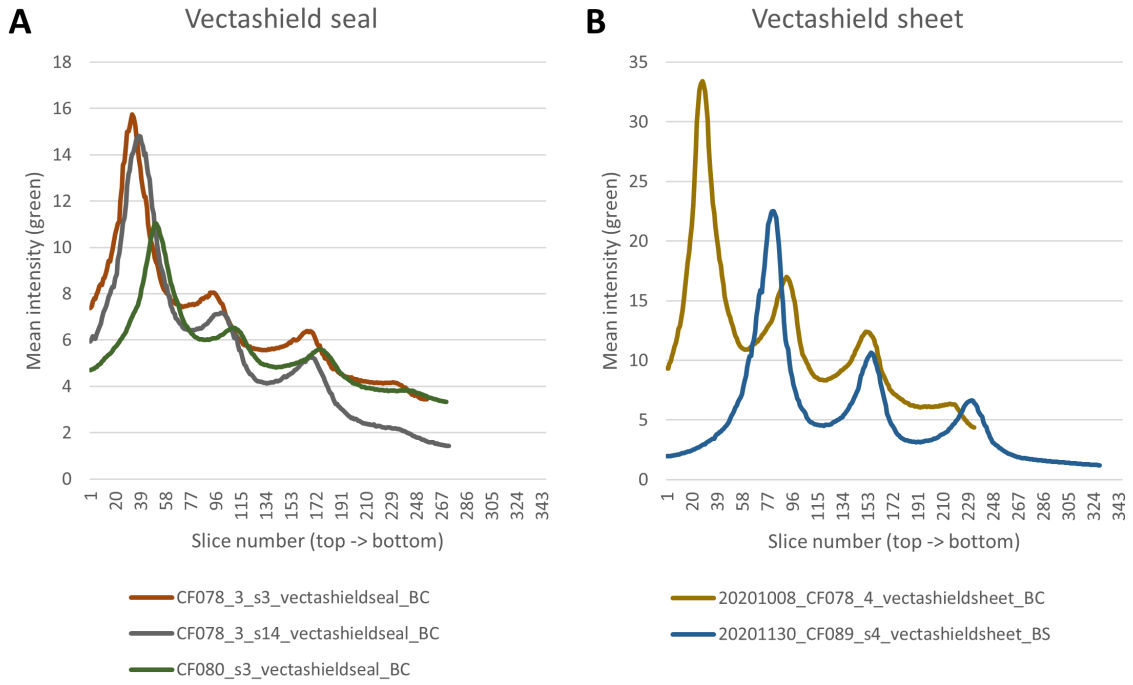

Figure F.3: Comparison of mean intensity of green channel per slice per imaging configuration: Vectashield with a seal versus Vectashield with a sheet. Imaged with Leica SP 5 Intravital. 20x WD objective (NA 1.0)

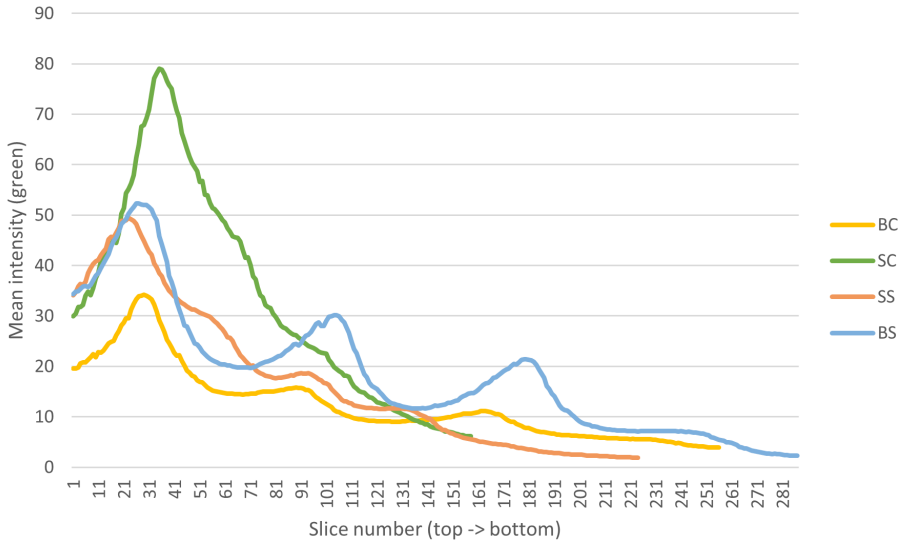

Figure F.4: Mean intensity of green channel per slice per scaffold type: BS, BC, SS and SC imaging configuration with Vectashield and a Press-to-seal. Imaged with Leica SP 5 Intravital. 20x WD objective (NA 1.0). Sample $CF078_3$.

Appendix G

Correlation SEM distortion top versus side of scaffolds

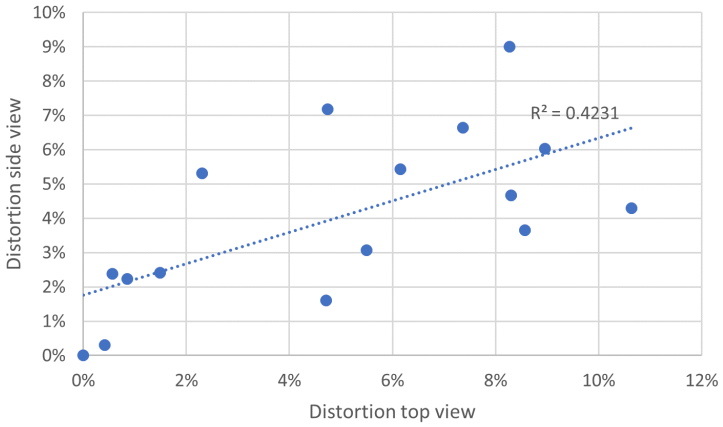

Figure G.1: Correlation between scaffold (BS, BC, SS and SC) deformation in top and side view SEM images after HeLa cell culture of 2 days (seeding density 200,000 cells/mL) and SEM sample preparation via different protocols.

Appendix H

SEM dehydration experiment density

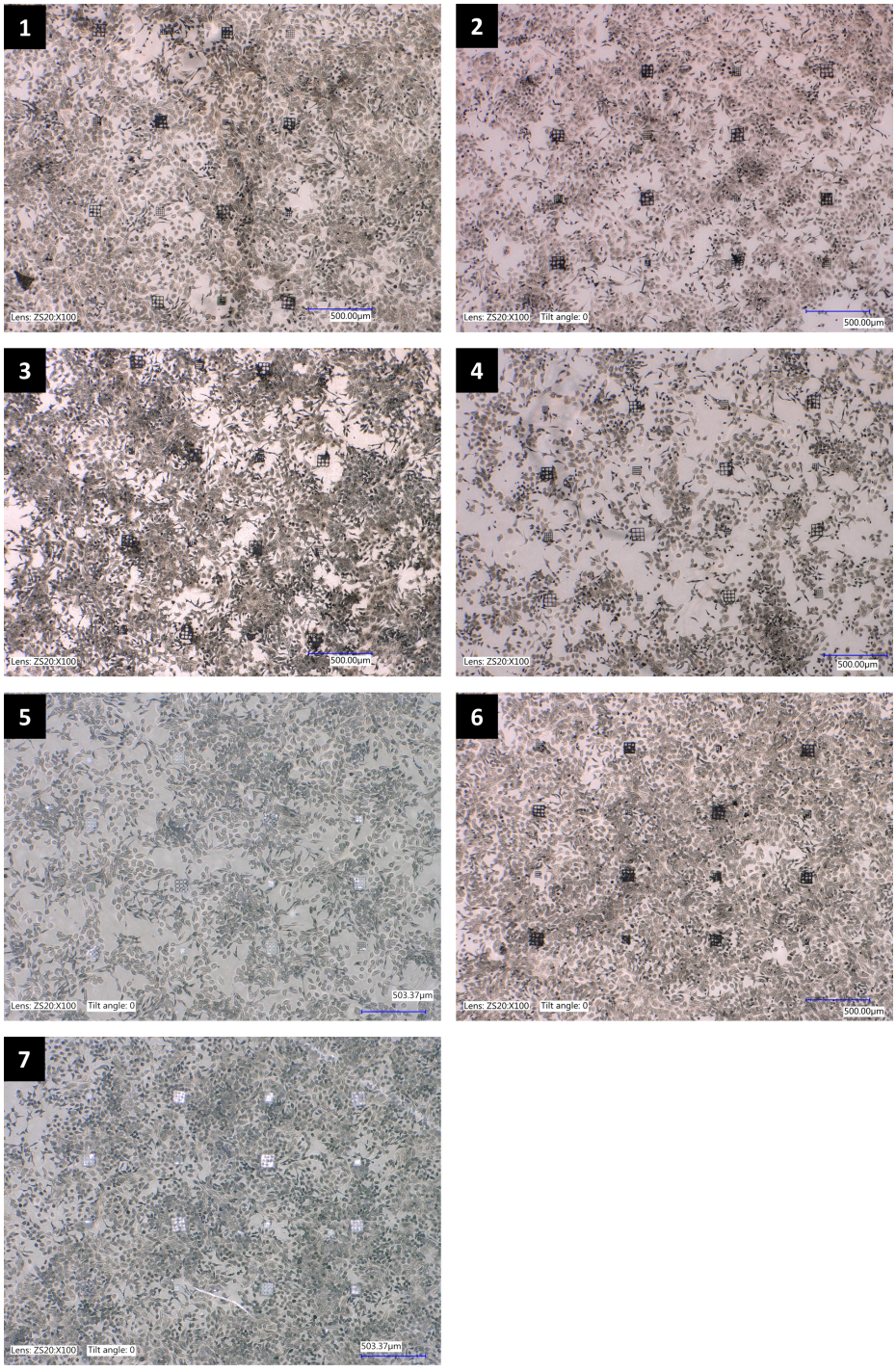

Figure H.1: Overview of scaffolds and cells on substrates seeded with 200,000 cells/mL after a 2-day culture. The samples were prepared for SEM imaging by fixation and dehydration according to protocol 1-7. Images taken with Keyence.

Appendix I

HEK-293T experiments

Sterilization Different sterilization methods were tried on the samples before seeding HEK293-T cells. In some cases the seal or IP-Dip structures were omitted for comparison. The methods tried were:

A Seal is pressed onto the substrate with IP-Dip pedestals and UV sterilized for 1 hour.

B Seal is pressed onto the substrate with IP-Dip pedestals and UV sterilized for 1 hour. A 0.1% gelatin coating is then applied for 1 hour.

C Substrate with pedestals and seal (adhesive side upwards) were UV sterilized separately for 1 hour, after which the seal was placed onto the substrate.

D Substrate with pedestals is placed in 70% ethanol for 45 minutes, substrate and seal are then UV sterilized separately for 1 hour, after which the seal is placed onto the substrate.

E Substrate with pedestals is UV sterilized for 1 hour and then placed in a 6cm dish with 5 mL of cell medium.

F The seal is autoclaved for 15 minutes at 121°C and a substrate with pedestals is UV sterilized for 1 hour, after which the seal is placed onto the substrate.

G The seal is autoclaved for 15 minutes at 121°C and then soaked in 70% ethanol for 5 minutes. Ethanol is removed and the seal is washed 4x with PBS for 3 minutes. A substrate with pedestals is sterilized in 70% ethanol for 30 minutes and then UV sterilized for 1 hour. The seal is then placed onto the substrate.

H Same procedure as G but with a bare substrate (no pedestals).

I Bare substrate is sterilized in 70% ethanol for 30 minutes and then UV sterilized for 1 hour. Substrate is placed in a 6cm dish.

J As a control, the same cell source is seeded on a 10cm dish.

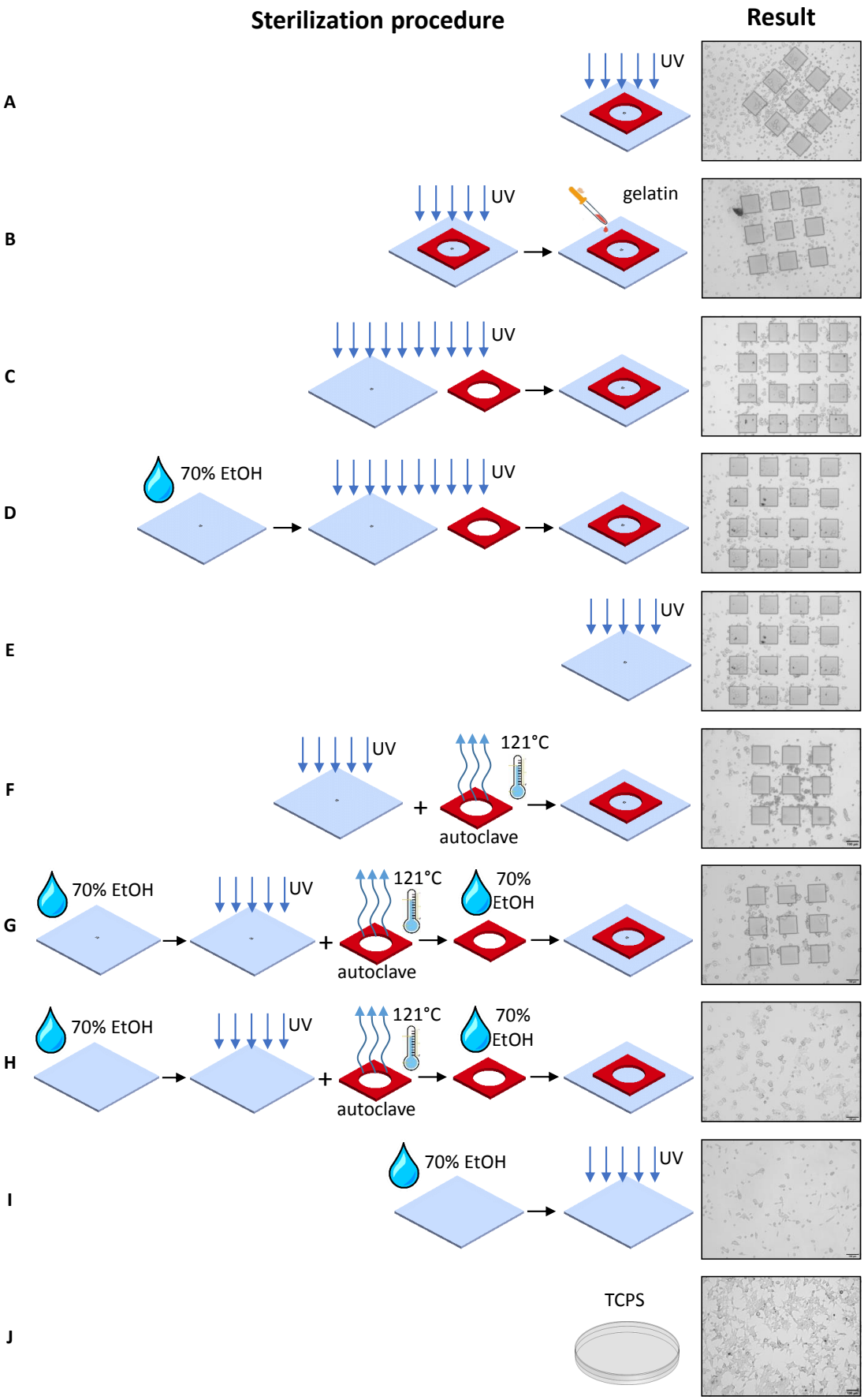

Figure I.1: HEK293-T cell culture after 6 hours (figure A and B) or 48 hours (figure C-J) on fused silica substrates sterilized by applying different protocols (figures A-I) versus a control grown in a petridish (figure J). Samples A-G contain an array of two photon polymerized IP-Dip pedestals, whereas sample H and I are empty. In cases A-D and F-H a silicone isolator was used to contain the cell medium, whereas substrates E and I were placed in a 6 cm petridish. Some healthy cells were observed outside of the pedestals in sample F, but most cells showed a rounded, unhealthy morphology which was also observed in the rest of the samples, except for the control. Contamination was observed in.... , in the other samples there was no (clear) source of contamination.

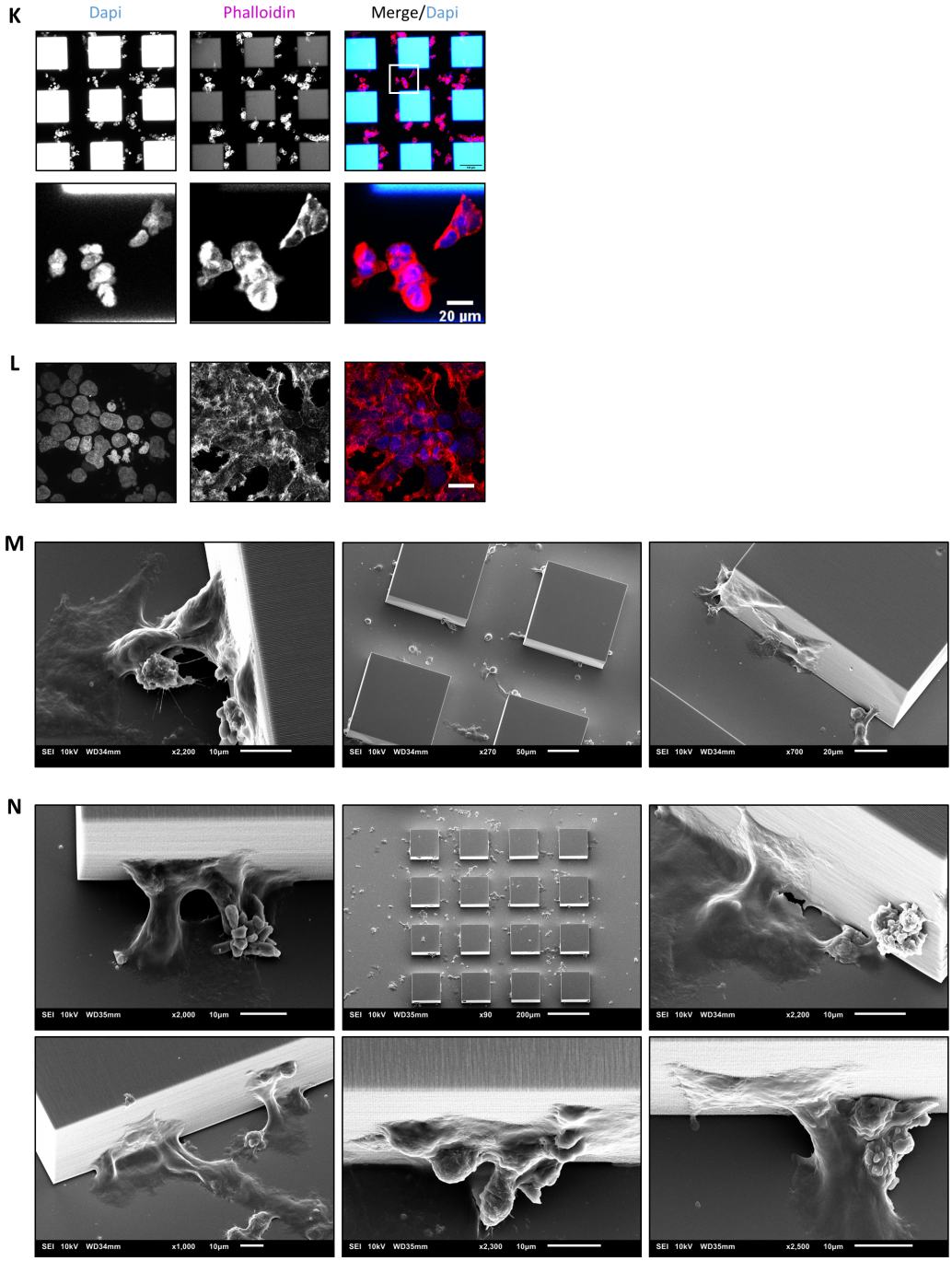

Figure I.2: Figure 4.1 continued. K) Confocal image of HEK293-T cell culture on fused silica substrate with pedestals after 48 hours, stained with phalloidin and Dapi. Sterilization performed according to procedure F. L) Healthy HEK293-T cell culture grown in TCPS (procedure M) for comparison. The cells in figure K show a much rounder morphology. Scalebar represents 20 µm. M) SEM images of HEK293-T cell culture grown on pedestals sterilized according to procedure C. N) SEM images of HEK293-T cell culture grown on pedestals sterilized according to procedure D.

Appendix J

Effect of seeding location on cell distribution within press-to-seal

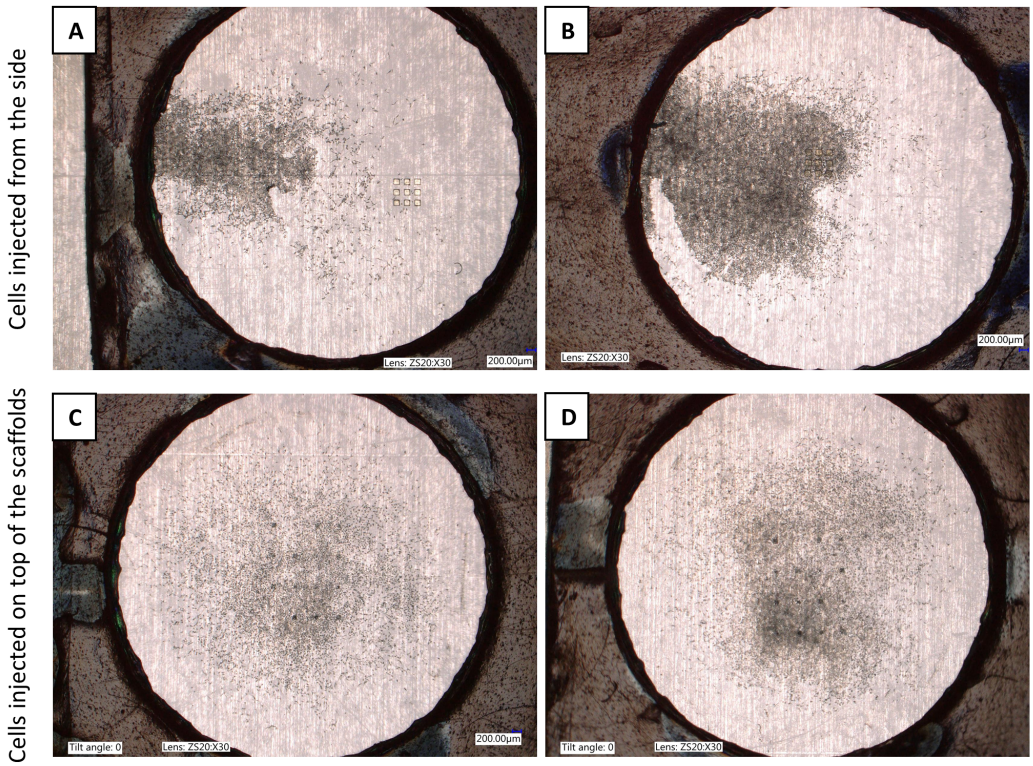

Figure J.1: Effect of seeding location on cell distribution of HeLa cells within a Press-to-Seal after two days of culture. A-B) Cells injected from the side of the well. Sample contained 2P-printed pedestals and were seeded with A) 80,000 cells/cm^2 and B) 160,000 cells/cm^2 C-D) Cells injected on top of scaffolds in the centre. Sample contained 2P-printed scaffolds and were seeded with C) 120,000 cells/cm^2 and D) 160,000 cells/cm^2. Optical images taken with Keyence.

Appendix K

Simulation of projected major axis angle distribution in nuclei on sinusoidal scaffold

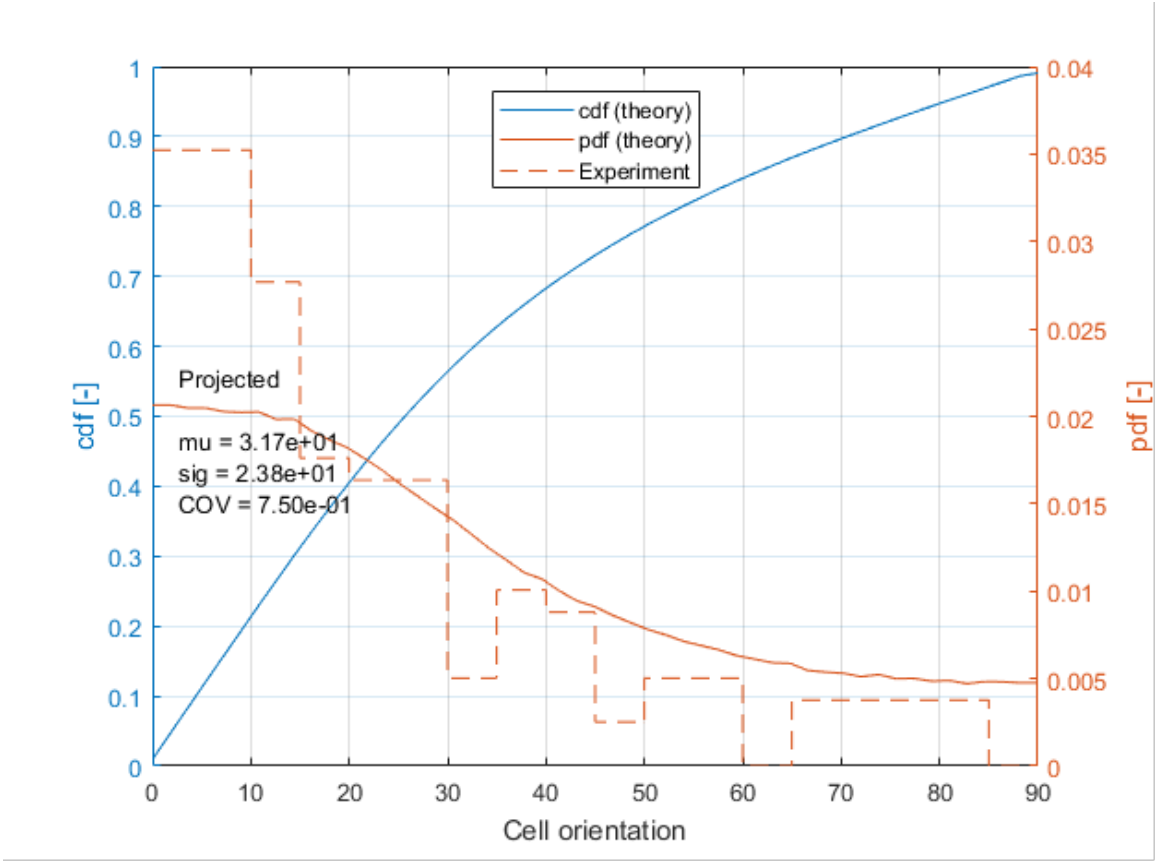

Figure K.1: Monte Carlo simulation of experiment with HeLa cells on a sinusoidal structure with wavelength 100 µm and an amplitude of 25 µm to investigate nuclei alignment with the sinusoidal waves. A random distribution of nuclei is assumed on the structure with random alignment, after which the observed angle with the major axis in the 2D projection are calculated. The theoretical (simulated) results are plotted as a cumulative (cdf) and probability density function (pdf). The experimental values are plotted as a dashed line (probability density function).

Appendix L

Distribution phalloidin within 3D scaffolds

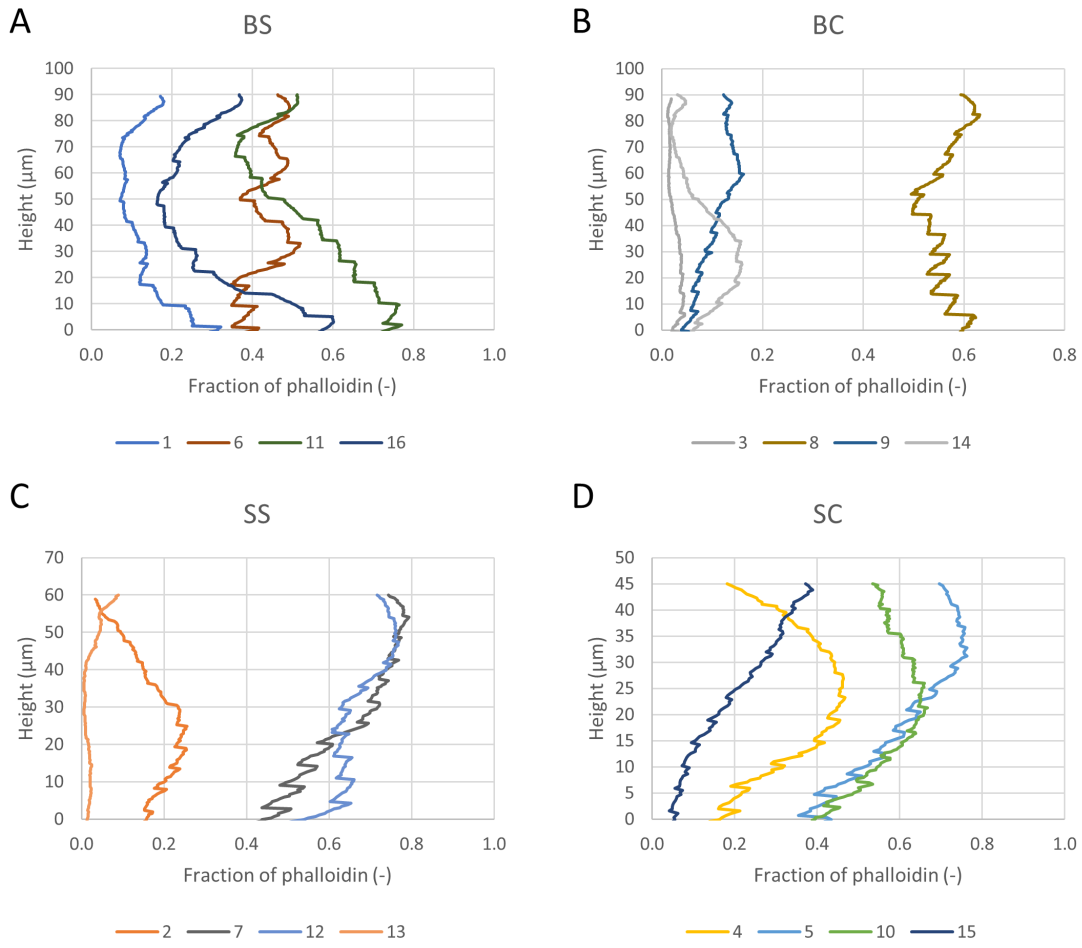

Figure L.1: Volumetric occupancy of phalloidin in scaffolds of substrates seeded with respectively 120,000 versus 160,000 HeLa cells/cm^2. A-D) Distribution of phalloidin within the scaffolds for substrate seeded with 120,000 cells/cm^2 for each scaffold type: BS, BC, SS and SC. Different colors/numbers represent the different scaffolds, of each type we analysed 4 scaffolds.

Appendix M

Volumetric vs z-projection occupancy

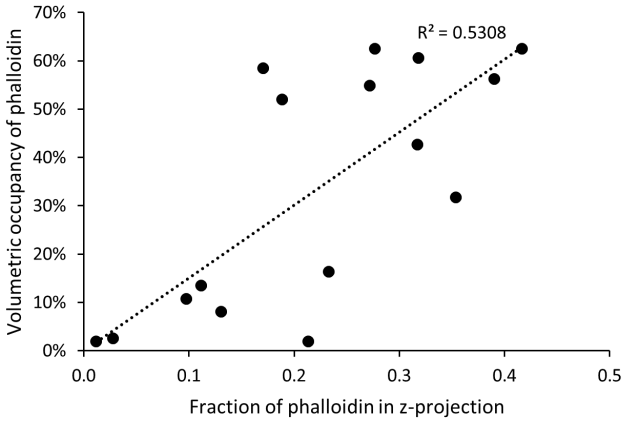

Figure M.1: Phalloidin volumetric occupancy of scaffolds versus phalloidin fraction in maximum z-projection of scaffolds on substrate seeded with 120,000 cells/cm^2, including a linear trendline. N=16 (consisting of 4 scaffolds of 4 types).